

Institut de Physique de l'Université de Neuchâtel (Suisse)



- Advanced LPCVD ZnO - Challenges in Application for Thin Film Solar Cells and Modules

THÈSE

présentée à la Faculté des Sciences
de l'Université de Neuchâtel

pour l'obtention du grade de docteur ès sciences

PAR

Daniel Messerschmidt

Soutenue le 23 juillet 2014

En présence du directeur de thèse:
Prof . Philipp Aebi

Et des rapporteurs:
Prof. Christophe Ballif
Prof. Thomas Südmeyer
Prof. Edda Rädlein
Dr. Jens Eberhardt

Neuchâtel 2014

IMPRIMATUR POUR THESE DE DOCTORAT

**La Faculté des sciences de l'Université de Neuchâtel
autorise l'impression de la présente thèse soutenue par**

Monsieur Daniel MESSERSCHMIDT

Titre:

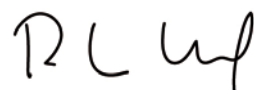
**Advanced LPCVD ZnO – Challenges in Application for Thin
Film Solar Cells and Modules**

sur le rapport des membres du jury composé comme suit :

- Prof. Philipp Aebi, Université de Fribourg, directeur de thèse
- Prof. Thomas Südmeyer, Université de Neuchâtel
- Prof. Christophe Ballif, EPF Lausanne
- Prof. Edda Rädlein, Technische Universität Ilmenau, D
- Dr. Jens Eberhardt, Bosch Solar Energy AG, D

Neuchâtel, le 12 août 2014

Le Doyen, Prof. P. Kropf



Abstract

Ethanol is used as a precursor during the growth of zinc oxide (ZnO) by low-pressure chemical vapor deposition (LPCVD). By adding ethanol, the surface of the deposited ZnO layer is flattened and its roughness is decreased about sevenfold. The layers become increasingly stressed and their resistivity grows significantly. The present work proposes an explanation for the observed behavior based on the catalytic decomposition of ethanol at the ZnO surface and on the growth of selected crystal planes. By using ethanol for the last 10% of the total ZnO layer growth only, sheet resistance is maintained and roughness is slightly decreased. The results indicate that such LPCVD ZnO bilayers could be a promising method to modify the ZnO surface morphology before cell deposition, thus providing an alternative to argon plasma treatment, which is typically reported to improve solar cell parameters such as open-circuit voltage and fill factor.

The introduction of an advanced LPCVD boron-doped ZnO (ZnO:B) into the production line at Bosch Solar Thin Film in Erfurt, Germany, is presented. Here the ZnO:B is deposited with a LPCVD production tool on $1.1 \times 1.3 m^2$ glass substrates. Early results on a laboratory scale of this advanced transparent conductive oxide (ATCO) type were published by Ding et al. [1,2]. For an ATCO, they combined a highly doped ZnO:B seed layer with a low-doped ZnO:B bulk layer. Compared to a standard ZnO:B (Std-TCO), which is homogeneously doped across the total layer thickness, the ATCO possesses enhanced optical and electrical properties. Comparing the ATCO with the Std-TCO, equal in layer thickness (1800 nm) and sheet resistance (16 to 17 Ω), the ATCO possesses slightly better transmittance. Furthermore, the ATCO showed 37% haze, which is 3 to 5% absolute more haze compared to the Std-TCO. After ATCO optimization, a complete micromorph solar module was fabricated, incorporating this new advanced LPCVD ZnO:B layer as the front electrode. An initial module power of 153.7 Wp was achieved. Here the unit Wp indicates that the module was tested under standardized test conditions. The power output was determined at 25°C with a light illumination power of 1000 W/m^2 . The light spectrum was adjusted to be equivalent to an terrestrial solar spectrum with an air mass 1.5 characteristic.

For the first time the present work introduces a novel degradation effect of the ZnO, which is observed for ZnO layers deposited on commercially available soda-lime glass. When an electric field is applied, the potential induced anodic degradation causes a

massive sheet resistance increase of the ZnO. The present work shows that the increase in resistance strongly affects the power output of small non-encapsulated and large encapsulated micromorph thin-film photovoltaic modules, in which ZnO was used as the front electrode. The present work proposes that the evolution of gaseous oxygen at the anode (ZnO) may be responsible for the increased resistance of the ZnO. A model that describes this observation is presented and solutions to suppress the effect are proposed. The optical properties of non-degraded and anodically degraded ZnO:B are presented. The optical model used to simulate the infrared reflectance in the wavelength range between 1.2 and 25 μm is based on the Maxwell-Garnett effective-medium theory. The model is sensitive to the conditions at the grain boundaries of the investigated polycrystalline ZnO:B films. The yielded results confirm the presence of defect-rich grain boundaries, especially after degradation. Furthermore, indications of a degraded ZnO layer next to the ZnO:B/glass interface with a different refractive index are found. Furthermore, based on Raman investigations, evidence for the creation of oxygen vacancies, which correlate with a shift of the optical absorption edge of the ZnO:B, is presented. Investigations with scanning and transmission electron microscopy show microvoids at the grain boundaries after anodic degradation. This indicates that the grain/grain interfaces are the principle location of defects after degradation.

Contents

Contents	i
List of Figures	iii
List of Tables	vii
1 Introduction	1
1.1 Contribution to the Field of Research	3
2 Principles of Thin-Film Silicon PV	5
2.1 Zinc Oxide - Deposition and Material Properties	5
2.1.1 Deposition of Zinc Oxide by LPCVD	6
2.1.2 Structural Properties	11
2.1.3 Electrical Properties	12
2.1.4 Optical Properties	14
2.1.5 Dielectric Function of Polycrystalline LPCVD ZnO:B	16
2.2 Silicon Thin Films - Deposition and Material Properties	18
2.2.1 Deposition of Silicon Thin Films by Plasma-Enhanced Chemical Vapor Deposition	18
2.2.2 Amorphous Silicon	20
2.2.3 Microcrystalline Silicon	21
2.3 Micromorph Solar Cells and Modules	22
2.3.1 Concept of a micromorph solar cell	23
2.3.2 Working principles of a solar cell and characteristic I(V) parameters	24
2.3.3 Module Fabrication	28
3 Techniques of Characterization	31
3.1 Optical Characterization	31
3.1.1 Ultraviolet-Visible Spectroscopy	31
3.1.2 Fourier Transform Infrared Spectroscopy	32
3.1.3 Raman Spectroscopy	34
3.2 Electrical Characterization	34
3.2.1 Four-Point Probe Resistance Measurement	34
3.2.2 Hall Effect Measurement	34
3.3 Structural Characterization	36
3.3.1 Atomic Force Microscopy	36
3.3.2 X-Ray Diffraction Analysis (XRD)	37
3.3.3 Secondary Ion Mass Spectroscopy (SIMS)	37

3.4	Characterization of Solar Cells and Modules	38
3.4.1	Current-Voltage Characterization of Solar Cells and Modules	38
3.4.2	External Quantum Efficiency (EQE)	39
4	Ethanol-enriched LPCVD ZnO bilayers: Properties and Growth – A Potential Electrode for Thin Film Solar Cells	41
4.1	Background	41
4.2	Experimental	43
4.3	Results	43
4.3.1	ZnO single layers deposited using a mixture of ethanol, water and DEZ	43
4.3.2	Ethanol-enriched bilayers	51
4.4	Conclusion	54
5	Integration of Advanced-TCO into the Production Line at Bosch	57
5.1	Experimental	58
5.2	Results	59
5.2.1	Variation of process temperature	60
5.2.2	Variation of water-diethylzinc ratio	62
5.2.3	Variation of process pressure	63
5.2.4	Variation of seed layers deposition time / thickness	64
5.2.5	Variation of bulk layer doping	65
5.2.6	Comparison of ATCO vs. Std-TCO	67
5.2.7	Result on module power using ATCO	69
5.3	Conclusion	70
6	Anodic degradation of ZnO:B on soda-lime glass	71
6.1	Background	71
6.2	Experimental	73
6.3	Anodic degradation of a large size module in the climate chamber . . .	75
6.4	Anodic degradation of a unencapsulated mini module on the hot plate .	77
6.5	Degradation of samples with ZnO:B on glass only	79
6.5.1	Electrical changes of glass/ZnO:B samples	79
6.5.2	Optical changes of glass/ZnO:B samples	81
6.6	The glass substrate as a source of oxygen during degradation treatment	92
6.7	Model of anodic degradation of ZnO:B at the glass/ZnO:B interface . .	93
6.8	Improvements	97
6.9	Conclusion	100
7	Summary	103
	References	105
	A IR spectral reflectivity response of low-iron soda-lime glass	ix
	Publications	xiii
	Acknowledgment	xv
	Curriculum Vitae	xvii

List of Figures

1.1	Net price reduction of solar modules based on micromorph technology.	2
2.1	Demonstration of high reactivity between DEZ and water at atmospheric pressure.	7
2.2	Small LPCVD system.	8
2.3	Large size LPCVD TCO1200 deposition system.	10
2.4	Crystallographic structure of ZnO.	11
2.5	SEM images of a standard ZnO layer. Morphology and cross section .	12
2.6	Barrier model of ZnO grain boundaries.	14
2.7	Transmittance and reflectance of LPVCD ZnO deposited on a glass substrate.	15
2.8	PECVD deposition system for Si thin-film fabrication.	19
2.9	Classification of energy states into non-localized and localized band stands in amorphous silicon.	20
2.10	Illustration of the microstructural characteristics of $\mu\text{c-Si:H}$	22
2.11	Comparison of absorption coefficients for amorphous, microcrystalline and crystalline silicon material as a function of photon energy and wavelength.	22
2.12	Layer configuration of a micromorph solar cell.	23
2.13	Sketch of a band diagram of a solar cell with p-i-n structure under short-circuit conditions.	25
2.14	Current-voltage characteristic of a solar cell, showing important electric parameters.	27
2.15	Electric equivalent circuit of a single-junction solar cell.	28
2.16	Illustration of the process to produce a monolithic interconnection of single solar cells on the glass substrate.	29
2.17	Thin-film silicon solar module.	30
3.1	Principle setup of an integrating sphere.	32
3.2	Schematic of Michelson interferometer.	32
3.3	Schematic of collinear probe arrangement for four-point probe measurement.	34
3.4	Schematic of Hall effect.	35
3.5	Schematic of x-ray diffraction geometry (Bragg-Brentano).	37
3.6	Comparison of light spectra of solar simulator and terrestrial solar spectrum AM1.5.	38
4.1	Deposition rate – ethanol enriched LPCVD ZnO	44
4.2	SEM images of surface - ethanol enriched LPCVD ZnO	45
4.3	XRD data - ethanol enriched LPCVD ZnO.	46

4.4	Resistivity of ZnO films versus ethanol flow rate during deposition. . .	47
4.5	IR reflection spectra of ZnO films deposited with and without ethanol.	49
4.6	Optical transmission next to the optical absorption edge of glass samples covered with ZnO, deposited with and without ethanol.	50
4.7	Evolution of haze at 600 nm as a function of ethanol mass flow rate during the deposition of ZnO.	51
4.8	Sketch of layer stack, RMS surface roughness and simplified bilayer equivalent circuit.	52
4.9	Sheet resistance of ethanol-enriched bilayers as a function of cap-layer thickness.	53
4.10	SEM image of an ethanol-enriched bilayer in comparison to a standard ZnO layer.	54
5.1	Schematic of the deposition tool TCO1200.	58
5.2	Distribution of layer properties after the retrofit of TCO1200.	59
5.3	Comparison of ATCO and Std-TCO before optimization.	60
5.4	Variation of process temperature.	61
5.5	Variation of the water/DEZ ratio.	62
5.6	Variation of process pressure.	64
5.7	Variation of seed layer thickness.	65
5.8	Variation in bulk layer doping.	66
5.9	Comparison of ATCO and Std-TCO for the optimized deposition parameters.	68
5.10	Comparison of transmission measured index matched for ATCO and Std-TCO.	69
5.11	Best results achieved on ATCO with non-retrofitted PECVD equipment.	69
6.1	Equipment for biased damp heat experiments in the climate chamber. .	73
6.2	Experimental setup for TCO degradation tests.	74
6.3	Comparison of thin-film silicon solar module performances in the climate chamber, with and without biasing.	76
6.4	Solar Module's fill factor (FF) and series resistance (R_s) as a function of time in the climate chamber.	76
6.5	I(V) characteristics of a small module based on an a-Si:H and μ c-Si:H silicon tandem solar cell structure before and after degradation treatment.	77
6.6	External quantum efficiency of a small module measured at different spots on the active module area before and after degradation treatment.	78
6.7	Evolution of the resistance of the ZnO:B covered glass samples during hot plate treatment.	80
6.8	Scanning electron microscopy (SEM) images of a ZnO:B surface after an anodic degradation treatment.	82
6.9	Transmittance spectra of a 3.2-mm-thick soda-lime glass substrate covered with ZnO:B before and after degradation treatment.	82
6.10	IR reflectance of non-degraded and degraded ZnO:B deposited on glass.	84
6.11	Modeled layer stacks used for simulating the IR reflectance spectra of the non-degraded and degraded sample.	85
6.12	Refractive index (n) and extinction coefficient (k) for non-degraded, degraded ZnO materials.	88

6.13	Transmission electron (TEM) and scanning electron (SEM) microscopy images of a non-degraded and degraded ZnO film deposited on soda-lime glass.	90
6.14	The change between the degraded sample and the non-degraded one in the Raman signal is presented.	91
6.15	SIMS intensity of the ratio $m/e=60$	93
6.16	A SEM cross section illustrates the conditions under the anode (ZnO:B) – The model of the anodic degradation of ZnO on soda-lime glass . . .	95
6.17	Different approaches of LPCVD ZnO:B in order to reduce the sensitivity to the the hot plate and climate chamber treatment.	98
6.18	Optical and electrical properties of different homogeneously doped Std-TCOs, Lasagne-TCO and ATCO.	98
6.19	Comparison of different types of LPCVD ZnO:B treated on the hot plate.	99
6.20	Modules under test in the climate chamber. Different configurations have been studied to stabilize the power loss.	100
A.1	Experimental and simulated IR reflectance data of a 3.2-mm-thick low-iron soda-lime glass sample.	x
A.2	Dielectric function of glass in the IR spectral range.	xi

List of Tables

4.1	Separation of (002) planes for different ethanol flow rates.	45
5.1	Optimized deposition parameters for ATCO and Std-TCO.	67
6.1	Data derived from Hall effect measurements for the sample with a doping ratio of 0.08 before and after biased hot plate treatment.	80
6.2	Summary and comparison of fit parameters used for simulating the reflectance data presented in Figure 2.	86
A.1	Parameterization of Gaussian peak functions used to model $Im\{\epsilon\}$ of a low-iron soda-lime glass sample.	xi

Chapter 1

Introduction

For decades the global annual consumption of primary energy has been rising [3]. Primary energy includes both non-renewable and renewable forms of energy. Whereas uranium and fossil fuels like coal, oil, and gas are assigned to the non-renewable forms, energy provided by wind, water and the sun are typically assigned to the renewable forms. In 2012 the global primary energy consumption was about $1.49 \cdot 10^{17} Wh$ [4]. Ninety-one percent of this energy demand was covered by non-renewable fuels and nine percent by renewable forms of energy. It is well known that fossil fuels are limited and that their combustion leads to climate-damaging emissions. It is highly probable that these emissions are linked to global warming [5]. It is the opinion of the author that the use of 100% renewable forms of energy is the only way to circumvent the limitations of the current global energy system.

For billions of years the sun has provided energy to our earth. This energy is partially stored in wind, ocean waves, and electromagnetic waves (light). Estimated from the solar constant, which has a value of $1367 W/m^2$, and the earth's cross-sectional area, the total power reaching earth is about $1.74 \cdot 10^{17} W$. One year's total energy amounts to $1.52 \cdot 10^{21} Wh$. Considering the global radiation balance, about one-half of this energy reaches the earth's surface, whereas the other half is absorbed, reflected or scattered by the earth's atmosphere [5]. Compared to the annual demand of primary energy in 2012 these numbers illustrate the potential of using the sunlight that reaches the surface as one source of renewable energy. Furthermore, sunlight is available everywhere on earth for free and represents an inexhaustible source of energy for mankind.

Photovoltaic technologies represent a possibility to access this energy source. With photovoltaics, sunlight is converted directly into electricity. There are different technologies available on the market, based on crystalline wafers or on thin films. In the present work the focus is on the micromorph thin-film silicon technology. This technology combines an amorphous top cell with a microcrystalline silicon bottom cell in a tandem configuration. Furthermore, the transparent conductive oxide zinc oxide (boron doped, ZnO:B) is used as the front and back electrodes. Small quantities of

abundant and non-toxic materials (silicon, zinc) are used. As a result this technology holds the potential for low production costs at a minimum risk of material shortage.

Since the year 2000 photovoltaics have experienced unprecedented growth, encouraged by the introduction of the German Renewable Energy Act (in German: Erneuerbare-Energien-Gesetz, EEG). Nowadays, photovoltaics are challenged by low prices and the demand for reliability and long-term stability. Figure 1.1 illustrates the dramatic net price reduction of solar modules based on the micromorph thin-film technology. Note, that this graph is also representative in general for other photovoltaic technologies. As can be seen the net price decreased from about 2 euros to about 50 cents within the last five years. To stay competitive, manufacturers of solar modules are continually forced to lower production costs. This can be realized by improving conversion efficiency but also by reducing material costs.

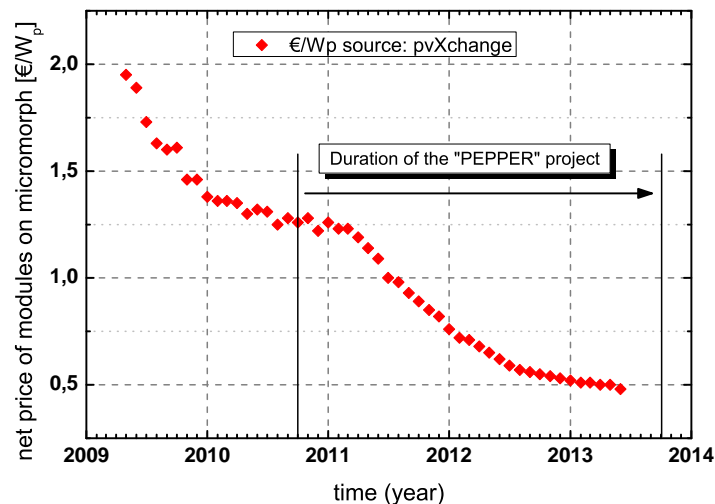


Figure 1.1: Net price reduction of solar modules based on micromorph technology.

The "PEPPER project" (Demonstration of High Performance Processes and Equipments for Thin-Film Photovoltaic Modules Produced with Lower Environmental Impact and Reduced Costs and Material Use) was aimed at improving manufacturers' competitiveness, as discussed above [6]. It addresses different facets of micromorph technology, such as the substrate glass, new and improved processes for the deposition of ZnO:B and silicon with a partly new technical design of the deposition tools, and improved reactor cleaning.

The present work was prepared in the framework of the PEPPER project. It is focused on challenges related to the optimization of the ZnO:B front electrode deposited by low-pressure chemical vapor deposition (LPCVD) for thin-film silicon solar cells. With its results, the present work contributes not only to the PEPPER project, but also to the field of research.

1.1 Contribution to the Field of Research

The morphology of the ZnO:B front electrode is of importance not only for light scattering, but also for the quality of the subsequently deposited silicon material. It is therefore of importance for the solar cell and module efficiency. The effect of using ethanol as an additional precursor during the ZnO:B layer deposition on the as-grown surface morphology is investigated. The related results are presented in Chapter 4. The present work proposes a growth model in which ethanol mediates the incorporation of oxygen at oxygen vacancy sites at the surface of the growing ZnO grains. Furthermore, the ethanol changes the reaction kinetics at the surface of the ZnO and therefore impacts the final layer morphology [7].

As a practical application, the introduction of an advanced LPCVD ZnO:B (ATCO) into the production line of Bosch Solar Thin Film GmbH is presented. The approach depicts a LPCVD ZnO:B with improved optical and electrical parameters. Here, the ZnO:B film is composed of a highly doped thin seed layer and a low-doped thicker bulk layer [1]. The corresponding results are presented in Chapter 5 and document the first results with ATCO in a commercial production line.

When new processes and functional layers are introduced, the final product (the improved solar module) has to be qualified. Beyond standardized lifetime test conditions a novel degradation phenomenon of LPCVD ZnO:B was encountered. According to IEC61646(10.13) the modules are tested in a climate chamber for 1000 hours at 85°C and 85% relative humidity. These test conditions neglect the functioning of the module under certain bias voltage conditions in the field. In addition to these test conditions, the modules were biased with 600 V against the grounded module frame (mounting system). The anodic degradation of LPCVD ZnO:B deposited on soda-lime glass was reported for the first time; the resistivity of the ZnO:B was found to strongly increase, due to an increase of defect concentration at ZnO:B grain boundaries. The resulting resistance increase of the ZnO:B is responsible for a dramatic efficiency loss in tested solar modules. Oxygen generation at the ZnO:B/glass interface during the degradation procedure will be discussed as a root cause for the increase of the defect density at ZnO grain boundaries. The corresponding results are presented in Chapter 6. Furthermore, solutions to minimize the degradation, minimizing the degradation are proposed and discussed [8,9].

The present work is structured as follows:

In **Chapter 2** the principles of thin-film silicon photovoltaics are introduced. The material properties and the deposition processes of zinc oxide and amorphous and microcrystalline silicon are presented. Micromorph solar cells and modules and their working principles are introduced.

Chapter 3 presents the main characterization techniques used for the investigations in the present work. It is separated into four sections. The first three summarize

the optical, electrical and structural techniques related to layer characterization. The fourth covers the characterization of solar cells and modules.

In **Chapter 4** results of the investigations using ethanol as an additional precursor to modify the ZnO:B surface morphology are presented.

Chapter 5 presents the introduction of an advanced transparent conductive oxide (ATCO, based on ZnO:B) into the production line at Bosch Solar Thin Film GmbH in Erfurt, Germany.

In **Chapter 6** the anodic degradation of ZnO:B on soda lime glass is discussed.

Finally, in **Chapter 7** the results are summarized.

Chapter 2

Principles of Thin-Film Silicon PV

It is the goal of this chapter to present a brief introduction to the main technology used for preparing micromorph solar cells and modules. Furthermore, for a better understanding of results presented later, important material properties will be discussed and summarized. The cells and modules investigated were prepared in the so-called superstrate configuration [10]. That means that the glass substrate used for the deposition of the required layer stack not only acts as a pure substrate but also as the entrance window for the light to be converted into photocurrent. In our case, the first layer to be deposited on the glass substrate is zinc oxide (ZnO) a transparent conductive oxide (TCO). Details on deposition and material properties will be discussed in Section 2.1. After the ZnO layer is processed, the silicon cell structure is deposited. The material properties and deposition process will be introduced in Section 2.2. Finally, the concept of micromorph solar cells and modules will be presented in Section 2.3.

2.1 Zinc Oxide -

Deposition and Material Properties

ZnO possesses unique properties, which make it suitable not only for photovoltaic applications, but also for devices such as gas sensors, light-emitting diodes, varistors or sound acoustic wave applications [11]. It possesses high transparency in the visible and near-infrared spectral region. In most cases ZnO is a semiconductor of n-type conductivity. Due to intrinsic defects such as zinc interstitials or oxygen vacancies and extrinsic doping elements such as aluminum (Al) or boron (B), the free-electron concentration can typically be adjusted in a range between 10^{19} and $10^{21} 1/cm^3$. This yields resistivity values lower than $10^{-3} \Omega cm$. For industrial photovoltaic applications it is necessary to deposit ZnO on large substrates. In the case of micromorph module fabrication, substrate sizes of $1.4 m^2$ are used. In addition to the already mentioned high transparency, ZnO's light-scattering ability is important for yielding highly efficient thin-film solar cells. The production process technology based on chemical vapor

deposition at low pressures (LPCVD) meets all the requirements of the micromorph modules concept.

2.1.1 Deposition of Zinc Oxide by LPCVD

Due to the complexity of the process of ZnO deposition using chemical vapor deposition (CVD) [12–16], only an introduction is presented here in order to show the reader the principles of this technology and the growth regime used for sample fabrication in the present work. Metal-organic compounds such as diethylzinc (DEZ, $(C_2H_5)_2Zn$) or dimethylzinc (DMZ, $(CH_3)_2Zn$) as a source of zinc (Zn) and molecular oxygen (O_2) or water (H_2O) as a source of oxygen are typically utilized as precursors for ZnO film deposition, by means of CVD. Also other precursors are possible, e.g. zinc acetylacetonate [17], alcohols [7, 18–24] or nitrogen oxygen compounds [25, 26]. The present work will focus on DEZ and water only.

The deposition of ZnO, using a CVD process, is a result of sophisticated chemical vapor phase reactions followed by the nucleation of reaction intermediates and finally of the adsorption of reaction products on the substrate surface [12–14]. At the surface of the substrate the cluster formation and growth of single ZnO grains strongly depend on the growth conditions which are mainly determined by substrate temperature, process pressure and precursor flow rates. Here, the mobility of adatoms or clusters, which is of importance during layer growth, significantly influences the final layer properties, as e.g. morphology [15, 16, 27]. The morphology is of major importance for photovoltaic applications, as will be discussed later.

In comparison to other oxygen precursors mentioned above, water possesses a high reactivity in combination with DEZ. This is illustrated in Figure 2.1. Indeed, DEZ already ignites at atmospheric pressure and low ambient temperatures due to the presence of ambient oxygen and humidity, as shown in Figure 2.1a. If liquid water is added to the DEZ-containing box, a strong and fast reaction follows, as the reaction is not limited by the low availability of water as oxidation agent, see Figure 2.1b.

In high-pressure CVD, which is usually associated with atmospheric pressure (APCVD), pre major reactions occur in the vapor phase due to the high reactivity between DEZ and water. These lead to the formation of dust (ZnO particles) within the deposition chamber and to a bad layer quality [11] pp. 238 – 240. Also the layer uniformity, which is the distribution of layer properties across the deposition area, is adversely affected. In the high-pressure regime, the growth of the ZnO layer is diffusion- rather than kinetics-limited. That means that the growth is limited by an insufficient transport of reactants to the growing surface. Improvements regarding layer quality and growth rate were achieved by reducing the deposition pressure. When the deposition process becomes kinetics-limited, the reaction rate between the DEZ and water is reduced. In turn, an increased number of reactants in the form of precursors and intermediates

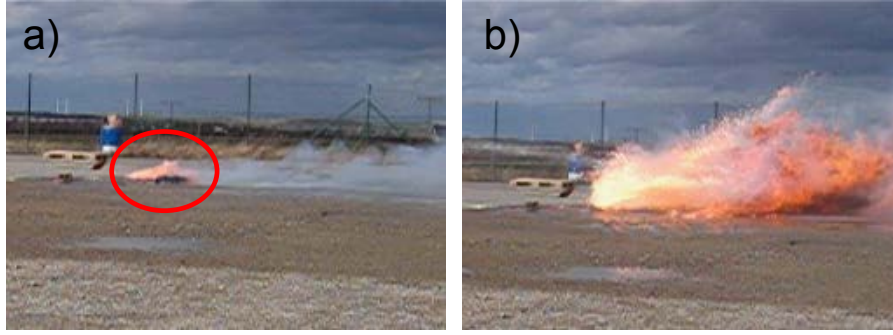
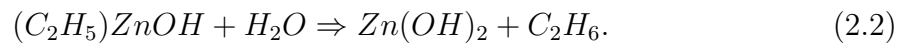
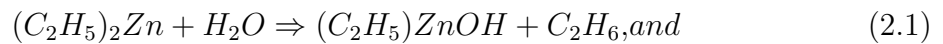


Figure 2.1: Demonstration of high reactivity between DEZ and water at atmospheric pressure and at an ambient temperature of about 15°C. (a) DEZ ignites already due to the presence of ambient oxygen and humidity. (b) Adding liquid water to the DEZ-containing box leads to a strong and fast reaction.

reach the substrate surface. Due to the reduced process pressure the probability of vapor phase reactions is reduced caused by the lower density of reactants. One can think also of an increased length of mean free path before a water molecule meets a DEZ molecule in order to react. In fact, the process of deposition became easier to be controlled. The low-pressure CVD (LPCVD) process, which is associated with pressures below 10 mbar and which is similar to the process used in the present work, was intensively studied by Fay et al. [15, 27–30]. The reader is referred to these references to get more information about the impact of the precursor flow ratio, deposition temperature and pressure on final ZnO layer properties. Nowadays a pressure of about 0.5 mbar has been found to be suitable for LPCVD ZnO layer deposition not only for laboratory but also for industrial application.

Smith et al. [13] and Kim et al. [14] made theoretical calculations to find the paths of reactions that are likely to occur between DEZ and water. Besides other possible reaction paths and emerging intermediates they identified the reaction paths shown in Equation 2.1 and 2.2 to be highly likely in the vapor phase:



Zinc hydroxide ($Zn(OH)_2$) is assumed to play a key role for the formation of ZnO. Here, due to oligomerization of zinc hydroxide and the elimination of hydrogen, nuclides or clusters emerge. Adsorbed on the substrate surface they are responsible for ZnO layer growth during the CVD process. In the following section, the deposition tools used in the present work are introduced. After that, the general material properties of LPCVD ZnO will be presented.

2.1.1.1 Small Single-Chamber Deposition System

In Figure 2.2 a single-chamber LPCVD deposition tool is presented. The small system is located at the Institute of Microengineering (IMT) in Neuchâtel, Switzerland. In the present work the system was used for all preparations for the investigations of the suitability of ethanol to modify the surface morphology of the final LPCVD ZnO layer during the deposition. Results on that are presented in Section 4.

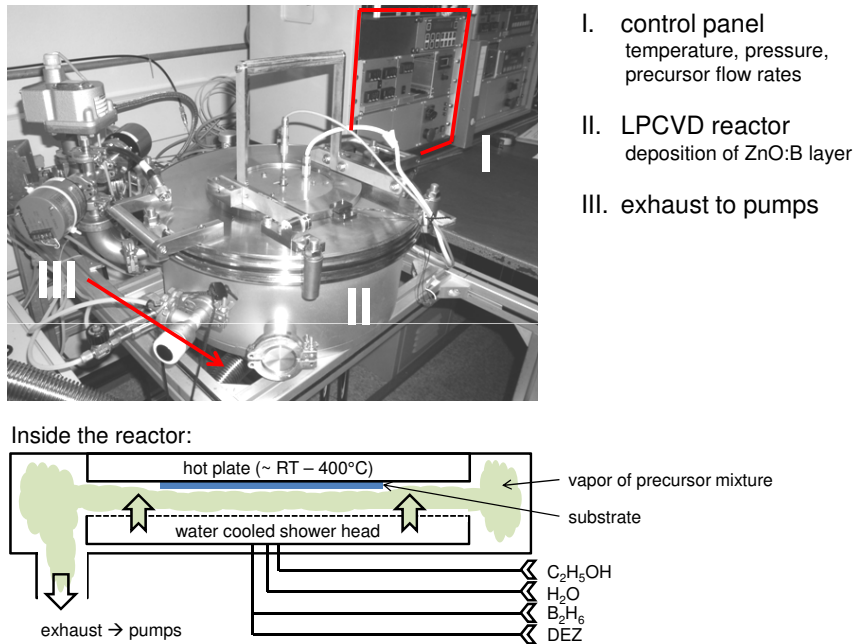


Figure 2.2: Small LPCVD system in the PV-Lab at the Institute of Microengineering in Neuchâtel (IMT) used for investigation of the suitability of precursor ethanol during the deposition of ZnO from DEZ and water, see Section 4.

The deposition system is composed of three major components: the control panel (I), the reactor (II) and the exhaust (III), which connects the reactor and system vacuum pumps. A schematic view into the LPCVD reactor (II) is shown at the bottom of Figure 2.2. The reactor is about 50 cm in diameter and about 25 cm in height. As shown, the shower head, responsible for mixing the precursors before entering the reactor zone between the shower head and the substrate, is located at the bottom of the reactor. The hot plate, on which the substrate is fixed, is located at the top of the reactor. The deposition system is suitable for substrates with a size of about $5 \times 5 \text{ cm}^2$. Note that the substrates used here are borosilicate glass slices (0.5 mm thick). They were cleaned in a bath of an acidic solution followed by one in an alkaline solution. The baths were enhanced by ultrasonic treatment. Afterward, the substrates were rinsed with deionized water and dried in air.

The temperature of the hot plate can be varied between room temperature (RT)

and 400 °C. In the present case the temperature was set to 175 °C, unless indicated otherwise. DEZ, water and ethanol (C_2H_5OH) were used as precursors. The doping gas source used was diborane (B_2H_6) diluted at 1% in argon. Argon was used not only for dilution but also as a carrier gas. It is assumed to have a negligible impact on the deposition process. The deposition pressure can be regulated in a range between 0.1 and 1 *mbar* with a butterfly valve. For the deposition of LPCVD ZnO:B, which is suitable for thin-film silicon solar cells, a pressure of 0.5 *mbar* was set. Without using ethanol, typical deposition rates between 2.5 and 3 *nm/s* were achieved. For more process details regarding the small deposition system presented here, see Section 4.

2.1.1.2 Large Deposition System (TCO1200)

The TCO1200 deposition tool, which is used for the large-size industrial photovoltaic application at Bosch Solar Thin Film GmbH (BSTF), is shown in Figure 2.3. In the present work the tool is used for the introduction of an advanced LPCVD ZnO:B into the production line at BSTF. Results will be presented in Section 5. The tool is also used for solar module and sample fabrication during the investigation of anodic degradation of ZnO:B on soda-lime glass. For results see Section 6. The TCO1200 tool enables us to deposit LPCVD ZnO:B on glass substrates with a size of $1.1 \times 1.3 \text{ m}^2$. Note that the substrate used for solar module and sample fabrication is a low-iron soda-lime glass with a thickness of 3 to 3.2 *mm*. Before front contact layer deposition, the substrates were cleaned in a bath of an alkaline solution. The cleaning process was enhanced by ultrasonic treatment. Afterward, the substrates were rinsed with deionized water and dried with a clean air flow.

The TCO1200 deposition system is about 15 *m* long and a weights about 40 tons. The main components are the load lock followed by four process modules (PM1–4) and the unload lock. Leaving the unload lock the ZnO:B-covered substrates cool down at atmospheric ambient conditions. Below the deposition tool, a transfer back to the starting point is realized. Afterward, the substrates are handled further by an automated production line control system.

In order to cycle through the deposition process, a cleaned substrate, provided by the automated production line control system, is transferred into the load lock at ambient pressure. After the transfer is completed, the pressure is reduced down to regime of deposition, which is around 0.5 *mbar*. At the same time an infrared radiation heater increases the substrate temperature from ambient temperature to 170 to 180 °C. This step is realized within less than 2 minutes. Now the pre-heated substrate is transferred into PM1 and another substrate enters the load lock immediately after the transfer has completed. Contrary to the reactor geometry of the small deposition system described in Section 2.1.1.1, in the process modules of the LPCVD tool TCO1200 the hot plate is placed at the bottom and the shower head is placed at the top of the process module.

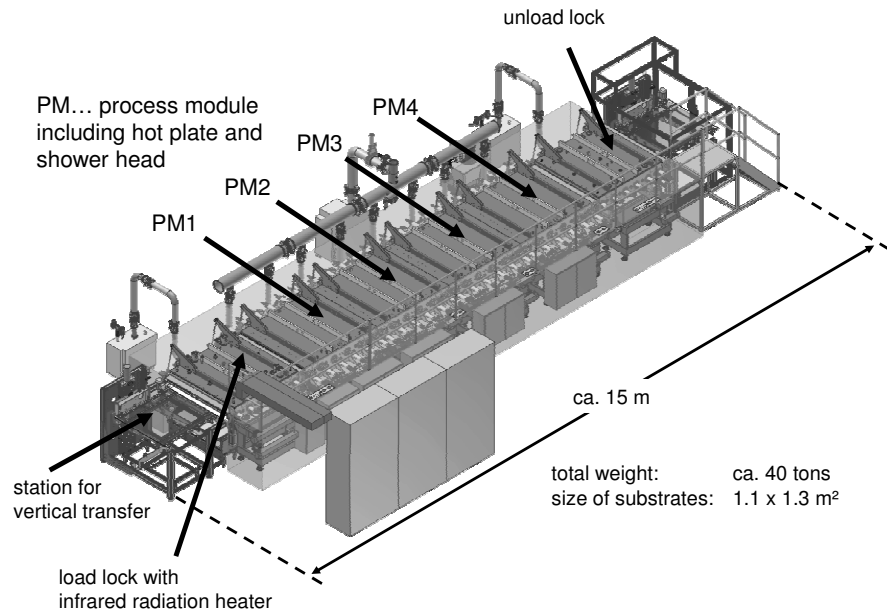


Figure 2.3: TCO 1200 deposition system from Tokyo Electron Solar AG, formerly Oerlikon Solar (Source: TEL Solar AG). The LPCVD tool was used in the standardized production line of Bosch Solar Thin Film GmbH for the deposition of ZnO front and back electrodes.

This geometry simplifies the handling of the large substrates, since the substrates on the hot plate are fixed by their own weight. In PM1 only a quarter of the final layer thickness is deposited. In each process module a further quarter is deposited. PM2 to PM4 possess the same deposition conditions as PM1. There is no valve that separates each process module. The approach using four process modules maximizes the utilization of the load lock module. Here, the rate of heating and in total the time of transferring substrates into the deposition process is about four times lower than the time (deposition rate) required for the entire ZnO layer deposition. The task of the unload lock module is to transfer the ZnO-covered substrates back to normal ambient conditions.

Similar to the deposition introduced for the small deposition system, for the ZnO:B deposition with the TCO1200, water, DEZ and diborane were used as precursors. The hot plate temperature was set to 188 °C, which is hotter than that used by the small deposition tool. This is explained by the thicker substrate used for LPCVD ZnO:B deposition by using the TCO1200. Nevertheless suitable deposition rates of about 3 nm/s were achieved. More specific deposition details will be mentioned in sections the tool is used.

2.1.2 Structural Properties

ZnO is a group II-VI binary compound semiconductor. Its lattice structure is illustrated in Figure 2.4a and 2.4b. The hexagonal wurtzite structure of ZnO is composed of two interpenetrating hexagonal-close-packed (hcp) sub-lattices. Each sub-lattice is occupied by only one type of atom (zinc or oxygen). These sub-lattices are displaced parallel to c-axis by a value of $3/8$ in units of "c". The lattice constants "a" and "c" for the wurtzite-structured ZnO at room temperature are determined from various experimental measurements and range for "a" from 3.2475 to 3.2501 Å and for "c" from 5.2042 to 5.2075 Å [31]. These values can significantly differ in the presence of stress induced thermally or mechanically. But the stoichiometry also influences the lattice constants. For ZnO the wurtzite structure at ambient condition is the most stable phase, whereas under certain conditions the lattice structures of cubic rocksalt or zinc blende are known for ZnO, as well [31].

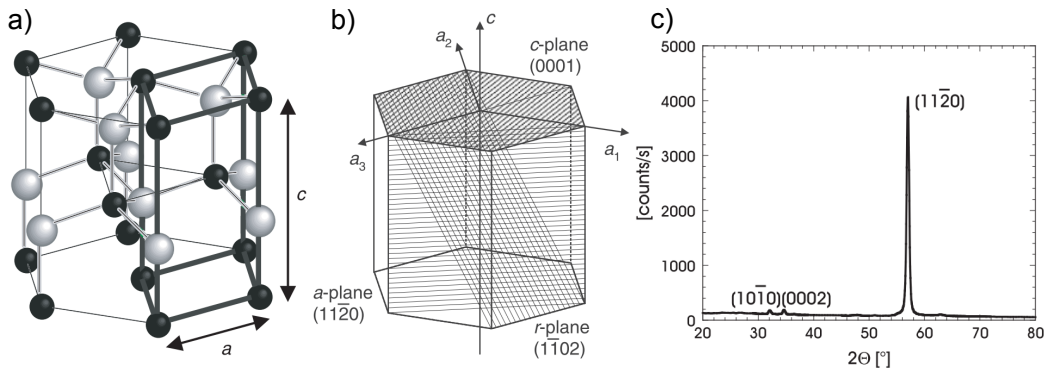


Figure 2.4: (a) Hexagonal wurtzite-structured lattice of ZnO. The primitive cell (heavy lines) is indicated. "a" and "c" are the lattice constants. (b) Drawing of surface planes of different crystallographic orientations of the hexagonal wurtzite structure [11] p. 82. (c) X-ray diffraction of a 2- μm -thick LPCVD ZnO:B layer deposited at 155°C and 0.5 mbar [11] p. 243.

In Figure 2.4c one can see that grains with (1120) orientation dominate the diffraction pattern. Note that the texture of LPCVD ZnO strongly depends on the deposition conditions and is usually a function of layer thickness [16, 27]. In the diffraction diagram the peak at an angle of 56° identifies the a-plane of hexagonal wurtzite-structured ZnO.

In Figure 2.5 one can observe that a ZnO film deposited by LPCVD is composed of many grains. Such a polycrystalline LPCVD ZnO film with its unique as-grown rough surface morphology possesses a crystallographic texture, a preferred orientation of the crystalline grains grown on the glass substrate. This texture is illustrated in a diffraction pattern in Figure 2.4c.

In Figure 2.5 images made by scanning electron microscopy (SEM) of a LPCVD ZnO:B layer, as it is typically used for thin-film solar cell applications, are shown. Figure 2.5a shows the top view of the as-grown layer, and a cross section of the layer,

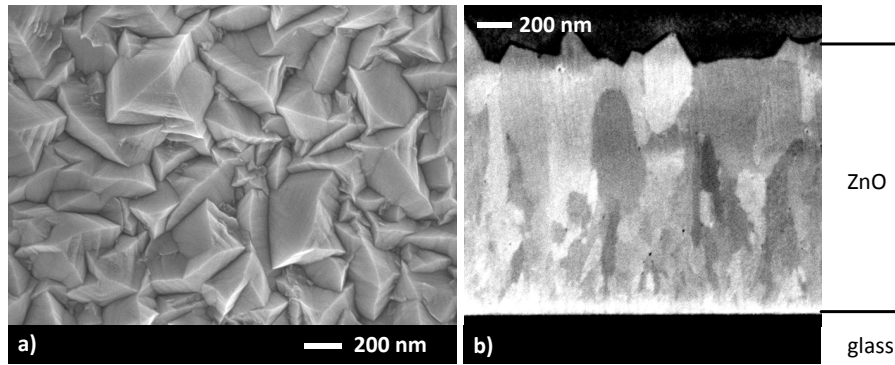


Figure 2.5: SEM images of a standard ZnO layer typically used as a front electrode for thin-film solar cells. (a) The top surface morphology. (b) A cross section of the layer prepared by a focused ion beam.

which was prepared by a focused ion beam, is shown in Figure 2.5b. From the cross-sectional image one sees the ZnO layer to be polycrystalline. The ZnO layer on the substrate surface starts to grow with small grains. During the growth, some of the grains survive and become bigger while the smaller ones become covered by the bigger ones. The growth process of LPCVD ZnO is a process away from thermal equilibrium. It is based on the evolutionary selection theory with kinetic growth aspects. It relies on the growth rate anisotropy of different crystallographic planes of the ZnO material. A growth model for polycrystalline LPCVD ZnO is discussed in more detail by Nicolay et al. [16]. The surface of the ZnO layer is dominated by the bigger grains. These determine the as-grown rough surface, which is of importance for light scattering, as it directly influences the photogenerated current.

2.1.3 Electrical Properties

Only basic informations are summarized in the following section. The reader is referred to the literature for more details [11,31–33]. ZnO deposited by LPCVD is a degenerated n-type semiconductor, meaning the Fermi level is within the conduction band. The quantity and mobility of free electrons determine the conductivity of the deposited material. The free-electron concentration is determined by intrinsic and extrinsic lattice defects and typically can be adjusted for LPCVD ZnO to a range of 10^{19} to 10^{21} cm^{-3} . Intrinsic defects such as zinc interstitials (Zn_i) or oxygen vacancies (O_V) are a result of defective growth and are inherently incorporated in the ZnO material. They act as intrinsic donors and are assumed to deliver electrons to the conduction band of the ZnO material [11] p. 38. Extrinsic donor type defects are assigned to foreign atoms (impurities) which are incorporated in the lattice structure. In ZnO they replace either zinc or oxygen at their respective lattice sites. Elements of group III such as boron (B), aluminum (Al), gallium (Ga) or indium (In) are known to act as donors if incorporated in the ZnO lattice structure. They replace zinc and donate the additional electron not required for bonding to the conduction band. For LPCVD ZnO, which is deposited at

temperatures below 200°C, diborane (B_2H_6) was found to be a suitable extrinsic doping source. When diborane is used as an additional precursor, the electron concentration and as a result the resistivity can easily be tuned.

The mobility of electrons is of major importance to achieve suitable resistivity values. For LPCVD ZnO:B used in photovoltaic applications and in the present work, typical mobility values are around $30\text{ cm}^2/Vs$. The mobility of electrons is a measure of their scattering probability while moving through the material. There are several scattering mechanisms known to reduce the electron mobility [11, 31]. For example, ionized impurity scattering occurs due to the deflection of electrons by long-range coulomb potentials. These are induced by charged defect centers or intentionally doped impurities, e.g. ionized boron atoms within the lattice structure of ZnO. Another form of scattering is induced by electron phonon interaction. Here, one distinguishes between optical and acoustical phonon scattering. While for optical phonon scattering the electron interacts with the electrical field induced by the lattice vibration, for acoustical phonon scattering the electrons are scattered by the lattice deformation, which induces a local energetic shift of the band edge. Other scattering mechanisms are piezoelectric scattering and the scattering induced by lattice dislocations (crystal defects). Piezoelectric scattering occurs due to the interaction of electrons with an electric field that is induced by the presence of stress in the material.

In polycrystalline materials such as in LPCVD ZnO thin films, a vast number of grains and as a result of grain boundaries is present. Here, the consideration of scattering of free charge carriers (electrons) at grain boundaries is of importance if one discusses electrical properties. According to the model of Seto [34] trap states at the grain boundaries are responsible for trapping free electrons from the near grain bulk material. These cause the creation of a negatively charged interface layer and the formation of a back-to-back Schottky potential barrier. Figure 2.6 shows a schematic band diagram illustrating a one-dimensional grain model and the idealized situation at the grain boundaries. Electrons crossing the grain/grain interface have to overcome the barrier by thermionic emission or by tunneling.

The barrier is characterized by its height (Φ_B) and width (W). An expression for both is given in Equation 2.3 and 2.4 [34]:

$$\Phi_B = \frac{e^2 N_t^2}{8\varepsilon\varepsilon_0 N_e}, \text{ and} \quad (2.3)$$

$$W = \frac{N_t}{N_e}. \quad (2.4)$$

where e is the elementary charge of electrons, N_t the trap density at the grain boundaries, ε the dielectric permittivity of the material, ε_0 the dielectric permittivity of free space and N_e the free-electron concentration. One can see that Φ_B and W are proportional to the density of traps, whereas they are inverse proportional to the free-electron

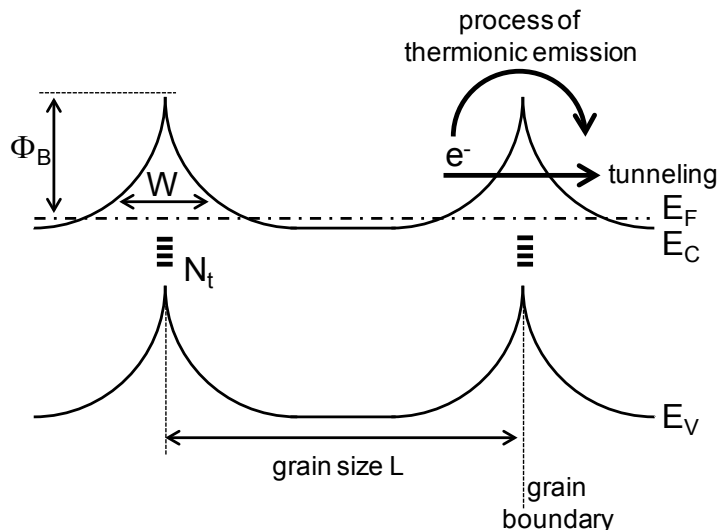


Figure 2.6: Linear band diagram of grains of the length L and electron concentration N . The presence of trap states with a density N_t causes barriers of the height Φ_B at the grain boundaries [34]. Different transport paths for electrons are indicated: thermionic emission across the barrier; tunneling through the barrier. See Refs. [11] p.59 and [35]

concentration. In other words, for a constant trap density, a high concentration of electrons decreases the influence of grain boundary scattering on the electrical properties of a polycrystalline material. Steinhauser et al. applied the abovementioned theory to LPCVD ZnO:B as it is used in the present work [35–38]. For an as-grown trap density, they found the mobility of electrons to be limited by intra-grain (impurities,...) scattering for high ($> 10^{20} \text{ cm}^{-3}$) and by grain boundary scattering for low ($< 10^{20} \text{ cm}^{-3}$) electron concentrations. They further reported a typical concentration of trap states at the grain boundaries to be in the range of 10^{12} to 10^{13} cm^{-2} . As will be discussed later the process of grain boundary scattering is of central importance for the results presented in Chapter 6.

2.1.4 Optical Properties

In Figure 2.7 transmittance and reflectance data are presented from the ultraviolet (UV) to the far infrared (IR) spectral region for LPCVD ZnO:B deposited on a soda-lime glass substrate. Furthermore, ranges of optical features which will be discussed in the following are indicated. For simplification the influence of the substrate is neglected. The spectra shown in Figure 2.7 include a lot of characteristic information about the ZnO material. Note that the spectral range used for micromorph solar cell application is small, reaching from the absorption edge of the ZnO to the absorption edge of the microcrystalline silicon absorber material at about 1100 nm . More information about the silicon absorber is summarized in Section 2.2.

The optical absorption edge of ZnO is located between 350 and 400 nm . Here, incoming photons with energies equal to or higher than the energetic position of the

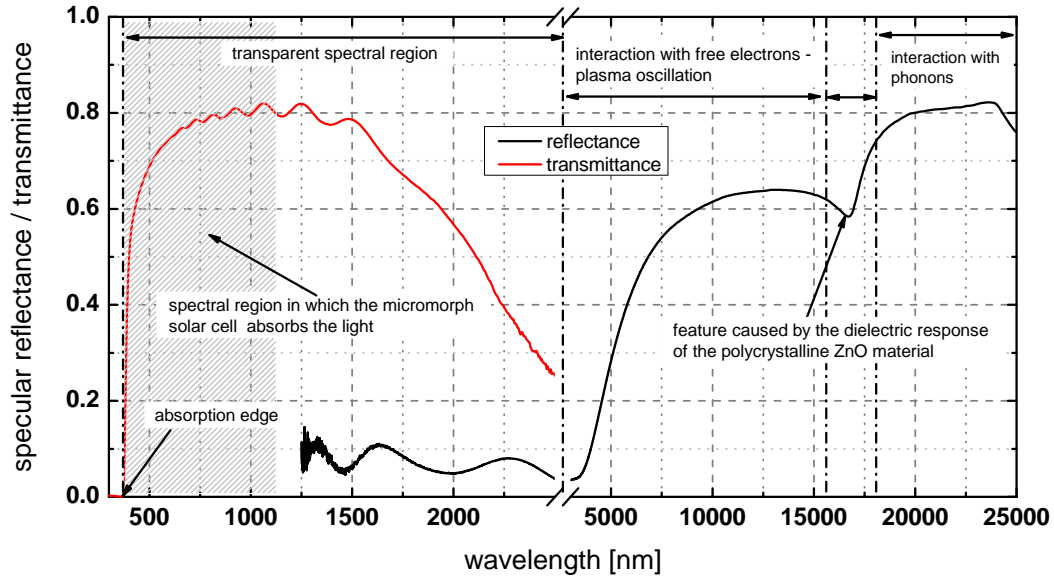


Figure 2.7: Transmittance and reflectance of LPVCD ZnO deposited on a glass substrate. Typical features for the LPCVD ZnO are indicated.

absorption edge are typically absorbed due to the excitation of electrons from the valence to the conduction band. The absorption edge is correlated with the bandgap of the material. For the bandgap of ZnO, which is assigned to a direct transition between the highest valence to the lowest conduction band, energy values ranging from 3.19 to 3.44 eV are reported [11] p. 111. There are several mechanisms known to affect the energetic position of the absorption edge of ZnO. The first and most frequently mentioned effect is the shift of the absorption edge according to Burstein-Moss [35,39]. Due to the high electron concentration, which is in a range between 10^{19} and 10^{21} cm^{-3} , the bottom states of the conduction band are occupied. As a result the photons need to have more energy in order to transfer additional electrons from the valence to the conduction band. Usually the absorption edge shifts with higher electron concentration to higher energies (shorter wavelengths) [35]. But also defect absorption and the deformation of the lattice structure caused by internal or external stress affect the position of the absorption edge [40,41].

Subsequently to the edge of absorption, the transparent spectral region follows for longer wavelengths (lower photon energies). As mentioned above, this region is the most important for solar cell applications, since the transmission of photons directly determine the photocurrent of the solar cell. In the transparent region, incoming photons pass the ZnO material with a minimum of losses. Due to the wave character of the incident light, interference oscillations are observed. They are a result of the coherent superposition of the electromagnetic light waves reflected at the air/ZnO and at the ZnO/glass interfaces. At longer wavelengths, transmission decreases. This is a result of the starting interaction between free electrons and the electric field of the incoming electromagnetic light wave. As will be explained later in more detail, this

phenomenon can be treated by the well-known Drude Theory [35, 42–45].

Between 2.5 and about 15 μm , a strong increase of reflection can be observed. Here, for frequencies between 20 and 120 THz the free electrons are able to follow the oscillating electric field of the light waves. With the onset of strong reflection the penetration depth of the electromagnetic waves is drastically reduced. No electromagnetic waves if still reflected at the ZnO/glass interface contribute to the formation of interference fringes. This is indicated by the disappearance of the interference fringes, which are observed only in the transparent spectral region. The position of the reflection edge and its shape depends on the concentration and on the mobility of electrons, respectively. Whereas with a higher concentration of electrons the reflection edge shifts to shorter wavelengths and vice versa, the slope of the reflection edge increases the higher the mobility of the interacting free electrons and vice versa.

The second reflection edge above 17 μm marks the interaction of optical phonons with electric field oscillations of electromagnetic waves. This band of high reflection is known as Reststrahlen (residual rays) band reflection [42, 46].

A last feature which was found to be of interest during the course of the present work was the dip in the reflection spectrum located at about 17 μm . Recently, Prunici et al. explained that the dip is due to the dielectric response of the polycrystalline ZnO:B material [46]. Prunici's approach will be introduced in Section 2.1.5. As a result one obtains a dielectric response function which includes the features mentioned above and enables the simulation of the reflection spectra shown in Figure 2.7. The fit parameters extracted and their interpretation are in agreement with electron transport theory introduced by Seto [34] and discussed in Section 2.1.3.

2.1.5 Dielectric Function of Polycrystalline LPCVD ZnO:B

The dielectric function (DF), $\epsilon(\omega)$, of any material is known to be a complex function describing the interaction between an incoming electromagnetic wave and the interacting material. According to the relation $\underline{n} = \sqrt{\epsilon} = n + ik$ the refractive index (n) and the extinction coefficient (k) can be calculated. If the DF of the material is known, in combination with Fresnel's equations, one is able to calculate transmission, absorption and reflection of an incoming electromagnetic wave. The reader is referred to related textbooks for more details [42, 47, 48]. Note that it is necessary to know the DF of each layer including the substrate and the surrounding medium, if for example the transmission or reflection of a stack of layers has to be calculated. The DF of our glass substrate was determined separately and will not be discussed further, since the focus of the present work is on the ZnO material. For more information on the DF of the glass the reader is referred to the Appendix A. For ZnO in the IR spectral range to 25 μm one has to consider three major dielectric contributions. These are summed up in Equation 2.5:

$$\epsilon(\omega) = \epsilon_{\infty} + \epsilon_{pl} + \epsilon_{ph}. \quad (2.5)$$

ϵ_{∞} is the high-frequency dielectric constant and is associated with oscillators in the high-frequency range, which do not directly influence the optical spectral range investigated. ϵ_{pl} and ϵ_{ph} are the dielectric contributions of the free electrons and phonons, respectively. These are defined in Equation 2.6 and 2.7:

$$\epsilon_{pl} = -\frac{\omega_{pl}^2}{\omega^2 + i\Gamma_{pl}\omega}, \text{ and} \quad (2.6)$$

$$\epsilon_{ph} = \frac{\omega_{LO}^2 - \omega_{TO}^2}{\omega_{TO}^2 - \omega^2 + i\Gamma_{ph}\omega}. \quad (2.7)$$

Here, ω_{pl} is the plasma mode frequency and Γ_{pl} is the corresponding damping constant. ω_{TO} and ω_{LO} are the resonance frequencies of the transversal and longitudinal optical phonon modes, respectively. Γ_{ph} is the damping constant of the phonon dielectric contribution.

The proposed DF would be sufficient to describe an isotropic, monocrystalline ZnO. However, it fails when describing a polycrystalline ZnO possessing a free-electron concentration on the order of 10^{19} cm^{-3} . In order to overcome these limitations and to model IR reflectance of ZnO:B deposited by LPCVD, Prunici et. al. [46] proposed to describe the DF of a polycrystalline ZnO layer as an effective medium according to the theory of Maxwell-Garnett [49, 50]. It is assumed that the ZnO grain bulk/core material (as spherical inclusions) is embedded in a ZnO host material, namely the ZnO grain boundary material. Both the grain bulk and boundary material are modeled by their respective DF, according to Equation 2.5. The resulting DF according to Maxwell-Garnett is calculated from Equation 2.8:

$$\epsilon(\omega) = \epsilon_{bnd} \frac{\epsilon_{blk} + 2\epsilon_{bnd} + 2f_{blk}(\epsilon_{blk} - \epsilon_{bnd})}{\epsilon_{blk} + 2\epsilon_{bnd} - f_{blk}(\epsilon_{blk} - \epsilon_{bnd})}, \quad (2.8)$$

where ϵ_{blk} and ϵ_{bnd} are assigned to the individual DFs of the ZnO grain bulk and boundary material, respectively. f_{blk} is the volume fraction of the ZnO grain bulk material. f_{bnd} , the volume fraction of the ZnO grain boundary material, can be calculated according to Equation 2.9:

$$f_{bnd} = 1 - f_{blk} \quad (2.9)$$

Again, ϵ_{blk} and ϵ_{bnd} are independently determined according to Equations 2.5 to 2.7.

From the fitting process of simulated and measured optical spectra, important parameters such as the plasma mode frequency (ω_{pl}) and the damping constant (Γ_{pl}) can be derived. As can be seen from Equation 2.10 and 2.11, these parameters allow us to determine the free-electron concentration (N_e) and electron optical mobility (μ_{opt}):

$$N_e = \frac{\omega_N^2 \epsilon_0 \epsilon_\infty m^*}{e^2} = \frac{\omega_{pl}^2 \epsilon_0 m^*}{e^2}, \quad \omega_N^2 = \frac{\omega_{pl}^2}{\epsilon_\infty}, \text{ and} \quad (2.10)$$

$$\mu_{opt} = \frac{m^*}{e \Gamma_{pl}}, \quad (2.11)$$

where e , ϵ_0 and m^* are the elementary electron charge, the permittivity of the vacuum and the effective electron mass, respectively. ω_N is the plasma mode frequency, as well. It results from putting ϵ_∞ in Equation 2.5 out of the brackets.

2.2 Silicon Thin Films - Deposition and Material Properties

On the following pages a brief introduction into thin-film silicon technology will be given. The deposition process is introduced in Section 2.2.1. Afterward, the material properties of amorphous and microcrystalline silicon will be briefly summarized in Sections 2.2.2 and 2.2.3, respectively.

2.2.1 Deposition of Silicon Thin Films by Plasma-Enhanced Chemical Vapor Deposition

For the industrial fabrication of silicon thin films on large substrates ($1.1 \times 1.3 m^2$, in our case), the technology of plasma-enhanced chemical vapor deposition (PECVD) is utilized. In the present case the main precursors required for the deposition of silicon are silane (SiH_4) and hydrogen (H_2). Other precursors such as silicon tetrachloride ($SiCl_4$), dichlorosilane (SiH_2Cl_2) or silicon tetrafluoride (SiF_4) are also reported for thin-film silicon deposition [51–54].

Silane usually dissociates at temperatures above $450^\circ C$. Thus, only substrates resisting high temperature are suited for the deposition of silicon thin films. During the PECVD process a continuous flow of precursors is forced to dissociate before reaching the substrate surface. In the gas phase a plasma is generated [55]. The plasma is powered by an external power source. This approach has an advantage, since the temperature of the substrate can be chosen independently from the dissociation temperature of the precursors. The substrate temperature for the deposition of silicon thin films by PECVD is typically adjusted to a range between 150 and $200^\circ C$. The plasma required for the dissociation is generated between coplanar-arranged electrodes. The deposition setup is shown in Figure 2.8. Utilizing an alternating electric field with a frequency of $40 MHz$ applied to the electrodes, enables the deposition of thin films on isolating substrates. Whereas the upper electrode in Figure 2.8 is used as the input electrode, the bottom electrode, as well as the rest of the reactor, is grounded. The

supply of the reactor with precursors is realized with a circuit of small pipes within the upper electrode. Using a butterfly valve in the exhaust, the process pressure is adjusted to about 0.5 mbar. A characteristic feature of the deposition system is the Plasma-Box-Principle[©] by Tokyo Electron Solar AG. As one can see in Figure 2.8 the reactor is a plug-in unit in a process module. The deposition reactor and process module are separately pumped, in order to achieve a slightly higher process pressure within the reactor. As a result contamination of the reactor and the implementation of foreign atoms within the deposited silicon layers can be minimized.

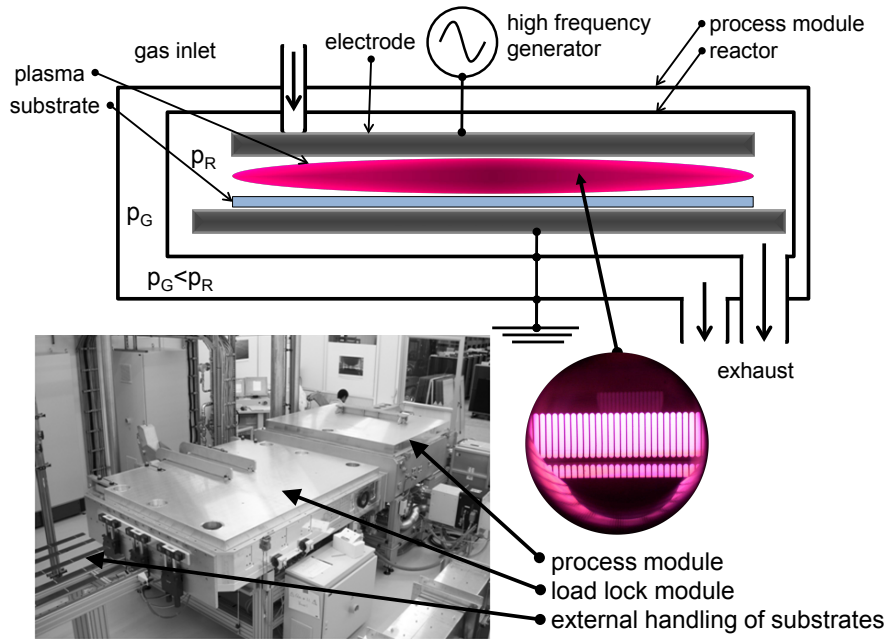
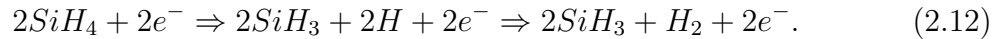


Figure 2.8: Research and development tool for large-size ($1.1 \times 1.3 \text{ m}^2$) deposition of thin-film silicon solar cells and modules by PECVD. The top part of the figure sketches the process module including the PECVD reactor. The representation illustrates the Plasma-Box-Principle[©] of the Tokyo Electron Solar AG, formerly Oerlikon Solar. p_r and p_g are the pressure inside the reactor (process pressure) and the pressure of the process module, respectively. The photograph at the bottom right shows the plasma, an insight into the reactor during a deposition process.

At the bottom left of Figure 2.8 a photograph of the PECVD system, which was used in the present work and as a research and development tool at Bosch Solar Thin Film GmbH for solar cell and module fabrication, is shown. One can see the process module, in which the reactor is placed. It is interconnected with a load lock module. The load lock realizes the transfer of substrates from and into the deposition reactor.

Within the plasma zone (electrode gap) silane and hydrogen are excited to dissociate. In addition to ionized atoms and molecules, electrons and neutral particles in the plasma phase are available. The neutral species are typically non-dissociated precursors or reaction intermediates. In sum of positively and negatively charged species the plasma is electrically neutral. In a low-pressure plasma regime, the species important for layer growth arise from the interaction with electrons. The following equation shows

only one possible reaction path [55]:



SiH_3 as a reaction intermediate is assumed to play a major role in the deposition of silicon. On their way to the surface of the growing silicon layer, reaction intermediates are influenced by many interactions. Here, secondary reactions might occur that lead to the formation of further intermediates. On the one hand some of them will support layer growth, but on the other hand some of them will cause the formation of dust (silicon dust) influencing the final layer quality [55]. Nevertheless, due to a certain set of deposition parameters, the fabrication of amorphous and microcrystalline silicon films and their photovoltaic application are possible [10, 56, 57].

2.2.2 Amorphous Silicon

The process of the deposition of the amorphous silicon (a-Si:H) was first described by R. Chittick et al. and later investigated in more detail by W. E. Spear et al. [58, 59]. "a-Si:H" indicates that the deposited silicon film contains a lot of hydrogen. The content of hydrogen in a-Si:H layers is reported to be between 10 to 20 At% [55]. The main feature of the a-Si:H matrix is a missing long-range order of the silicon atoms, whereas the near order can be compared with that of crystalline silicon [60]. Furthermore, the material features a high amount of coordination defects for example due to missing or redundant bonds. Their high density creates band defects within the bandgap of the a-Si:H material. Deviations in bond angles and distances create tailored states of the valence and conduction band. A sketch of the classification of energy states is shown in Figure 2.9.

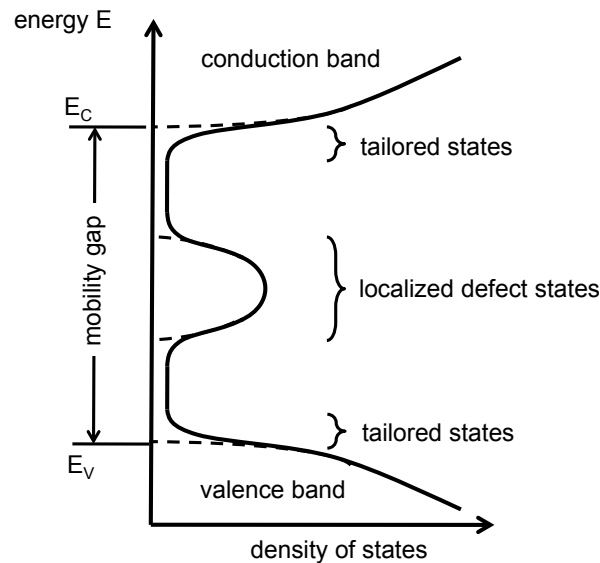


Figure 2.9: Classification of energy states into non-localized and localized band states in amorphous silicon. The mobility gap is labeled [60].

The mobility of charge carriers that occupy the tailored states of the valence and conduction bands is reduced, but increases significantly towards the bands. This is the reason one defines a mobility gap rather than a bandgap for a-Si:H. The mobility gap for a-Si:H is reported to be 1.65 eV [60]. That energy is required for electron excitation in order to overcome the mobility gap, so that a significant increase of layer conductivity becomes measurable. Unlike crystalline silicon, a-Si:H is a direct semiconductor [55, 60]. This leads to stronger absorption, which will be discussed for Figure 2.11 in the following section.

2.2.3 Microcrystalline Silicon

Microcrystalline silicon ($\mu\text{c-Si:H}$) is known to be a crystalline silicon material which is embedded in a matrix of a-Si:H [61]. The material quality is of major importance for the application in a $\mu\text{c-Si:H}$ solar cell. In Figure 2.10 the microstructure of $\mu\text{c-Si:H}$ is sketched for different deposition regimes. Typically, the growth of the crystalline material occurs due to the presence of nuclei next to the substrate surface. Their presence and survival depend on the deposition conditions. After the survival of numerous nuclei they increase quickly in size before the growth of the crystallites becomes columnar. The space in between the crystallites is associated with voids or is filled with a-Si:H. Unlike for the amorphous deposition regime, for the microcrystalline deposition regime, the precursor silane is strongly diluted with hydrogen. With reference to the total mass flow rate of precursors, the dilution usually lies in the range between 6 and 7%. This range of dilution is reported to be suitable for solar cell fabrication, but depends on other deposition parameters, such as on the electrical power the plasma is loaded with [10, 51, 62]. For higher dilutions ($< 6\%$) the crystallites are larger in size. This is illustrated by the left side of Figure 2.10. Here, the $\mu\text{c-Si:H}$ material is more porous and more sensitive to contamination, especially at the grain boundaries. Solar cells prepared with that kind of material possess low efficiencies [63].

When a lower dilution of silane ($> 7\%$) is used, the material properties become amorphous. Such material is illustrated on the right side of Figure 2.10. Note that due to the addition of hydrogen the quality of the amorphous material can be improved. One assumes the hydrogen quenches non-quenched silicon bonds [55].

Optically, $\mu\text{c-Si:H}$ possesses properties similar to crystalline silicon. As well as crystalline silicon, $\mu\text{c-Si:H}$ is an indirect semiconductor and has a bandgap of 1.12 eV . The absorption coefficient for photons with energies above 1.12 eV is usually smaller in comparison to a direct semiconductor [10]. A comparison of the absorption coefficients of amorphous, microcrystalline and crystalline silicon is shown in Figure 2.11. One can see the absorption coefficient of a-Si:H for photon energies above 1.65 eV is one order of magnitude larger than the one for the crystalline material. The absorption coefficient of $\mu\text{c-Si:H}$ material lies in between. Note that the $\mu\text{c-Si:H}$ material is embedded

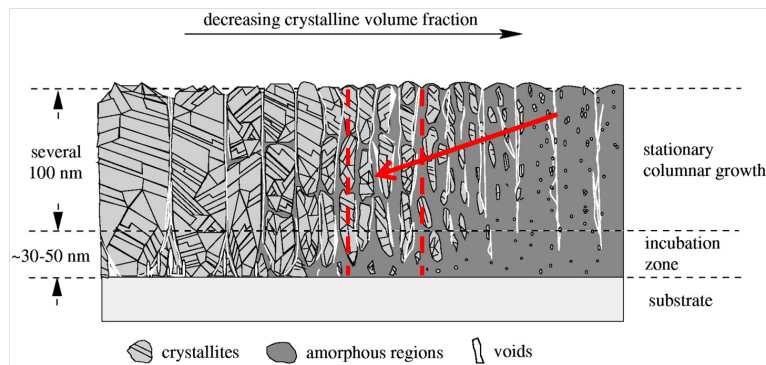


Figure 2.10: Illustration of the microstructural characteristics of $\mu\text{c-Si:H}$ [64]. The marked range indicates the material suitable for solar cell application.

in an a-Si:H matrix, which might explain the higher absorption compared to the pure crystalline material. Between 1.12 and 1.65 eV the absorption coefficient of the $\mu\text{c-Si:H}$ material is dominated by its crystalline volume fraction. Here, the $\mu\text{c-Si:H}$ is similar to the one of the pure crystalline material. Below 1.12 eV defect absorption determines the absorption of the $\mu\text{c-Si:H}$ material.

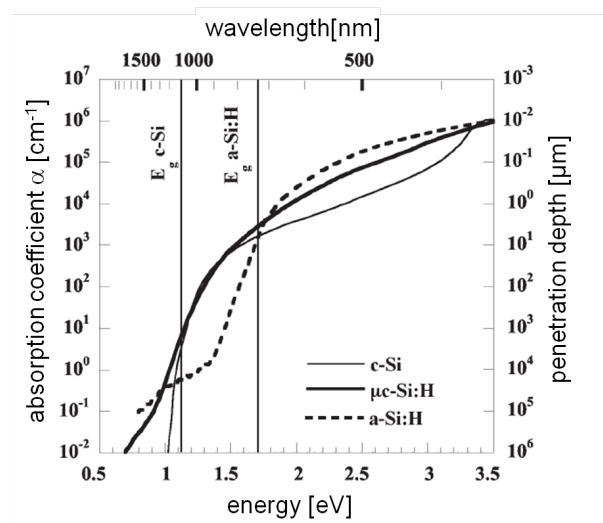


Figure 2.11: Comparison of absorption coefficients for amorphous, microcrystalline and crystalline silicon material as a function of photon energy and wavelength [10].

2.3 Micromorph Solar Cells and Modules

In the following a brief introduction into the concept of a micromorph solar cell will be given. Furthermore, the working principle of a solar cell and its characterizing parameters derived from current-voltage measurements will be discussed. Finally, the fabrication of a micromorph module is briefly summarized. For a more detailed discussion the reader is referred to the literature and references therein [60, 65, 66].

2.3.1 Concept of a micromorph solar cell

The concept of a micromorph solar cell combines an a-Si:H top with a $\mu\text{c-Si:H}$ bottom cell in tandem configuration. Due to the deposition sequence, the top and bottom cells are electrically interconnected in series. The a-Si:H absorber has a bandgap (mobility-gap) of 1.65 eV , whereas the $\mu\text{c-Si:H}$ absorber has a bandgap of 1.12 eV . Photons with energies higher than 1.12 eV but lower 1.65 eV are absorbed by the $\mu\text{c-Si:H}$ bottom cell. Photons with energies higher than 1.65 eV are absorbed by the a-Si:H top cell. This concept allows achieving stabilized cell efficiencies between 10 and 12% [63]. An actual stabilized record efficiency for micromorph solar cells is reported to be 12.3% (Nov. 2012) [67].

In Figure 2.12 the layer configuration of a micromorph tandem solar cell is shown. Both, the a-Si:H top cell and the $\mu\text{c-Si:H}$ bottom cell feature a p-i-n structure, which will be discussed in Section 2.3.2 in more detail. ZnO, which has high transparency and conductivity, is used for the front and back electrodes. Sufficient conductivity is required in order to realize a minimum of ohmic losses, since the generated photocurrent is passed through the ZnO. Furthermore, a very important feature of the ZnO is its as-grown rough surface morphology. Due to the rough interface, the incoming light is scattered and the light trapping within the absorber layer of the top and bottom cells is enhanced. As a result the photocurrent, and thus the efficiency of the solar cell device, is increased.

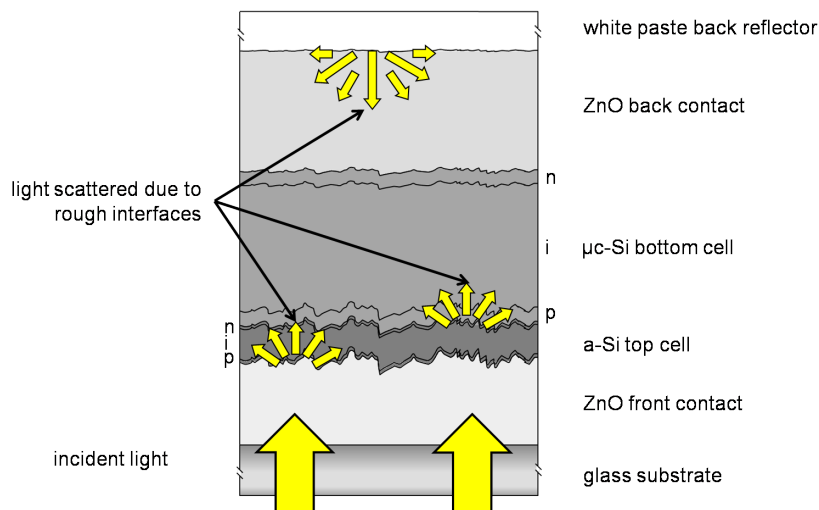


Figure 2.12: Layer configuration of a micromorph solar cell. Rough interfaces improve photocurrent generation due to light scattering.

The micromorph solar cell is completed with a reflector on its backside. In our case the reflector is realized with a white paste, containing mainly titanium dioxide and solvents. The reflector is utilized to reflect the light, which is transmitted through top and bottom cells on its first pass. Thus, the probability of light absorption in the absorber layers is enhanced. Furthermore, when a reflector is applied the thickness of the absorber layers can be reduced. This is important for the industrial fabrication

of solar cells and modules, since the deposition time of the absorber material can be reduced and thus the throughput can be increased.

2.3.2 Working principles of a solar cell and characteristic I(V) parameters

A crystalline silicon solar cell possesses a p-n-structure, like an ordinary diode. According to the type of cell the p- or n-doped silicon material acts as the absorber of the solar cell. The diffusion process of electron-hole pairs, generated within the absorber by the absorption of photons, determines the current-voltage characteristic for this type of solar cells. In order to get the generated pairs of electrons and holes to contribute to the photocurrent, they have to diffuse within the absorber towards the p-n junction. Here, the electron-hole pairs must be separated by the internal electric field of the p-n junction, before their recombination. After separation and under the conditions of open-circuit an external cell voltage can be measured. A large diffusion length of the charge carriers is essential for a good cell performance, since electron-hole pairs are typically generated far from the p-n junction. Whereas the diffusion length in the crystalline silicon material is above $200\ \mu\text{m}$, for a-Si:H material the diffusion length is in the order of $0.1\ \mu\text{m}$ [10]. For thin-film photovoltaic applications such low diffusion lengths prohibit the use of a cell structure with an ordinary p-n junction.

To circumvent the issue with the low diffusion length, a p-i-n cell structure is used. The "i" refers to intrinsic, non-doped material, which is implemented between the p- and n-doped layers of the solar cell (see Figure 2.12). It serves as the absorber material. Due to the cell structure, the electric field, necessary for charge separation, is created over the intrinsic absorber material. The electron-hole pairs are separated immediately after their generation due to photon absorption. Cells with p-i-n structure are controlled by drift processes instead diffusion processes. To illustrate the conditions of valence and conduction band in the p-i-n-structure, the band diagram is shown in Figure 2.13. The band diagram is sketched for short-circuit conditions (front and back electrode of the solar cell are shorted). The Fermi levels of n- and p-doped material lie on the same potential. An external device voltage of zero is measured. In the following, the case of no illumination is discussed first.

Due to the doping profile a current of charge carriers, driven by the concentration gradient of electrons and holes, from the n- and p-type material into the intrinsic absorber material is present. At the same time, localized positively charged defects in the n-type and negatively charged defects in the p-type material are left back. Their presence creates the electric field across the intrinsic absorber material. The electric field creates a drift-current of electrons and holes directed in the reverse direction of the diffusion-current. Once thermal equilibrium is reached, the electric field is fully developed and the drift- and the diffusion-currents annihilate each other.

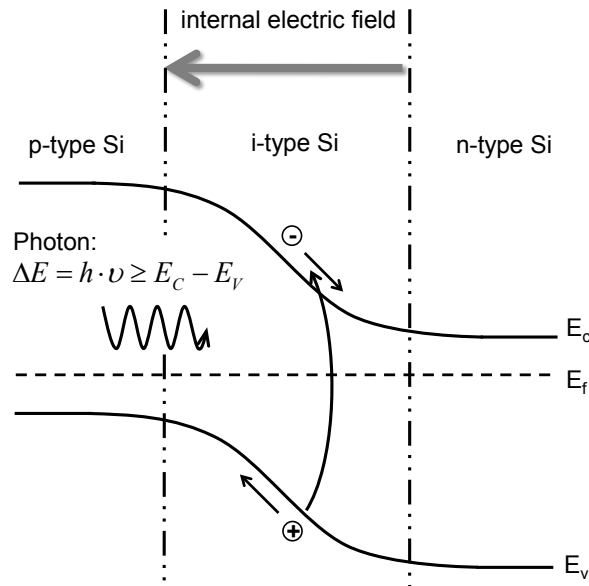


Figure 2.13: Sketch of a band diagram of a solar cell with p-i-n structure under short-circuit conditions (according to Ref. [60]).

When a photon is absorbed in the intrinsic absorber material, the generated electron-hole pair is separated due to the presence of the electric field. As a result, neglecting loss mechanisms such as recombination within the intrinsic absorber material, a measurable external short-circuit current can be interpreted in terms of photocurrent. Normalized to the cell area, one yields the short-circuit current or photocurrent density.

In the case of open-circuit conditions, the front and back electrodes of the solar cell are disconnected. Generated pairs of electrons and hole are still separated but they accumulate in the p- and n-type material of the solar cell. Due to the charge accumulation the Fermi levels of front and back electrodes are shifted with respect to one other until the band bending within the intrinsic absorber material is compensated. As a result an external device voltage can be measured.

In order to describe the current-voltage ($I(V)$) characteristic and to introduce important characteristic parameters, only a simple description of the $I(V)$ -characteristic of a single-junction solar cell is introduced here. The application of the description is strongly limited, since recombination mechanisms and a voltage-dependent photocurrent generation for solar cells with p-i-n structure are neglected. For a more detailed discussion, especially for solar cells with p-i-n structure, see Ref. [68] and references therein. A solar cell is a rectifying electric device. In addition to the dark-current the photocurrent characteristic of a diode is present. The dark current, characteristic depends on the type of diode. A simplified expression for the total current density of a solar cell can be given by [69] p. 719 et ff.:

$$j_{total} = j_{ph} - j_d, \quad (2.13)$$

where j_{total} , j_{ph} and j_d are the total current, photocurrent and dark-current density,

respectively, where

$$j_d = j_0 \cdot \left(\exp \left(\frac{eV}{nk_B T} \right) - 1 \right). \quad (2.14)$$

Here, j_0 , n , k_B , T , e and V are the saturation-current density, diode quality factor, Boltzmann constant, temperature, elementary electron charge and applied voltage, respectively. In general, the photocurrent density depends on the amount of absorbed photons. Assuming short-circuit (sc) conditions ($V=0$) j_d is zero and j_{total} is equal to the short-circuit current density (j_{sc}) and thus equal to j_{ph} :

$$j_{total} = j_{ph} = j_{sc}. \quad (2.15)$$

In open-circuit (oc) conditions, $j_{total} = 0$. Equation 2.13 in combination with Equation 2.14 can be rewritten as:

$$0 = j_{ph} - j_0 \cdot \left(\exp \left(\frac{eV_{oc}}{nk_B T} \right) - 1 \right). \quad (2.16)$$

Furthermore, the last equation can be solved for the open-circuit voltage (V_{oc}). As one can see from equation 2.17, V_{oc} is a function of photocurrent and saturation-current density.

$$V_{oc} = \frac{nk_B T}{e} \cdot \ln \left(\frac{j_{ph}}{j_0} + 1 \right). \quad (2.17)$$

The higher the j_{ph} – or the lower j_0 – the higher the V_{oc} . Among other dependencies, j_0 scales with the bandgap of the absorber material. It generally applies that the larger the bandgap of the absorber material the higher the V_{oc} [69] p. 723. The temperature dependence of a solar cell is not obvious from Equation 2.17, since the parameters j_{ph} and j_0 in general are a function of temperature, as well. As a rule of thumb for crystalline silicon solar cells it is [70] p. 231 ff.:

$$\frac{dV_{oc}}{dT} = \frac{1}{T} \left(V_{oc} - \frac{E_g}{e} \right), \quad (2.18)$$

where E_g is the bandgap of the absorber material. Usually $dV_{oc}/dT < 0$ is observed. The higher the temperature, the lower V_{oc} .

In Figure 2.14 the current-voltage characteristic of a solar cell is shown for the dark case and the illuminated case. The power output density of a solar cell depends on the voltage the solar cell is working at. It is

$$p(V) = j_{total}(V) \cdot V. \quad (2.19)$$

For $j_{total} = 0$ (external resistor is equal to infinity) and $V = 0$ (external resistor is equal to zero) the power output of the solar cell is zero. Its maximum power point is

reached for the point of maximum curvature at (V_{mpp}, j_{mpp}) . The efficiency (η) of a solar cell is defined by ratio of its maximum power output (p_{mpp}) over the power of the light (p_{ill}) the solar cell is illuminated with:

$$\eta = \frac{p_{mpp}}{p_{ill}}. \quad (2.20)$$

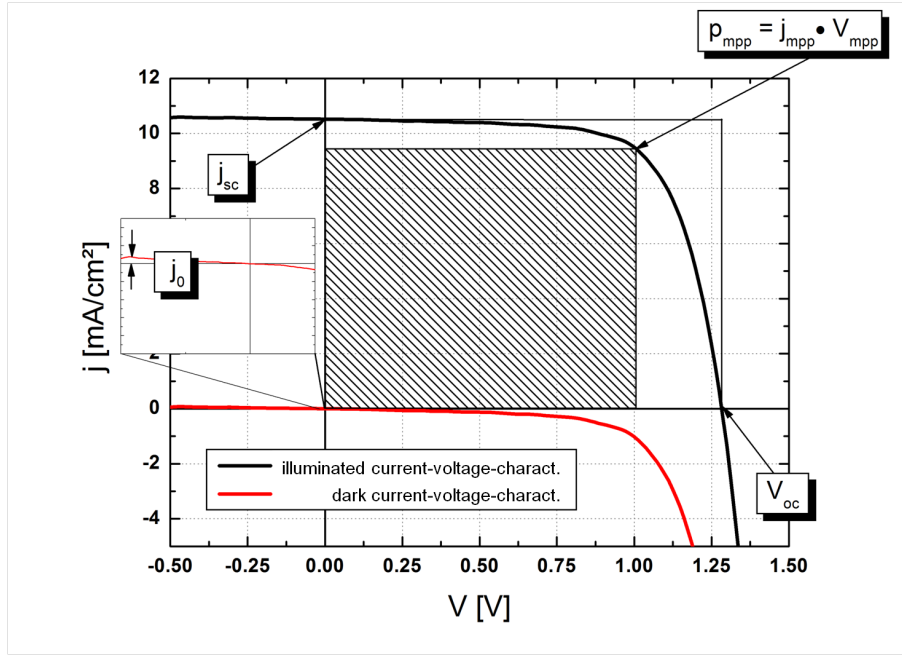


Figure 2.14: Current-voltage characteristic of a solar cell, showing important electric parameters.

A correlation between j_{mpp} , V_{mpp} , j_{sc} and V_{oc} is given by the fill factor (FF):

$$FF = \frac{p_{mpp}}{j_{sc} \cdot V_{oc}} = \frac{j_{mpp} \cdot V_{mpp}}{j_{sc} \cdot V_{oc}}. \quad (2.21)$$

Independent of the operation principle of a solar cell the current-voltage characteristic is affected by a series (R_{oc}) and a parallel (R_{sc}) resistance. In Figure 2.15, the electric equivalent circuit of a single-junction solar cell is shown. Considering R_{oc} and R_{sc} , Equation 2.13 in combination with Equation 2.14 can be rewritten

$$j_{total}(V_{total}) = j_{ph} - j_0 \cdot \left(\exp \left(\frac{e(V_{total} + j_{total}(V_{total}) \cdot R_{oc})}{nk_B T} \right) - 1 \right) + S, \quad (2.22)$$

where:

$$S = - \frac{V_{total} + j_{total}(V_{total}) \cdot R_{oc}}{R_{sc}}. \quad (2.23)$$

From the current-voltage characteristic shown in Figure 2.14 R_{oc} and R_{sc} can be derived as follows:

$$R_{oc} \approx 1 / \left(\frac{\partial j_{total}(V_{total})}{\partial V_{total}} \right)_{(V_{total}=V_{oc})} \quad (2.24)$$

$$R_{sc} \approx 1 / \left(\frac{\partial j_{total}(V_{total})}{\partial V_{total}} \right)_{(V_{total}=0)} \quad (2.25)$$

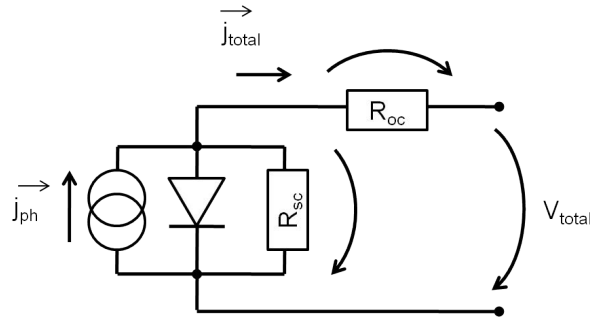


Figure 2.15: Electric equivalent circuit of a single-junction solar cell.

2.3.3 Module Fabrication

Large size substrates ($1.1 \times 1.3 m^2$) are used for the fabrication of thin-film silicon solar modules. These substrates are made of conventional soda-line glass. They possess a low content of iron and have a thickness of $3.2 mm$. The lower iron content leads to an increased transmission in the infrared spectral range around $1050 nm$ [71, 72]. Using such substrates has a beneficial effect on the spectral response of the photovoltaic active layers. To fabricate modules with a certain current-voltage characteristic, the monolithic interconnection of individual cells is required. The interconnection of cells is achieved by different laser scribing processes between certain deposition processes. In Figure 2.16 the module fabrication process regarding the monolithic interconnection of cells is illustrated. After the glass substrate enters the automated production line, the glass gets cleaned in a bath of an alkaline solution. The cleaning process is enhanced by an ultrasonic treatment at an elevated temperature. The substrate is then rinsed with deionized water and dried with a clean air flow.

Next follows the deposition of the LPCVD ZnO:B front electrode follows according to the process and deposition tool introduced in Section 2.1.1.2. After the front electrode is deposited, the first laser scribing process (P1) is executed. Here, a laser beam with a wavelength of $355 nm$ is used to ablate the ZnO:B from the substrate. The final pattern is of laser-scribed lines distributed equidistant across the total substrate area, separating bar-shaped areas of ZnO:B.

Next, the tandem cell structure, as introduced in Section 2.3.1, is deposited using the PECVD process, described in section 2.2.1. After the deposition of a-Si:H top cell and μc -Si:H bottom cell, the second laser scribing process (P2) is executed. Here, a laser with a wavelength of $532 nm$ is used. The laser beam is focused on the silicon

material through the glass and ZnO:B next to the P1 scribe. Glass and ZnO:B are transparent to the used laser wavelength. As a result only the silicon is ablated.

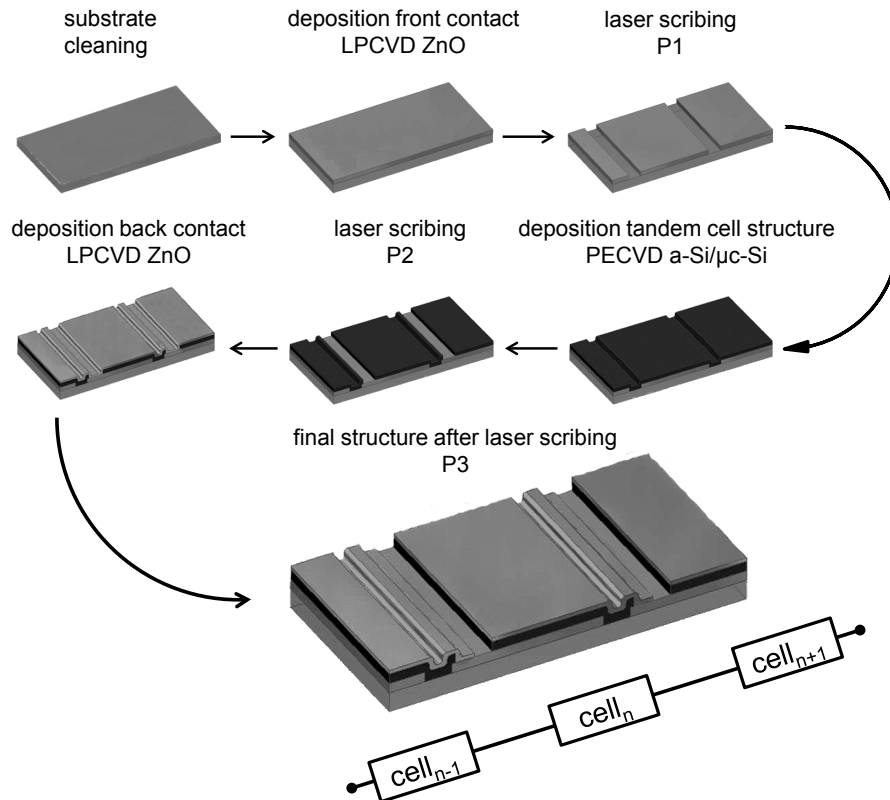


Figure 2.16: Illustration of the process to produce a monolithic interconnection of single solar cells on the substrate.

In a next fabrication step, the LPCVD ZnO:B back electrode is deposited on the laser-scribed (P1, P2) tandem cell structure. The final laser-scribing process (P3) completes the monolithic interconnection of individual cells fabricated on the glass substrate. For the P3 process, the same laser used for the P2-process is focused on the silicon material through the glass and the ZnO:B front electrode next to the P2 laser-scribe. As indicated in Figure 2.16 the cells are now interconnected in series. The gap between P1 and P3 is a non-photoactive module area (area loss). This gap has to be minimized in order to maximize the photoactive module area. Depending on the positioning accuracy of the used scribing system, typical gap distances are between 150 and 250 μm . The photoactive cell area is determined by the cell width, the distance between $P3_{n-1}$ and $P1_n$. Due to the limited substrate area, the number of cells and therefore the open-circuit voltage of the module decreases with increasing cell width. In turn the short-circuit current of the module is enhanced, which usually coincides with an increase of ohmic power-losses (I^2R) due to the contributions of front and back electrodes to the series resistance. A balance has to be found between area losses (gap between P1 and P3) and ohmic losses [11] p. 373.

In order to complete the internal electric circuit of the module, electric leads are glued onto the outer cells of the monolithically interconnected cell string. Cross con-

nectors are used to connect the glued leads with the junction box. The junction box is placed on the back glass sheet of the module. The front and back glass sheets are laminated together using a polymer sheet (polyvinyl butyral, PVB). Figure 2.17 illustrates the final module setup.

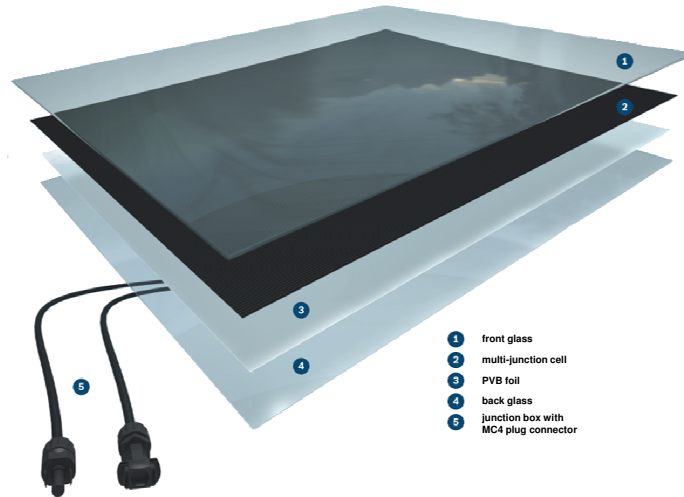


Figure 2.17: Thin-film silicon solar module as it is fabricated and used in the present work.

Chapter 3

Techniques of Characterization

In the present chapter several characterization techniques are briefly introduced. In Section 3.1 the optical techniques such as transmittance and reflectance measurements in the ultraviolet-visible and infrared spectral ranges are presented. The electrical and structural characterization techniques of solids and thin layers are briefly discussed in Sections 3.2 and 3.3. Finally, relevant electrical characterization techniques of complete solar cell and module devices are introduced in Section 3.4.

3.1 Optical Characterization

3.1.1 Ultraviolet-Visible Spectroscopy

For spectroscopic measurements, ranging from the ultraviolet to the near-infrared spectral region, dual-beam spectrometer "Lambda 950" from Perkin Elmer was used. This device measures transmittance and reflectance in the spectral range between 300 and 2500 nm. It features a grating monochromator and an integrating sphere (Ulbricht sphere), which is made of barium sulfate ($BaSO_4$). The integrating sphere is used to integrate the signal of a diffuse light source. Figure 3.1 illustrates the principal setup. In our case the diffuse light source was a glass sample covered with LPCVD ZnO:B.

Due to the rough surface morphology of the LPCVD ZnO:B, the light of the sample beam is scattered into the integrating sphere. As indicated in Figure 3.1a, the light is reflected at the inner of the sphere. As a result, the total transmission (TT) of the sample is measured. In order to evaluate the scattering capability of the LPCVD ZnO:B, the integrating sphere, as indicated in Figure 3.1b, is opened across from the sample position. Whereas the diffuse light (DT) is still integrated, the specular transmitted light exits the sphere and will not contribute to the signal measured. The light-scattering capability of the as-grown rough LPCVD ZnO:B is evaluated by the haze value (H). It is:

$$H = \frac{DT}{TT}. \quad (3.1)$$

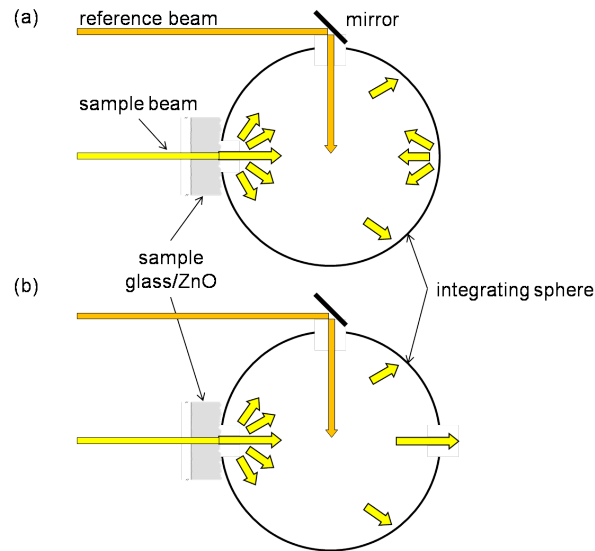


Figure 3.1: Principle setup of an integrating sphere for (a) total transmission (TT) and (b) diffuse transmission (DT) measurements.

Usually H is a function of wavelength with increasing values towards shorter wavelength. In the present work the H values at 600 nm will be used for the evaluation of light-scattering capability of fabricated LPCVD ZnO:B samples.

3.1.2 Fourier Transform Infrared Spectroscopy

Fourier transform infrared (FTIR) spectroscopy was used to determine the reflectance of the ZnO:B-covered glass samples in the spectral range between 1.2 and 25 μm . The measurement system used was a VERTEX80V from Bruker. The system is equipped with a specular reflectance accessory from Pike (VeeMAX). The major component of an FTIR spectrometer is a Michelson interferometer, see Figure 3.2.

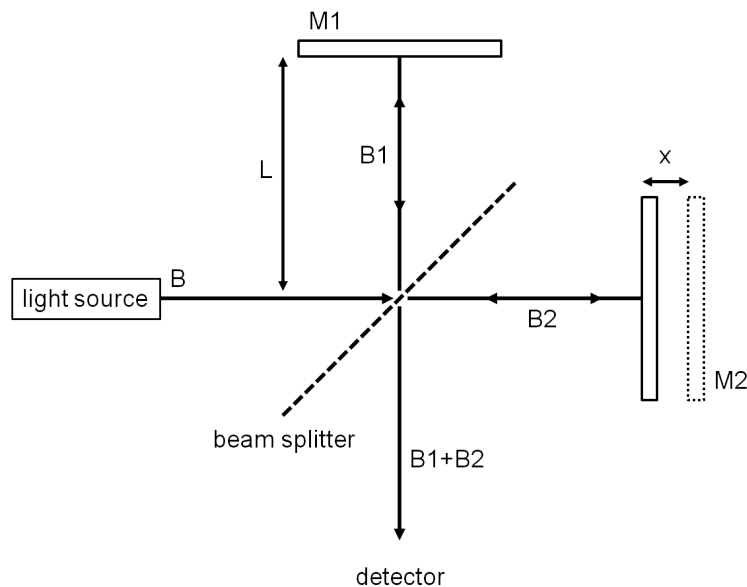


Figure 3.2: Schematic of a Michelson interferometer.

Here, the beam (B) of a light source is split into two beams (B1 and B2) by a semitransparent mirror, arranged at a 45° angle to the incident light beam. After the beams are split, the individual beams, B1 and B2, are reflected by the mirrors M1 and M2, respectively. Beams B1 and B2 are unified again after they traveled a distance of $2L$ (assuming x to be zero). Note, that the position of the mirror M2 can be adjusted by the value of x . When x is nonzero, the difference in the optical path length of beam B1 and B2 is $2x$. At the detector the signal measured is a superposition of B1 and B2. In the case of a monochromatic light source, constructive and destructive interference patterns can be observed when $2x$ is equal to $n\lambda$ and $(2n+1)\lambda/2$ ($n=0,1,2,\dots$), respectively. The signal intensity at the detector can be expressed as [73]:

$$I(2x) = S(\nu) \cos(2\pi\nu 2x), \quad (3.2)$$

where $S(\nu)$ is the intensity of the monochromatic light beam of the frequency ν . ν is correlated to its wavelength (λ) by $\nu = c/\lambda$. c is assigned to the speed of light. In the case of a polychromatic light beam, the interference pattern is given by:

$$I(2x) = \int_0^{\infty} S(\nu) \cos(2\pi\nu 2x) d\nu. \quad (3.3)$$

Here, $S(\nu)$ is the spectral power density of the light source. $S(\nu)$ as a function of ν comprises information about the intensity of the light in a spectral interval $d\nu$ at the frequency ν . The spectral power density can be calculated from $I(2x)$ by Fourier transformation:

$$S(\nu) = \int_{-\infty}^{\infty} I(2x) \cos(2\pi\nu 2x) 2dx. \quad (3.4)$$

For a more detailed description of the mode of operation the reader is referred to the Ref. [73]. In order to generate reflectance data for a sample to be investigated, the light beam (B1+B2) has to interact by reflection with the sample before detection. The radiation management is realized by the reflection accessory from Pike, mentioned above. The reflectance (R_{sample}) of the sample is given by the following relation:

$$R(\nu)_{sample} = \frac{S(\nu)_{sample}}{S(\nu)_{reference}} k(\nu)_{reference}. \quad (3.5)$$

This relation is applied in order to eliminate the non-quantified spectral intensity distribution of the light source. $k(\nu)_{reference}$ depends on the real reflectance of the reference sample ($R_{reference}$) and differs from unity ($k \geq 1$) when the reflectance of the reference sample is less than 1. For reflectance measurements in the infrared spectral range, as mentioned above, metallic mirrors are used as the reference sample. Due to the high concentration of free electrons, the reflectance in the infrared spectral range

is close to unity. In the present work a gold mirror was used as the reference sample. Here, the reflectance above 1200 nm exceeds 0.99 [74].

3.1.3 Raman Spectroscopy

Raman results shown in the present work were acquired with a "LabRAM ARAMIS" spectrometer from Horiba. Raman spectroscopy is based on inelastic light scattering. The incoming light interacts with elementary excitations of the probed medium. These are for example phonon excitations. Depending on the emission or absorption of phonons, the scattered light shifts to lower (Stokes-shift) or higher (Anti-Stokes-shift) frequency values, respectively. In the present work a laser with a wavelength of 473 nm was used as the excitation source. For more details on the effect of Raman light scattering the reader is referred to Refs. [73, 75].

3.2 Electrical Characterization

3.2.1 Four-Point Probe Resistance Measurement

In the present work a four-point probe measurement was used to determine the sheet resistance and the resistivity of ZnO:B deposited on glass substrates. A schematic of the of the experimental setup is shown in Figure 3.3. A current (I) is introduced between the probes S1 and S2. As a result a voltage drop (V) between S3 and S4 can be measured. The resistivity then is given by

$$\rho = \frac{\pi}{\ln(2)} t \frac{V}{I} = 4.532t \frac{V}{I}, \quad (3.6)$$

where t is the film thickness. The sheet resistance is defined as $R_{sh} = \rho/t$. For a more detailed discussion of the measurement the reader is referred to Ref. [76].

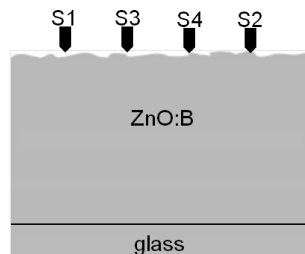


Figure 3.3: Schematic of collinear probe arrangement for the four-point probe measurement to determine sheet resistance or film resistivity.

3.2.2 Hall Effect Measurement

Information about charge carrier concentration and mobility can be deduced from Hall effect measurements, which utilize the effect of the deflection of charge carriers which

are moving with a velocity (\vec{v}) in a magnetic field (\vec{B}). An idealized schematic experimental setup is shown in Figure 3.4. The force that is responsible for the deflection, is known as the Lorentz force ($\vec{F}_L = q(\vec{v} \times \vec{B})$), where q is assigned to the charge to be deflected. As a result of deflection an electric field is generated. The electric field is directed in the reverse direction of the deflection current. In the stationary case it is

$$0 = q(E_y + v_x \cdot B_z), \quad (3.7)$$

where the subscript indicates the vector component. The current in x direction, which is deflected by the Lorentz force, can be expressed as

$$I = qn\rho \cdot wt \cdot v_x, \quad (3.8)$$

where n is assigned to the charge carrier density and ρ to the resistivity. V is the voltage driving the current in x direction. w and t are the dimensions width and thickness of the idealized conductor. It is

$$V = \frac{\rho \cdot l}{wt} I. \quad (3.9)$$

Combining Equation 3.7 and 3.8 one obtains

$$E_y = v_x \cdot B_z = \frac{B_z I}{qn \cdot t} \quad (3.10)$$

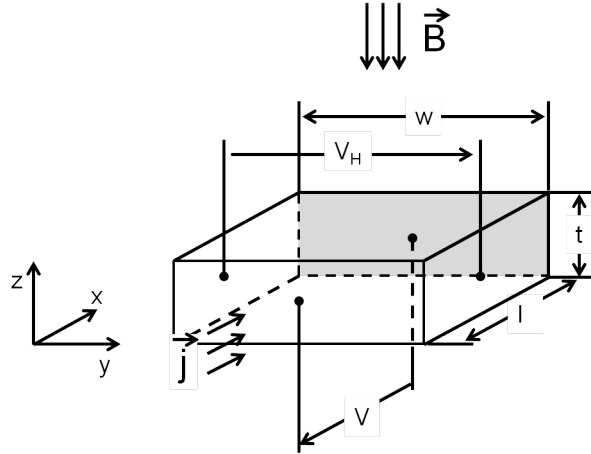


Figure 3.4: Schematic of Hall effect. A lead of the dimension length (l), width (w) and thickness (t). \vec{j} is the current density, which is driven by the voltage V . \vec{B} indicates the magnetic field. V_H is assigned to the Hall voltage, which is caused by the deflection of \vec{j} within the field \vec{B} .

The Hall voltage then is given by

$$\int_0^{V_H} dV_H = V_H = \int_0^w E_y dy = \frac{BI}{qn \cdot t} \quad (3.11)$$

By rewriting Equation 3.11 the Hall coefficient (R_H) is defined as

$$R_H = \frac{1}{qn} = \frac{V_H t}{BI}. \quad (3.12)$$

From Equation 3.12 charge carrier density (n_H) and mobility (μ_H) can be derived from the following relations

$$n_H = \frac{1}{qR_H}, \quad \mu_H = \frac{R_H}{\rho} \quad (3.13)$$

A more detailed discussion of the Hall effect measurement is given in Ref. [76]. Note, that the above model to determine n_H and μ_H is valid for thin films possessing a homogeneous structure. Other more sophisticated models may also apply. For simplicity the above model is assumed to be valid in the first approximation.

3.3 Structural Characterization

3.3.1 Atomic Force Microscopy

Atomic force microscopy (AFM) was used to characterize the morphology of the top surface of the rough ZnO:B front electrode. AFM is a scanning probe technique. It is realized with a cantilever, which is equipped with sharp tip. The tip interacts with the atomic surface structure of the sample, yielding a height profile. In general the height profile can be obtained with two different modes of the measurement. The first mode is the contact mode. Here, the tip is in contact with the surface. While scanning, the deflection of the tip is adjusted to be constant. For the second, the non-contact mode, the tip oscillates with its natural frequency. When it nears the surface a phase shift in its oscillation can be observed. While scanning, the approach is adjusted in order to fix the observed phase shift. In the present work the non-contact mode was used for surface analysis. For more details the reader is referred to Refs. [76–78].

In the present work AFM images were acquired with a system from Nanotec Electronica. The images were $10 \times 10 \mu m^2$ and were further analyzed by determining the root mean square roughness (σ_{RMS}) as follows:

$$\sigma_{RMS} = \sqrt{\frac{1}{MN} \sum_{m=1}^M \sum_{n=1}^N (z(x_m, y_n) - \langle z \rangle)^2}, \quad (3.14)$$

where $z(x_m, y_n)$ is the measured height value at the position (x_m, y_n) and $\langle z \rangle$ is defined as the average deflection of the cantilever:

$$\langle z \rangle = \frac{1}{MN} \sum_{m=1}^M \sum_{n=1}^N z(x_m, y_n). \quad (3.15)$$

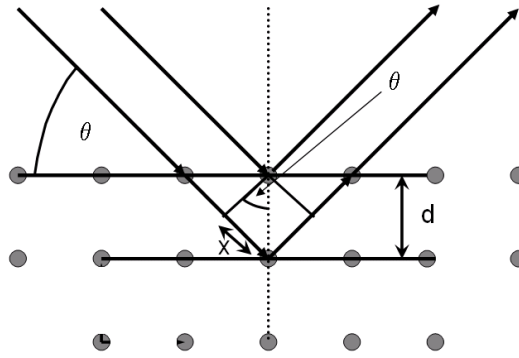


Figure 3.5: Schematic of x-ray diffraction geometry (Bragg-Brentano).

M and N are integer elements and determine the size of the analyzed surface array.

3.3.2 X-Ray Diffraction Analysis (XRD)

The diffraction of X-rays by solids is a method for analyzing their crystallographic structure. In the present work samples were investigated with a PANalytical X'Pert PRO MRD diffractometer using CuK_{α} radiation. The principle experimental setup is shown in Figure 3.5. An angular range of $20^{\circ} < 2\theta < 100^{\circ}$ has been investigated for structure analysis. X-rays are diffracted by net planes. The conditions of diffraction are described by Bragg's equation:

$$n\lambda = 2 \cdot d_{hkl} \cdot \sin(\Theta), \quad (3.16)$$

where n is assigned to the order of diffraction, λ to the wavelength of the X-ray used ($\lambda_{CuK_{\alpha}} = 1.5418 \text{ \AA}$), d_{hkl} to the net plane spacing and Θ to the angle between the net plane and the incident X-ray beam. The subscript hkl indicates Miller's indices (h, k, l). They indicate different net planes, depending on the crystal structure. For more details the reader is referred to Ref. [79].

3.3.3 Secondary Ion Mass Spectroscopy (SIMS)

Secondary ion mass spectroscopy (SIMS) was used for chemical composition analysis. The investigations were conducted at the Institute for Photovoltaics (IPV) in Stuttgart. During SIMS investigations a primary ion beam is directed at the sample surface. In the present work the ion beam was composed of positively charged cesium ions. While the sample surface is under bombardment of primary ions, secondary ions are ablated. The secondary ions are then detected by a mass spectrometer.

In the present case a time-of-flight mass spectrometer was used for chemical composition analysis. Here, the time of flight of the ablated secondary ions is analyzed. A pulsed beam of primary ions causes a pulsed beam of secondary ions, to come from the

sample surface. Due to an electric field the secondary ions are forced to accelerate into the direction of the detector. At the end of the acceleration process the ions possess the same kinetic energy. Ions with less weight will reach the detector within a shorter time than heavier ions. In this way the system is able to separate an ion's ratio of mass number to charge number. A more detailed discussion of this technique is given in Refs. [80–82].

3.4 Characterization of Solar Cells and Modules

3.4.1 Current-Voltage Characterization of Solar Cells and Modules

The current-voltage characteristic (I-V), as introduced in Section 2.3.2, of illuminated solar cells and modules can be derived from solar simulator measurements. One distinguishes between measurement system with continuous and flash light illumination. For both systems the goal is to replicate the solar light spectrum reaching the earth's surface. In the present work the continuous light system from Wacom (WXS-156S-L2,AM1.5GMM) was used in order to determine the I-V characteristic of solar cells and small modules (samples with a size of up to $10 \times 10 \text{ cm}^2$) [83]. Solar modules with a size of $1.3 \times 1.1 \text{ m}^2$ were characterized with a flash tester from Berger Lichttechnik GmbH & Co. KG.

The influence of the atmosphere on the extraterrestrial solar spectrum is characterized by molecular absorption bands. These are related to gaseous molecules such as water (H_2O) and carbon dioxide (CO_2). In Figure 3.6 the terrestrial solar light spectrum AM1.5 is compared with the light spectrum generated by the solar simulator system from Wacom. The characteristic absorption bands are indicated.

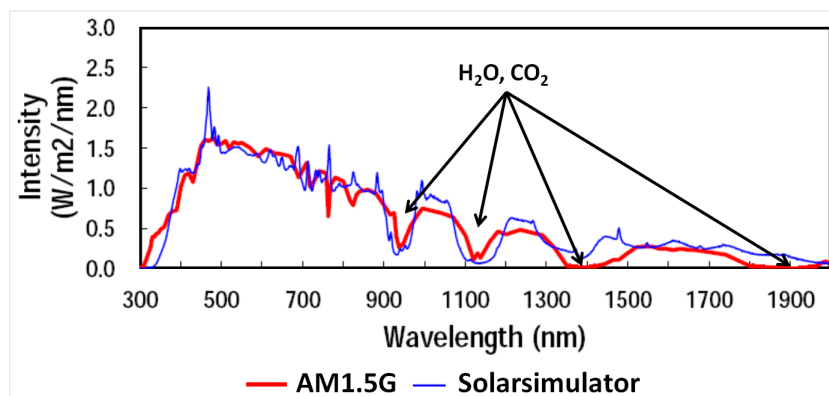


Figure 3.6: Comparison of light spectra. The terrestrial solar spectrum AM1.5 is compared with the spectrum generated by the continuous light system from Wacom [83]. Characteristic absorption bands of water and carbon dioxide are indicated.

In order to simulate the sunlight the system from Wacom uses a xenon high-pressure

lamp and a halogen lamp. With additional filters the spectra are further adjusted. In the term AM1.5, AM refers air mass, and 1.5 indicates the path length the extraterrestrial light passed through the atmosphere. Here, one atmosphere (AM1) scales with the height h where the pressure measured at the earth's surface (p_{norm}) decreased by $p_h = 1/e \cdot p_{norm}$ in accordance with the barometric formula [60]. As in the present work, solar cells and modules are generally rated with standardized test conditions. These conditions are given in detail in IEC60904. In general the ratings were done with a terrestrial solar radiation spectrum of AM1.5 at 1000 W/m^2 . The device temperature during measurement was set to 25°C .

3.4.2 External Quantum Efficiency (EQE)

The spectral response of a solar cell includes both optical information and information regarding charge carrier collection. The spectral response (S) of a solar cell is defined as ratio of the short-circuit current density ($j_{sc} [\text{A/m}^2]$) and the monochromatic irradiation power ($E [\text{W/m}^2]$). It is [60]:

$$S(\lambda) = \frac{j_{sc}(\lambda)}{E(\lambda)}, \quad (3.17)$$

where λ is assigned to the incident wavelength. If one normalizes the current density in Equation 3.17 to the electron charge (e) and the irradiation power to the energy of a single incident photon (hc/λ), one obtains the external quantum efficiency (EQE) [60]:

$$EQE(\lambda) = \frac{j_{sc}(\lambda)}{e} \cdot \frac{hc}{\lambda E(\lambda)} = \frac{hc}{e\lambda} S(\lambda), \quad (3.18)$$

where c is assigned to the speed of light and h to Planck's constant. One distinguishes between the external and internal quantum efficiency, because only a certain amount of photons penetrate the absorber material of the solar cell. Some of the photons are reflected at interfaces before they reach the absorber material. For the internal quantum efficiency (IQE) it is:

$$IQE(\lambda) = \frac{EQE(\lambda)}{1 - R(\lambda)}, \quad (3.19)$$

where R is assigned to the reflectance, the reflected part of the incoming photons.

Chapter 4

Ethanol-enriched LPCVD ZnO bilayers: Properties and Growth – A Potential Electrode for Thin Film Solar Cells

The present chapter investigates ethanol as additional precursor to water and diethylzinc in order to deposit ZnO by low pressure chemical vapor deposition. Here, the addition of ethanol is intended to modify the as grown surface morphology of the deposited ZnO film. The application of such layers to micromorph solar cells will be discussed. In Section 4.1 more introductive information will be given. After, experimental details are presented in Section 4.2. Section 4.3 is divided into two parts. In the first one, results of ZnO single layers deposited using a mixture of ethanol, water and diethylzinc are presented. In the second part the approach of ethanol enriched bilayers is discussed. Finally, in the Section 4.4 the main results of the chapter are summarized.

4.1 Background

Zinc oxide (ZnO) deposited by low-pressure chemical vapor deposition (LPCVD) is a widely used transparent conductive oxide (TCO) in thin-film photovoltaics and other applications like low-emission coatings and gas sensor devices. In photovoltaics ZnO:B layers are used as front and back electrodes to electrically contact thin-film solar cells. One of the advantages of LPCVD ZnO:B as a front electrode is that it possesses an as-grown roughness, unlike sputtered ZnO which needs an additional etching step to texture the surface [84]. Surface roughness is directly related to a film's light scattering properties. Indeed, efficient light scattering allows the use of thinner absorber layers in thin-film silicon solar cells without compromising photocurrent generation [57]. This in turn can be translated into reduced takt time and increased throughput. Also,

regarding cell stability, thinner absorber layers are preferred in thin-film silicon tandem cells, as light-induced degradation of hydrogenated amorphous silicon (a-Si:H) can be reduced [85]. For a given growth regime, the roughness of LPCVD ZnO:B is controlled primarily by adjusting the thickness of the layer: The thicker the layer, the rougher the ZnO surface tends to be. Therefore, the amount of light scattering can easily be tuned.

The present section discusses the use of LPCVD ZnO:B for front and back electrodes for micromorph silicon solar cells as introduced in Section 2.3.1. These devices combine an a-Si:H top cell with a hydrogenated microcrystalline silicon ($\mu\text{c-Si:H}$) bottom cell in a tandem configuration [10, 56]. It is well established that the quality of $\mu\text{c-Si:H}$ is sensitive to the morphology of the surface on which it is deposited [86], as well as to its crystallinity [87]. Therefore, one has to pay special attention to the quality of the front TCO surface, even the $\mu\text{c-Si:H}$ absorber is deposited on top of the a-Si:H absorber. Optimized as-grown LPCVD ZnO:B has very good electrical and optical properties that result from large grains [27]. However, the sharp pyramidal features of its surface are known to deteriorate the quality of subsequently deposited $\mu\text{c-Si:H}$ absorber layers, which are characterized by porous regions, also called cracks [88]. In fact, it has been shown that the crack density in the $\mu\text{c-Si:H}$ absorber material is directly related to the roughness and V-shaped features of the ZnO:B layer [86]. Usually, a high density of cracks is correlated with losses in fill factor and open-circuit voltage and, as a result, in conversion efficiency. High densities of cracks are avoided by using ZnO:B layers of reduced thickness and scattering ability (roughness). Another approach is to introduce optimized p- and n-type silicon oxide layers deposited before and after the $\mu\text{c-Si:H}$ absorber material [89]. To obtain a surface morphology suitable for both the deposition of high-quality $\mu\text{c-Si:H}$ and high-angle light scattering, an argon-based plasma treatment on as-grown LPCVD ZnO:B layers is typically used [90]. The aim of the treatment is to change the surface grooves from V-shaped to U-shaped. However, this approach is not cost-efficient for industrial production. Another possible approach to achieve good optical and electrical properties is to use sputtered ZnO, which features a U-shaped morphology after hydrochloric acid etching [84, 91]. However, this approach requires two different processes in order to create front electrodes suitable for thin-film silicon devices, and free carrier absorption is usually higher than in LPCVD ZnO:B films.

In the following a technique to modify the surface morphology of LPCVD ZnO:B without additional plasma treatment or etching is proposed. Ethanol is added to the water and diethylzinc mixture during deposition to change the surface morphology of the ZnO:B layer. In fact, it has already been reported that ethanol and other alcohols like methanol or butanol can be used as an oxygen source together with diethylzinc to deposit ZnO layers [18, 23, 92], and that they can prompt morphological changes. Here the results of Wenas et al, [92] will be confirmed. Furthermore, a growth mechanism

is proposed which is able to explain the observations in the regard of electrical, optical and morphological changes.

4.2 Experimental

ZnO layers were deposited on 0.5 mm thick AF45 glass substrates from SCHOTT, using the deposition tool introduced in Section 2.1.1.1. The films were grown with an LPCVD reactor at a pressure of 0.5 mbar and a substrate temperature of 175 °C, unless otherwise indicated. Diethylzinc (DEZ, $[C_2H_5]_2Zn$) and water (H_2O) were used as the main precursors to form the ZnO. Ethanol (C_2H_5OH) was added during ZnO deposition to change the film surface morphology.

Both, scanning electron microscopy (SEM) and atomic force microscopy (AFM) were used to analyse the surface roughness of the samples. The optical properties were investigated with a photospectrometer featuring an integrating sphere to measure the total and diffuse transmittance, from which haze was calculated. The haze value given is for a wavelength of 600 nm. FITR-reflectance measurements have been utilized to investigate samples properties in the infrared spectral range. Electrical properties were measured with a four-point probe to determine the sheet resistance and resistivity of the films. Film crystallography was investigated by X-ray diffraction (XRD) analysis in the $\theta - 2\theta$ mode.

4.3 Results

The following section is divided into two parts. The first part deals with single ZnO layers for which ethanol was used for the whole layer deposition, and we discuss the role of ethanol during deposition. The second part follows the work of Wenas et al. [92]. A standard layer deposited without ethanol is capped by a thin ZnO film deposited with a mixture of ethanol, water and DEZ.

4.3.1 ZnO single layers deposited using a mixture of ethanol, water and DEZ

Structural and electrical properties

Different agents can be used to oxidize DEZ in order to deposit ZnO [16, 18, 23, 93]. Grain growth, deposition rate, optical and electrical properties are expected to vary when different agents are used as precursors, as each oxidation agent is characterized by its respective kinetics. Figure 4.1 shows the ZnO growth rate as a function of ethanol mass flow rate. For the present investigations, the flow was varied between 0 and 20 sccm. The flow ratio of DEZ to water was kept constant at 2.5, and a value

of 50 *sccm* of DEZ was used. In every case the deposition time was adjusted to achieve films with thicknesses of about $2 \mu\text{m}$. As can be seen from Figure 4.1, the deposition rate decreases from approximately 25 to $15 \text{ \AA}/\text{s}$ as the ethanol flow rate increases. A possible explanation for this behaviour is a reduction of the adatom residence time induced by the rise of the total gas flow rate. Ethanol might also influence the formation of intermediates (Zn_xO_y) in the gas phase and on the sample surface. It is well known that these intermediates are important for cluster formation and thus for the deposition and growth of a ZnO film [12,94]. As will be discussed later, ethanol plays an important role, especially at the surface of ZnO.

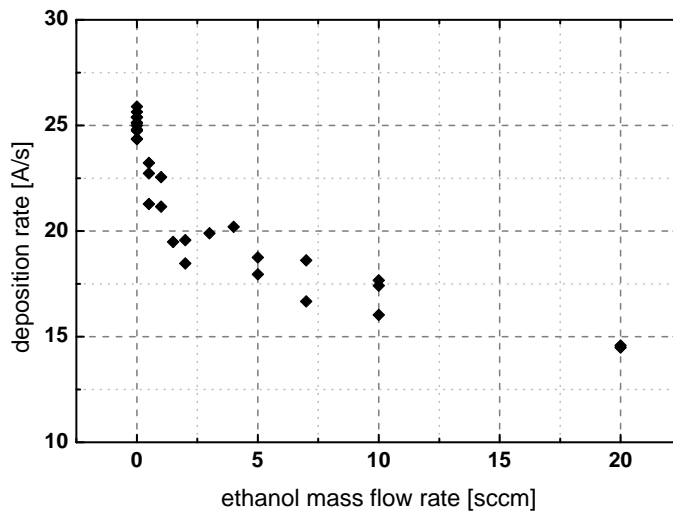


Figure 4.1: Deposition rate of LPCVD ZnO deposited at 175°C and 0.5 mbar as a function of ethanol mass flow rate.

In Figure 4.2a, a standard, ethanol-free ZnO film, $2 \mu\text{m}$ thick, is shown as a reference, with its typical pyramidal-like surface features. For the results shown in Figure 4.2b, c and d the ethanol flow rate was increased from 2 to 10 sccm . Figure 4.2 demonstrates the evolution of ZnO surface morphology with increasing ethanol flow rate. One observes that the surface features become smaller and the morphology becomes smoother with rising ethanol concentration. Furthermore, the occurrence of cracks can be observed for higher ethanol flow rates, as can be seen in Figure 4.2c and d.

In the ethanol-free case, the ZnO grows with a (110) preferential crystallographic orientation, corresponding to the a-axis of the wurtzite structure, as shown by XRD in Figure 4.3. Furthermore, Figure 4.3 shows XRD spectra of films grown with 0 to 10 sccm of ethanol. As expected ethanol has a major impact, not only on the morphology, but also on the preferential crystallographic orientation.

As seen in Figure 4.3b, an increase in the ethanol mass flow rate leads to a decrease in the (110) peak signal until it vanishes for the film deposited with 10 sccm . In contrast, the (100) peak intensity increases for films with up to 5 sccm . For higher mass flow rate, the (100) peak signal decreases again while the (101) slightly increases. Figure 4.3a shows a detail of the XRD spectra for 2θ from 30 to 40 degrees. The measured

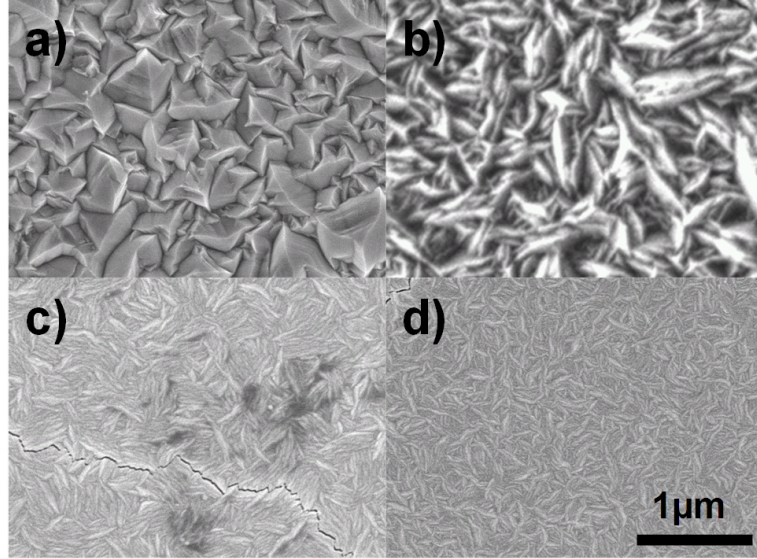


Figure 4.2: SEM images of $2\ \mu\text{m}$ thick ZnO films deposited a) without ethanol and with b) $2\ \text{sccm}$, c) $7\ \text{sccm}$, and d) $10\ \text{sccm}$ of ethanol during layer growth.

peaks are slightly shifted towards lower diffraction angles compared to unstrained ZnO powder, indicating residual stress in the deposited films. In Table 4.1, the distances between planes with (002) orientation - also known as the lattice constant, c - are shown for different ethanol flow rates.

Table 4.1: Separation of (002) planes for different ethanol flow rates.

conditions	2θ [$^\circ$]	c [nm]	Δc [nm]
ZnO powder	34.449	5.2013	
ZnO with 0 sccm ethanol	34.389	5.2101	0.0087
ZnO with 3 sccm ethanol	34.343	5.2169	0.0156
ZnO with 5 sccm ethanol	34.324	5.2197	0.0184
ZnO with 10 sccm ethanol	34.328	5.2192	0.0178

One can see from the calculated values that grains oriented normal (perpendicular) to the surface with their c -axes (002) are stretched along the c -axis. Furthermore, the higher the ethanol concentration, the more the films tend to be strained, as can be seen when comparing the c values of ZnO films deposited with and without ethanol. Here, the amplitude of elongation, Δc , is only on the order of one half of the maximum change observed for $5\ \text{sccm}$. For $10\ \text{sccm}$, c is reduced again, indicating a relaxation of the tensile strain along the c -axis, probably related to the occurrence of undesired cracks, as observed in Figure 4.2c and d, upper left corner.

The resistivity, which was deduced from the measured sheet resistance and the film thickness, is shown in Figure 4.4. An increase of about 5 orders of magnitude is observed between the minimum and maximum values. The resistivity increase is more pronounced for ethanol flow rates above $5\ \text{sccm}$. It is interesting to note that the onset

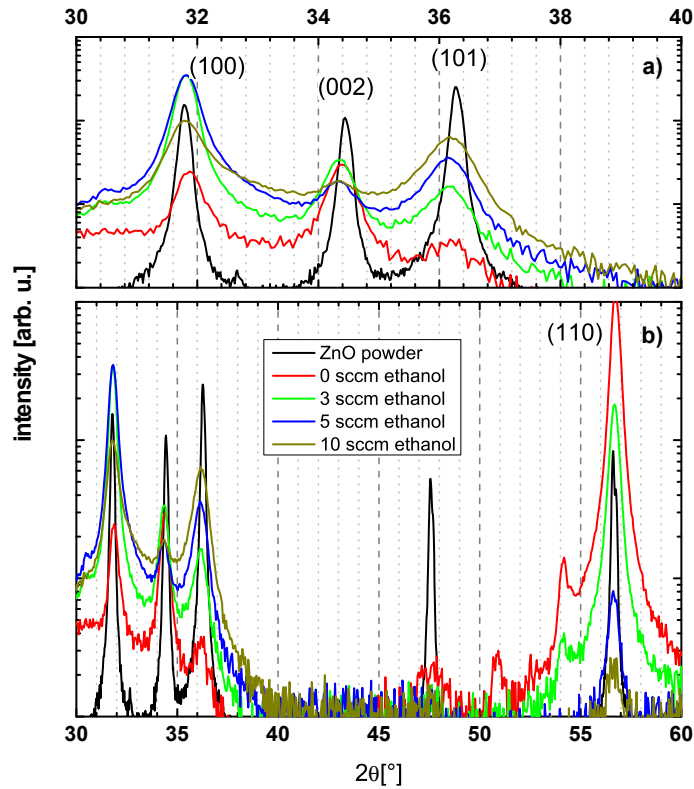


Figure 4.3: XRD data for $2\ \mu\text{m}$ thick ZnO films deposited with different ethanol flow rates.

of increased spread in resistivity above $5\ \text{sccm}$ coincides with film relaxation through cracks as explained before. We assert that the resistivity is influenced mainly by the formation of cracks in the regime of high ethanol mass flow rate, under our process conditions.

Catalytic growth model

In order to ascertain if a reaction between DEZ and ethanol occurs, layer deposition was attempted using those two precursors exclusively (i.e. without water). No notable layer deposition was observed for substrate temperatures of 175 and $250\ ^\circ\text{C}$, at $0.5\ \text{mbar}$ and a DEZ/ethanol ratio of 0.25 , using $5\ \text{sccm}$ of DEZ. Neither indications of dust formation within the reactor due to premature reactions were found. At $350\ ^\circ\text{C}$, a deposition rate of about $3\ \text{\AA}/\text{s}$ was observed. Although Oda et al. [18] used other deposition conditions (e.g. higher pressure, different mass flow rates and higher temperatures), they found a maximum growth rate at around $300\ ^\circ\text{C}$, using DEZ and ethanol as precursors. That indicates that rather high substrate temperatures are required to form ZnO films from this precursor mixture. In fact, sufficient activation energy has to be provided from the substrate surface in order to facilitate the reaction between DEZ and ethanol. These findings lead to the assumption that at low temperatures ($175\ ^\circ\text{C}$) and low pressures ($0.5\ \text{mbar}$) ethanol is not directly involved in the formation of ZnO. Therefore, it is supposed that the major reaction path remains between DEZ and water. Note, that

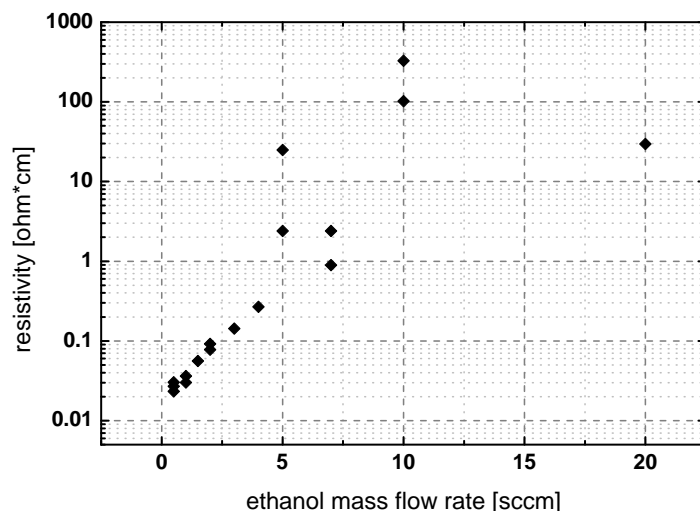


Figure 4.4: Resistivity of ZnO films versus ethanol flow rate during deposition.

this main reaction mechanism leading to the deposition of ZnO, from DEZ and water, is discussed in detail elsewhere [12–14, 94, 95].

To account for the effect of ethanol, the following mechanism is proposed: Ethanol is known to adsorb and decompose on ZnO surfaces [96,97]. Furthermore, it is established that the decomposition of ethanol depends on the ZnO crystallographic plane exposed to the ethanol vapor. The crystallographic planes on a polycrystalline ZnO film surface are linked to the crystallographic texture of the deposited film. It is proposed that, if the ethanol surface reaction is facilitated by a distinct grain direction, the growth rate of other crystallographic orientations might also be influenced, depending on the ethanol exposure. As a result, the growth competition between different grains characterized by different orientations might be altered by the presence of ethanol. This would then result in different surface morphologies. Such evolutionary grain growth was discussed by Nicolay et al. for LPCVD ZnO:B [16]. They stated that growth rate anisotropy of different crystal planes is significantly influenced by adatom surface mobility, which in turn depends on temperature, the precursors and other conditions. Note that it is not yet clear how ethanol, adsorbed on the ZnO surface, affects these conditions.

Kwak et al. [98] studied the adsorption and reaction of ethanol on the surface of ZnO nanowires. They proposed that ethanol is adsorbed on the surface and decomposes on oxygen vacancy sites into ethoxy and hydrogen. The oxygen of the ethoxy molecule is adsorbed on vacancy sites, and the hydrogen is adsorbed on oxygen at lattice sites at the ZnO surfaces.

No detailed growth mechanism for our deposition conditions is described in the literature. Therefore, it is proposed that the oxygen of ethanol is incorporated into the ZnO lattice at oxygen vacancy sites, as described above. This incorporation could explain both residual stress and the increase of sheet resistance.

Indeed, Pagni et al. stated that oxygen vacancies and other oxygen-induced defects

affect the tensile strain and the grain size of ZnO [99]. They deposited ZnO films on glass slides by metal organic CVD, using DEZ and tert-butanol as precursors. They claimed that residual strain was higher for films with fewer oxygen defects (vacancies) present in the lattice structure. They linked their results to annealing studies, where the generation of oxygen vacancies was investigated and a correlation between luminescence and diffraction studies was made [100, 101]. With regard to the present study, it is proposed that increased ethanol flow rate during deposition results in fewer oxygen vacancies, leading to increased residual stress in the films.

The conduction mechanism of ZnO is still debated in the literature. As-grown ZnO exhibits n-type behaviour. This is ascribed mainly to defects in the ZnO lattice structure. Intrinsic defects like oxygen vacancies or zinc interstitials, as well as extrinsic defects due to additional doping (e.g. with aluminium, boron, or gallium), act as donors and determine the amount of free carriers in the conduction band of ZnO and its n-type conductivity. A recent review about defects in ZnO was published by McCluskey et al. [32]. As the ZnO films discussed above were deposited without extrinsic doping, it is proposed that the changes in resistivity in Figure 4.4 originate in part from changes in the intrinsic defect density, where the defects act as donors. Lany et al. [102] suspected metastable vacancies behaving as shallow donor states to be responsible for the n-type conductivity of ZnO. However, oxygen vacancies alone, without other native point defects, are not believed to be the predominant cause of the n-type conductivity [32]. With a calculated energetic position within the band gap of 0.5 to 0.8 eV above the valance band maximum, an oxygen vacancy is a deep rather than a shallow donor [32]. More recently, Janotti et al. [33] showed that hydrogen can occupy an oxygen substitutional site, which can be interpreted as an oxygen vacancy with a single hydrogen atom in the centre. This defect is assumed to act as a shallow donor in as-grown ZnO [103]. This implies that fewer oxygen vacancies in ZnO mean fewer available sites for substitutional hydrogen acting as a shallow donor. As a consequence, the electron concentration decreases, thus increasing the resistivity of the ZnO, as observed in Figure 4.4. Following this line of reasoning again confirms the claim that increasing ethanol concentration during film deposition facilitates the incorporation of oxygen at oxygen vacancies at the ZnO surface during layer growth. Apart from crack formation at high ethanol concentrations, grain boundaries may influence conductivity as well [37].

Evidence of decreased electron concentration inside the ZnO grains is found in the infrared (IR) reflection spectra, shown in Figure 4.5. Steinhauser et al. [37] showed that the IR reflection signal of LPCVD ZnO:B is significantly influenced by the concentration of free carriers, which depends on the doping level. The sudden increase in reflection can be explained by Drude's theory and is directly correlated to the electron plasma mode frequency, ω_p [37, 104]:

$$\omega_p^2 = \frac{N_e e^2}{\epsilon_0 m^*} \quad (4.1)$$

where N_e is the electron density, e the elementary charge, ϵ_0 the permittivity of free space, and m^* the effective electron mass. As expected, the onset of reflection is shifted toward higher wavelengths for ZnO deposited with ethanol due to its lower electron concentration. For more details see Section 2.1.4. Applying Drude's theory one can derive the electron concentration of the ethanol-free sample in the order of 10^{19} cm^{-3} from the spectrum shown below. For the ZnO sample deposited with ethanol the electron concentration is estimated to be in the order of 10^{17} cm^{-3} or even lower.

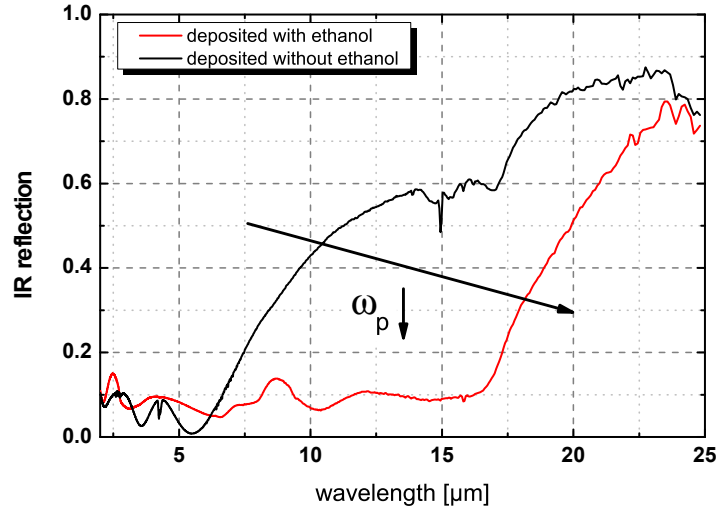


Figure 4.5: IR reflection spectra of $2 \mu\text{m}$ thick ZnO films deposited without ethanol and with 20 sccm of ethanol. The arrows indicate a decrease of ω_p which is correlated with a shift of reflection signal to longer wavelength.

To further support our growth model based on the incorporation of oxygen, another indication can be discussed. In Figure 4.6 the transmission of samples deposited with different ethanol mass flow rates in the vicinity of the optical absorption edge of the ZnO material is shown. The position of the optical absorption edge was determined by extrapolating the linear part of the spectra toward the x-axis. The values for different mass flow rates of ethanol are shown as inset in Figure 4.6 in units of eV. One can see that the absorption edge is shifting toward higher energy values (shorter wavelengths) when the ethanol flow rate is increased. There are different explanations to be considered. The first one deals with the presence of donor electrons. Here, the electrons fill and occupy the bottom states of the conduction band, so that higher excitation energies are required to excite electrons from the valence into the conduction band. As a result the effective optical absorption edge shifts, with increasing electron concentration, to higher energies. This phenomenon is well known as Burstein-Moss shift [39]. From the present results derived and discussed above a decreasing electron concentration is derived with rising ethanol mass flow rate during layer deposition.

Considering that one would rather expect a decrease of the optical absorption edge instead of an increase.

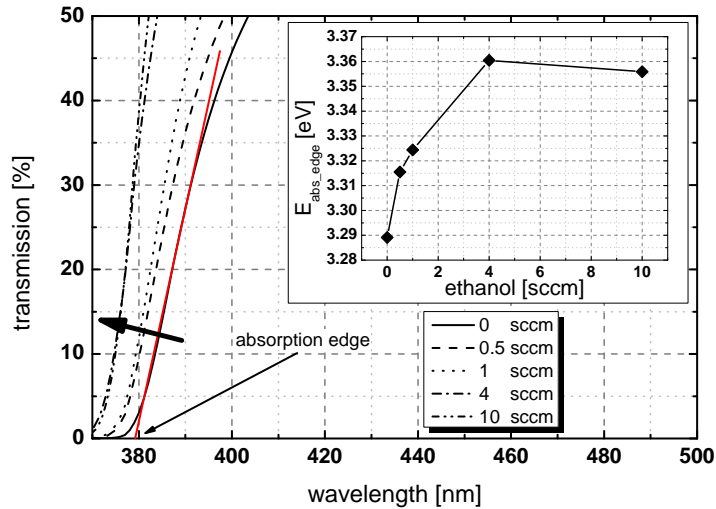


Figure 4.6: Optical transmission next to the optical absorption edge of glass samples covered with ZnO, deposited with and without ethanol. The optical absorption edge is shifting towards shorter wavelengths (higher energies). The inset shows the determined position of the absorption (E_{abs_edge}) edge in units of eV for different ethanol mass flow rates.

The second phenomenon to be considered to influence the optical absorption edge is the presence of tension. As discussed above, the *c* plane distances of the samples investigated were found to be increased compared to the one of the ZnO powder reference. Furthermore, the *c* plane distance was observed to increase with increasing the ethanol mass flow rate. That indicates a tensile stress component parallel to the *c*-axis, which in the present case was analyzed perpendicular to the surface. Therefore, one can assume a compressive force at work, acting within the plane of the ZnO layer. This is in agreement to the results of Pagni et al. [99], who investigated the influence of the oxygen zinc ratio on the properties of CVD-grown ZnO films on glass slides. Note that Pagni et al. [99] assigned the increase of the *c* plane distance with a risen oxygen zinc ratio to decreased presence oxygen vacancies. Nevertheless, they found no clear trend on the optical absorption edge. Srikant et al. [41] discussed the effect of tension on the optical absorption edge of ZnO thin films. For an in plane film compression they predict the optical absorption edge to shift red. Again, in the present case that contradicts our observation, since a blue shift was observed. Note, that several mechanisms influencing the optical absorption edge are present at same time and should be carefully considered.

The third phenomenon, having impact on the optical absorption, is correlated with defect absorption. In the literature oxygen vacancies are discussed to create a band of defects just above the valence band maximum within the band gap [40]. This in turn leads to defect induced light absorption causing a shift of ZnO absorption edge towards longer wavelengths. As proposed, the addition of ethanol during the layer

deposition, leads to the reduction of oxygen vacancies, which in turn would lead to the observed shift of the optical absorption edge towards shorter wavelengths (higher energies). As discussed it is likely that the latter effect is the dominating, since the other ones discussed contradict the present observations.

Impact of ethanol on light scattering properties

In Figure 4.7, the haze is shown as a function of the ethanol mass flow rate used during layer deposition. For haze definition see Section 3.1.1. The haze decreases from 50 to 3% as the ethanol concentration is increased.

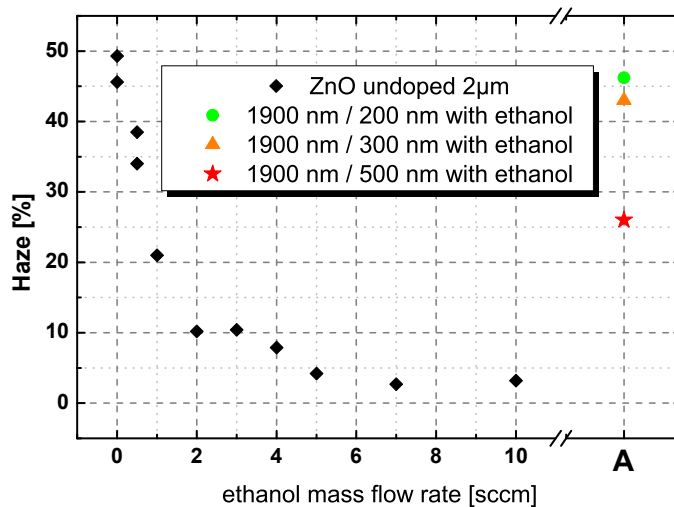


Figure 4.7: Evolution of haze at 600 nm as a function of ethanol mass flow rate during the deposition of 2 µm thick ZnO films. The data in column A of the current figure are for bilayers. Here, ethanol was used only during the cap layer deposition. Details are discussed in Section 4.3.2

This is expected from a smoothening of the surface morphology, as already observed in Figure 4.2. The root mean square (RMS) roughness, deduced from AFM measurements, is reduced from 76 to 11.5 nm as the ethanol mass flow rate is increased from 0 to 10 sccm. To check the suitability of our ZnO with its smoothened morphology, an appropriate next step would be to use it as a front electrode for µc-Si:H thin-film cells. However, the high resistivity of such films rules this out. Therefore, to circumvent this issue, a bilayer approach was investigated.

4.3.2 Ethanol-enriched bilayers

For the bilayer approach discussed in the following a 1900 nm thick ZnO bulk layer was deposited on a glass substrate before the addition of 20 sccm of ethanol during the deposition process introduces the cap-layer deposition. In Figure 4.8a a sketch of the bilayer stack is shown (bottom). The impact of the cap-layer to the surface morphology will be discussed later. The results in Figure 4.9 present measured data of

sheet resistance values gained from samples with cap-layer thicknesses varying between 0 and about 700 nm. It is interesting to note, that with increasing cap-layer thickness, no clear trend can be observed. In an approximation we conclude the sheet resistance of all measured samples is equal and about $36 \Omega/sq$, in average. Such behaviour can be expected although the ethanol-enriched layer possesses much higher resistivity, see Figure 4.4. For better understanding, a simplified equivalent circuit of resistors is shown in Figure 4.8b, at the top. Since we measured with a collinear four point probe configuration the sketched circuit between the probes S1 and S2 it can be assumed to be the same between S3 and S4.

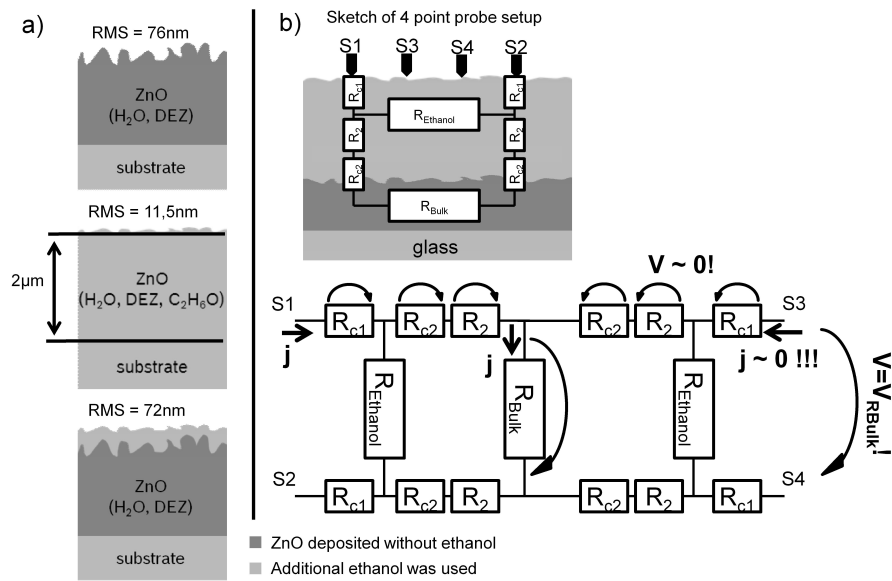


Figure 4.8: a) Sketch and RMS surface roughness of ZnO layers grown without ethanol (top), with 10 *sccm* of ethanol (center), and of a bilayer consisting of a standard 1900 nm thick ZnO layer capped by a 200 nm thick ZnO film deposited with 20 *sccm* of ethanol (bottom). Layers have a equivalent thickness of 2 μm. b) shows a simplified equivalent circuit diagram of an ethanol-enriched bilayer stack to evaluate the sheet resistance results presented in Figure 4.9. R_{c1} and R_{c2} are assigned to the contact resistances at the interfaces. R₂ is assigned to resistance current has to pass through the cap-layer in order to enter the ZnO bulk material. R_{Ethanol} and R_{Bulk} are assigned to the volume resistance of cap-layer and ZnO bulk material.

The full simplified circuit, representing the measurement configuration, is shown in Figure 4.8b, at the bottom. R_{c1} and R_{c2} are assigned to the contact resistances between measurement probes on top of the surface and ethanol-enriched ZnO cap-layer and between cap-layer and bulk ZnO material, respectively. R₂ is assigned to the resistance the current has to run through in order to enter the ZnO bulk material. R_{Ethanol} and R_{Bulk} are assigned to the volume resistance of cap-layer and ZnO bulk material, respectively. Current is introduced into the circuit on the left hand side through S1 and is leaving through S2. According to the current a voltage will drop across R_{c1}, R_{c2} and R₂, which should increase linearly with thickness of the ethanol-

enriched cap-layer. From Figure 4.4 we know that the resistivity of the ethanol-enriched layer, determining in first approximation R_2 and especially $R_{Ethanol}$, is about 4 to 5 orders of magnitude higher compared to the one of the ZnO bulk material. Since $R_{Ethanol}$ and R_{Bulk} are interconnected parallel, the lower R_{Bulk} will determine the overall resistance of the parallel circuit. The voltage needed to derive bilayer's effective sheet resistance is measured between S3 and S4, with the circuit on the right hand side. Hence, the current passing the circuit is very small, not least because of the typical high internal resistance of the voltmeter, connected to S3 and S4. As a result the voltage drop across R_{c1} , R_{c2} and R_2 can be neglected and the voltage measured is equal to the voltage drop across R_{Bulk} . The setup is not sensitive to R_2 , which is the explanation of the observed results in Figure 4.9. Even if R_2 rises due to increasing thickness of the ethanol-enriched cap-layer the determined sheet resistances will remain constant.

Nevertheless, R_2 of course might be important for future applications. When applying ethanol-enriched bilayers as front electrode for thin film solar cells, R_2 contributes to cell series resistance and lower the fill factor. This can be translated into losses in conversion efficiency. One would have to make a trade-off between possible beneficial effects of the adjusted surface morphology and an increased series resistance. But note, the bilayers discussed in the present work were deposited without the addition of an extrinsic doping source. For ZnO deposited with a LPCVD process, boron in form of diborane (B_2H_6) is typically used as extrinsic doping source. With boron the free electron concentration in the ZnO can be adjusted in the range of 10^{19} to $10^{20} 1/cm^3$, which could solve the mentioned resistivity issues.

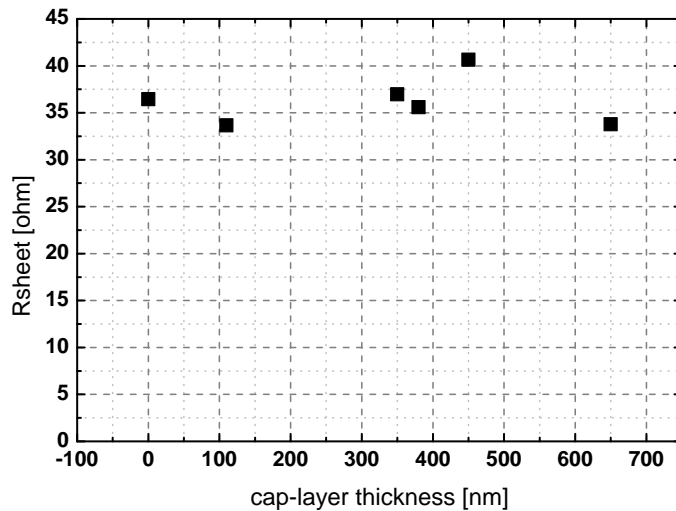


Figure 4.9: Sheet resistance of ethanol-enriched bilayers as a function of cap-layer thickness. The ZnO bulk layer was deposited without ethanol whereas for the cap-layer, in addition to the main precursors, 20 *scm* of ethanol were used. The ZnO bulk layer had a thickness of 1900 *nm*.

The influence of the cap-layer on the surface morphology is sketched in Figure 4.8a (bottom) and exactly shown in Figure 4.10b. Even for bilayers the smoothing effect

of adding ethanol during deposition is observed. Figure 4.8a shows that the RMS surface roughness is slightly reduced from 76 to 72 nm for a 1900 nm thick standard ZnO layer capped by a 200 nm thick ZnO film enriched with ethanol during deposition. Note that Figure 4.6, column A, shows that, with increasing cap-layer thickness, the haze is reduced from nearly 47% for a 200 nm thick cap layer to 26% for a 500 nm thick cap-layer.

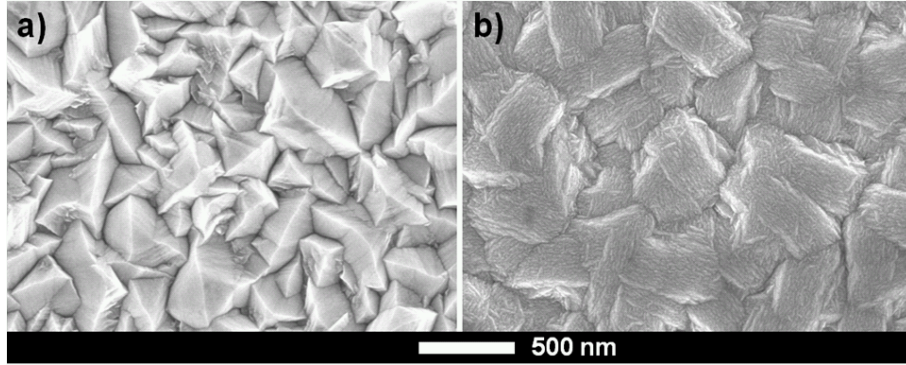


Figure 4.10: SEM images of a) the surface of a standard 2 μm thick as-grown rough ZnO film and b) a bilayer consisting of a 1900 nm thick standard ZnO film capped by a 200 nm thick ZnO layer deposited with ethanol.

4.4 Conclusion

The present work tested the suitability of adding ethanol during ZnO:B deposition to create a surface morphology that is more favorable for $\mu\text{c-Si:H}$ growth. A strong impact on the electrical and optical properties of 2 μm thick ZnO layers deposited with ethanol as an additional precursor was found. It is proposed a growth mechanism in which oxygen incorporation on oxygen vacancies is mediated by ethanol. Although ethanol-enriched ZnO single layers might be suitable for good $\mu\text{c-Si:H}$ growth, their high resistivity rules out their usage as electrodes for photovoltaic applications. In a two-step deposition process, a 200 nm thick ZnO cap layer on top of a 1900 nm thick as-grown rough ZnO film was deposited. A change in surface morphology was observed for these bilayers as well.

Furthermore, the sheet resistance of bilayer films was maintained at reasonable values, independent of the thickness of the ethanol-enriched cap-layer. It was found that the used four point probe measurement was not sensitive to the resistive cap-layer. To solve resistivity issues, which might become a problem for the potential application of bilayers, additional doping of the underlying and cap layers still has to be studied.

Future work will have to be done to investigate the effects of parameters like pressure and temperature on morphology. Also, other types of precursors will be evaluated. Finally, a complete solar cell, incorporating an optimized bilayer as the front electrode, will have to be tested. Work has been carried out by Ding et al. incorporating the

above presented approach into a micromorph solar cell [105]. Cell efficiencies above 12.2% were achieved.

Chapter 5

Integration of Advanced-TCO into the Production Line at Bosch

By using the LPCVD process, Ding et al. [1,2] introduced a novel and advanced LPCVD ZnO:B. In this Chapter, this type of TCO will be called ATCO. The ATCO approach combines a highly doped ZnO:B seed layer with a low-doped bulk layer above. ATCO, in opposition to standard TCO (Std-TCO, which is uniformly doped throughout the whole layer cross section), possesses both higher transparency due to less free-carrier light absorption in the infrared spectral range and higher haze, while maintaining the level of conductivity. The haze parameter is correlated to the film's light-scattering ability and influences the absorption of light in the absorber material of the top (a-Si:H) and bottom ($\mu\text{c-Si:H}$) cells that are combined to form a micromorph tandem solar cell device.

For more details the reader is referred to the Refs. [1,2] and to the project results reported in Ref. [6]. Whereas the deposition process was invented by Ding et al. on the same small deposition system shown in Figure 2.2, within the framework of the PEPPER project, the deposition process was scaled up (to substrate sizes of $1.1 \times 1.3 \text{ m}^2$) by Tokyo Electron Solar AG (TEL Solar, formerly Oerlikon Solar). For this, the TCO1200 deposition system, as shown in Figure 2.3, was retrofitted. With the retrofit of the deposition system TCO1200 it became possible to deposit ATCO on a commercially available production line tool.

In this Chapter the introduction of ATCO into the production line at Bosch Solar Thin Film (BSTF) is presented. First, brief comments on the retrofitted deposition tool TCO1200 are given. Then results on the process optimization done at the production site at BSTF in Erfurt (Germany) are shown. A comparison of the electrical and optical properties of ATCO and Std-TCO is presented. Finally the module performance achieved so far using ATCO as the new front electrode is reported.

5.1 Experimental

In general the deposition process of ATCO follows the process as introduced in Sections 2.1.1 and 2.1.1.2. A schematic of the deposition tool TCO1200 is shown in Figure 5.1.

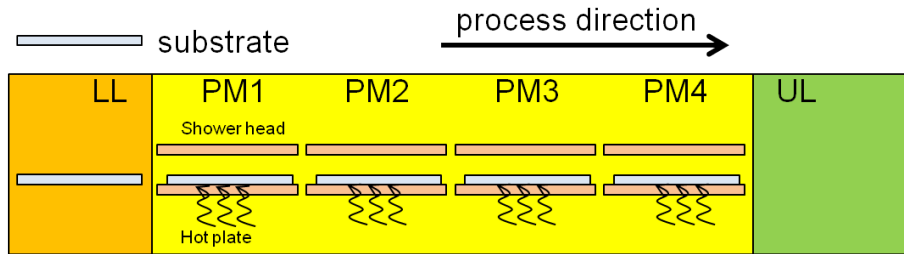


Figure 5.1: Schematic of the deposition tool TCO1200. LL, PM and UL refer to the load lock, process module and unload lock, respectively.

As depicted, the TCO1200 deposition system features a loadlock (LL) for heating up the substrates, four process modules (PM#), where the deposition takes place, and an unload lock (UL) to release the covered substrates back to the normal environment. LL and UL are separated from the PMs by gate valves to ensure a constant pressure in the PMs and to be able to transfer substrates from and back to the normal environment during deposition. The PMs are interconnected so that the pressure and atmosphere is the same in all PMs. After a substrate is heated in LL, it is transferred into PM1. Here, one quarter of the total layer thickness is deposited. The second, third and fourth quarters follow with the transfer into and deposition in PM2, PM3 and PM4. In order to deposit a highly doped seed layer within PM1 underneath a low-doped bulk layer, TEL Solar retrofitted an additional doping gas line for diborane (B_2H_6) to the shower head of PM1. Even though the four PMs are atmospherically interconnected, this has been proven to be the simplest solution. The gas line allows for additional doping of the first 100 – 200 nm of ZnO:B in PM1. This approach proved to be sufficient even though one has to accept a certain cross talk between PM1 and PM2, which will be discussed later.

After ZnO:B deposition, the substrates were analyzed by measuring thickness, sheet resistance (R_{sq}), haze and transmission. Thickness and R_{sq} were evaluated within a matrix of 8×8 measurements distributed equidistantly over the $1.4 m^2$ substrate. Thickness was determined by means of reflectance measurement. For the haze measurement the substrates were cut into small samples originating from 13 distinct positions, including samples of the edges, diagonals and the center. For this central sample, the transmission was measured with matching refractive indices as well. Here, diiodomethane (CH_2I_2) which possesses a refractive index of about 1.7 is applied to the ZnO:B surface. The liquid is then covered by a thin borosilicate glass, 0.5 mm thick. Thus, losses in transmission which can be observed due to haze in the spectral range below the absorption edge, causing misinterpretation, are avoided.

5.2 Results

As mentioned in Section 5.1, the upgrade of the TCO1200 deposition system gives rise to a certain cross talk between PM1 and the other process chambers. In order to study this effect, four substrates were loaded into PM1 to PM4. After reaching thermal equilibrium a ZnO:B film with a nominal thickness of 1700 nm was deposited in 514 seconds in PM1 to PM4. For the deposition, the ratio of mass flow rates of $[H_2O]/[DEZ]$ and $[B_2H_6]/[DEZ]$ was adjusted to 1.28 and 0.04, respectively. Due to the additional mass flow rate of diborane in PM1 the resulting ratio of $[B_2H_6]/[DEZ]$ in PM1 was set to be 0.84. In Figure 5.2, results of sheet resistance and thickness are shown for all PMs.

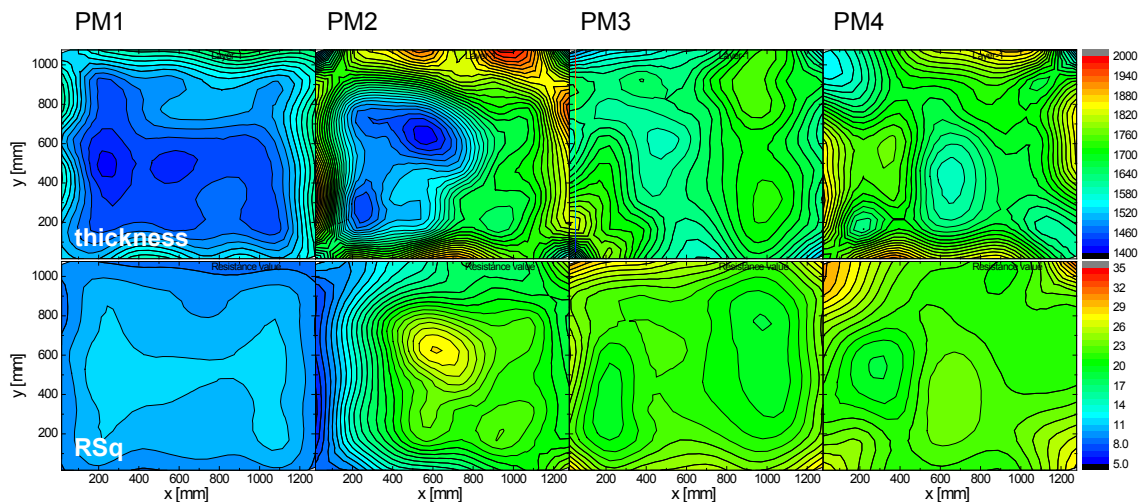


Figure 5.2: Distribution of layer properties after the retrofit of TCO1200, doing a single-chamber deposition with an additional mass flow rate of B_2H_6 of 500 sccm in PM1.

Due to higher doping ratio in PM1 the average sheet resistance results in a lower average value of $8\ \Omega$ compared to the values reached in PM3 and PM4 of about $20\ \Omega$. On the left side in PM2 one can clearly see the cross talk. Here, diborane spread into PM2 due to higher partial pressure of diborane in PM1 causing a lower sheet resistance. The average thickness in PM1 is obviously reduced in comparison to those of PM3 and PM4. In PM2 an area of minimal deposition rate was found. This feature is attributed rather to an undesired particle placed between the hot plate and the substrate – presumably ZnO – and therefore a locally lower substrate temperature, than to the higher flow rate of diborane in PM1. The lower thickness / deposition rate in PM1 seems to result from a thermal cooling effect (high flow regime) or a reduced adatom residence time induced by a higher total mass flow rate.

The TCO1200 deposition system runs in normal mode during production. Substrates are transferred from the normal environment to LL, from LL through the four PMs into UL, and from UL back to the normal environment every two minutes. The first results of layer properties of ATCO and Std-TCO are compared in Figure 5.3.

The process of ATCO seems to slightly benefit the thickness uniformity, as compared to the one of the Std-TCO process. Furthermore, we can conclude that the cross talk is much less prominent than what would have been expected from the results shown in Figure 5.2. Only small pronounced characteristics can be observed for sheet resistance values.

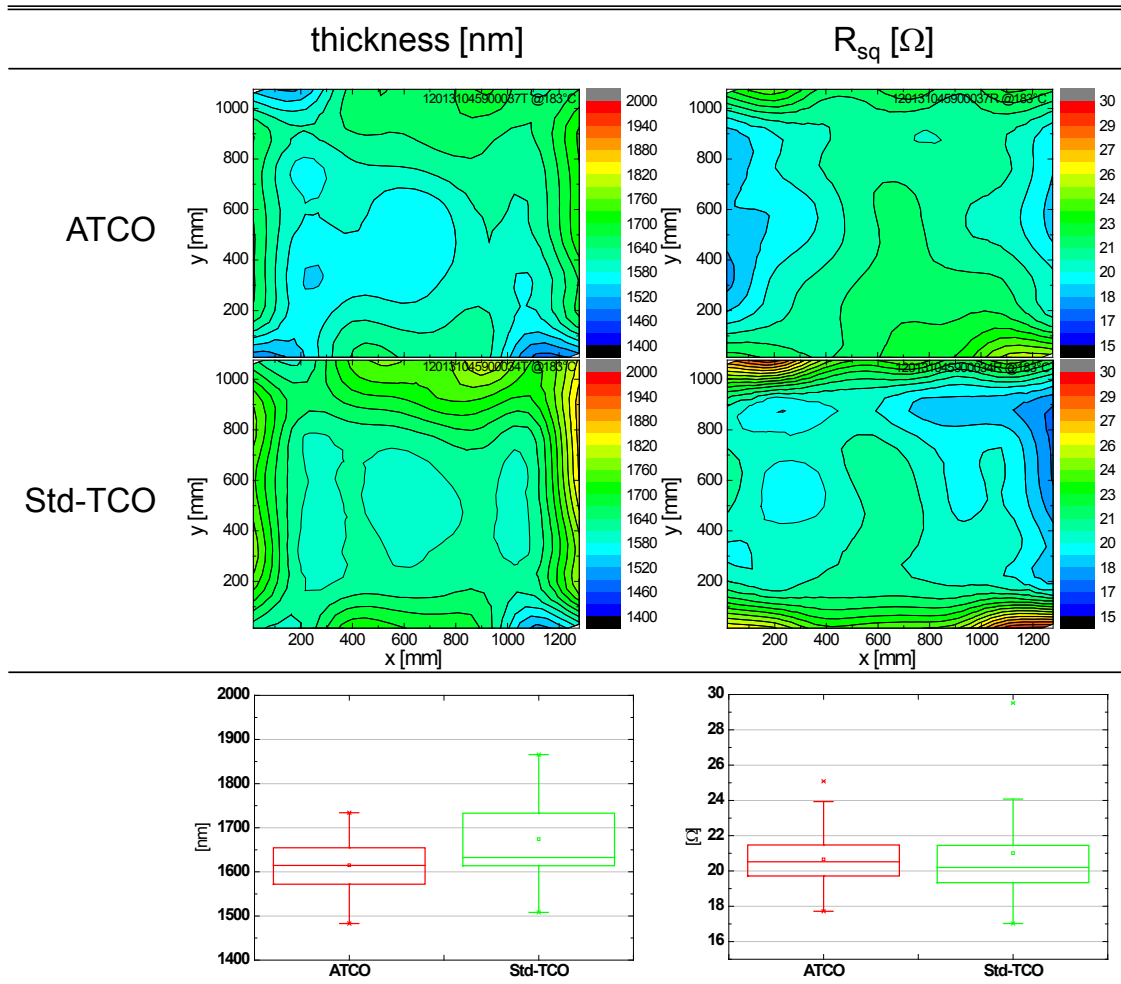


Figure 5.3: Comparison of ATCO and Std-TCO running the TCO1200 deposition system in production mode.

As a next step, the optimization of parameters like deposition temperature, pressure, mass flow rate ratio of water to diethylzinc and doping were conducted in order to optimize haze, transmission and resistivity for a final layer thickness of 1800 nm.

5.2.1 Variation of process temperature

The most sensitive parameter for depositing LPCVD ZnO:B is the substrate temperature. For the regime under consideration, the grain size can be optimized by varying the temperature for a given set of precursor flow rates [27]. For a certain deposition temperature, T_c , and film thickness, grain size becomes largest. The grain size for $T < T_c$ and $T > T_c$ is decreased. Also, the preferred crystallographic orientation of the

ZnO:B grains changes. Since LPCVD ZnO:B possesses a wurtzite structure, the preferential orientation of grains at T_c belongs to the a-axis. Temperatures in the vicinity of T_c coincide with highest haze and lowest resistivity for a given layer thickness. It has been found by tests at BSTF, here not further discussed, that the optimal temperature (T_{opt}) for LPCVD ZnO:B deposition suitable for micromorph tandem devices is slightly below T_c . The results of our temperature variation are summarized in Figure 5.4.

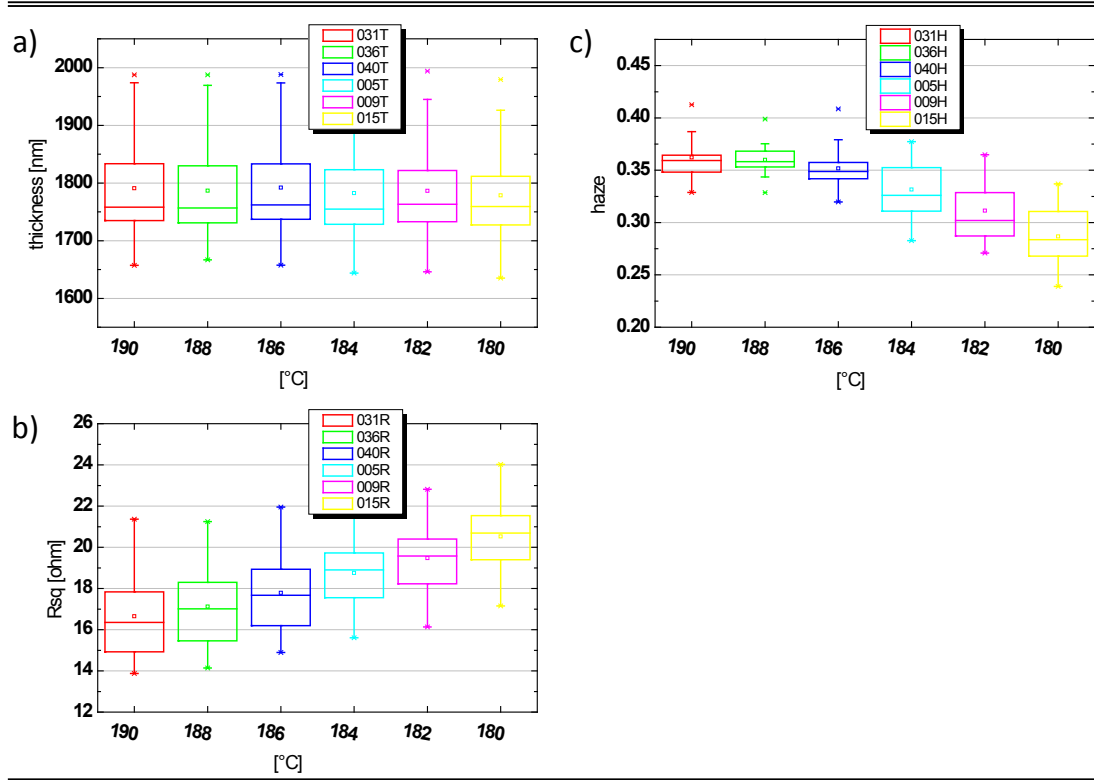


Figure 5.4: Variation of process temperature. The temperature of the center heater of the PMs is specified. The LL outlet temperature was set at 180°C. Results are shown for (a) equivalent thickness of each evaluated sample, (b) the evolution of sheet resistance, R_{sq} , and (c) the evolution of haze parameter.

Since the deposition rate of ZnO varies with the temperature, the deposition time was adjusted in order to get substrates covered with ZnO:B of equivalent thickness, see Figure 5.4a. The outlet temperature of substrates leaving LL into the first PM was set to 180°C and the temperature of the PMs heaters was varied. From experience it is known that substrates cool when transferred from PM to PM. So the substrates experience an average growth temperature that can be adjusted by changing the LL and/or hot plate temperature. Despite the real surface temperature being unknown, one is thus possible to determine a suitable growth regime from parameters like sheet resistance and haze, see. Figures 5.4b and 5.4c.

As shown in Figure 5.4b, the sheet resistance is decreased while the haze in Figure 5.4c is enhanced by increasing the heater temperature from 180 to 190°C. With the trend mentioned, we observe an improved grain size and a deposition regime equiva-

lent to $T < T_c$. The results shown above indicate an optimized deposition temperature (T_{opt}) of about 188 °C. In our experience, T_{opt} strongly depends on maintenance conditions, which are mainly influenced by the number of substrates passed through the TCO1200 deposition system. With an increasing number of substrates the deposition rate tends to be reduced. This can be ascribed to an undesired deposition of ZnO:B on the PM's gas shower heads and hot plate edge bars changing the thermal equilibrium. Despite a constant set of deposition parameters including temperature, the true substrate surface temperature decreases with substrate count. Obviously T_{opt} has to be adjusted in order to retain the ZnO:B layer properties.

5.2.2 Variation of water-diethylzinc ratio

The ratio between water (H_2O) and diethylzinc (DEZ, $(C_2H_5)_2Zn$) is a very important parameter for the deposition process of LPCVD ZnO:B. The amount of water as the source of oxygen influences parameters like film stoichiometry and electrical and optical properties. The surface morphology of the films especially can be changed dramatically [106]. In Figure 5.5, results of the variation of the $[H_2O]/[DEZ]$ ratio are shown.

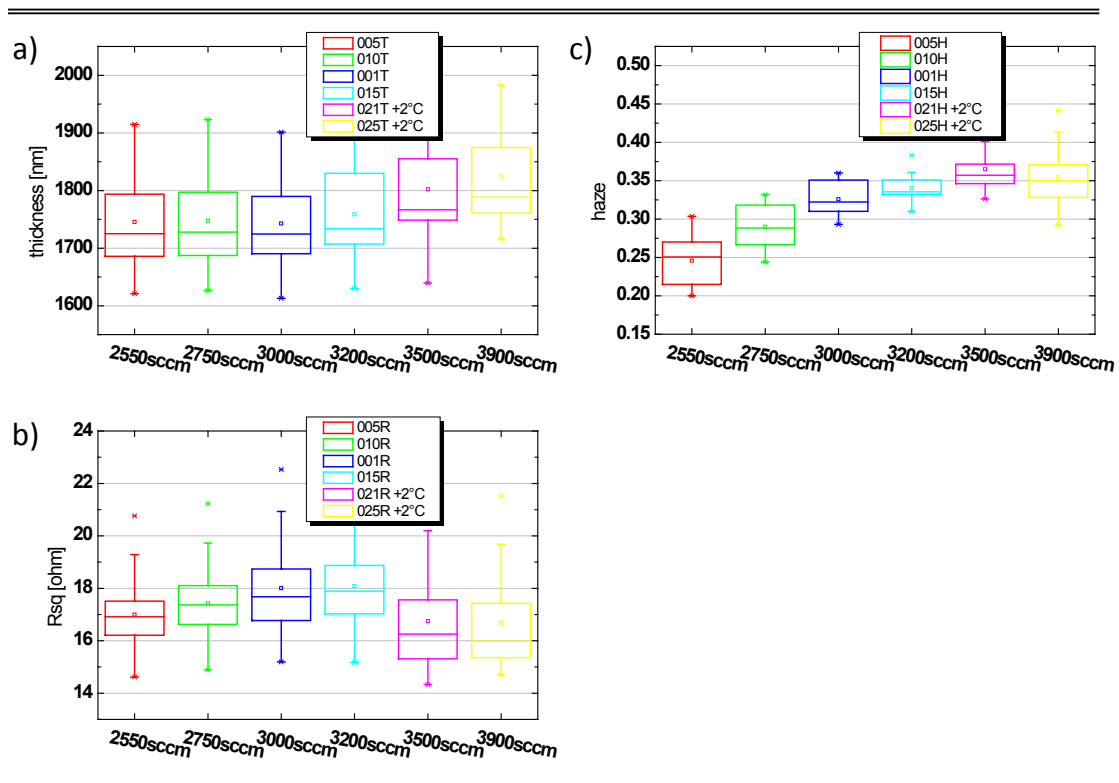


Figure 5.5: Variation of the water/DEZ ratio. The current water flow is displayed on the x-axis. DEZ flow is set to a fixed value of 2500 sccm. Results are shown for the (a) thickness of each sample, (b) sheet resistance and (c) haze parameter.

In contrast to the experiment discussed in Section 5.2.1, the deposition rate is much less sensitive to the mass flow rate of water and its given ratio to DEZ. The deposition

in the present case was not adjusted to achieve equivalent thicknesses for the different mass flow rates tested. As seen in Figure 5.5a, the values are very similar. For water mass flow rates of 3500 and 3900 *sccm* the deposition temperature was slightly higher, $\Delta T = 2^\circ\text{C}$, as indicated. From experience it is known that the average thickness deposited within 548 *s* increases by 30 to 50 *nm* for $\Delta T = 2^\circ\text{C}$. Nevertheless, it is acceptable to evaluate the regime of $[H_2O]/[\text{DEZ}]$ ratio. In Figure 5.5a one can see the total film thickness increases only slightly when the mass flow rate of water is increased from 2550 to 3900 *sccm*. For mass flow rates of 3500 and 3900 *sccm*, the thickness should be reduced by 30 to 50 *nm*. The sheet resistance in Figure 5.5b increases when the mass flow rate of water is increased from 2500 to 3200 *sccm*. Even though the sheet resistance is shown to be lower for higher flow rates, we expect the values to be on the same level as the value for 3200 *sccm* when deposited with a deposition temperature of 2°C less. This would result in a lower thickness (30 to 50 *nm*), thus in higher sheet resistance. The effect of different water mass flow rates on the haze is shown in Figure 5.5c. As can be seen, the haze is maximized by increasing the water mass flow rate from 2500 to 3900 *sccm*. Since the thickness of samples deposited with 3500 and 3900 *sccm* is slightly higher, the haze values have to be assumed to be 0.01–0.02 lower. So it matches with the values achieved for the deposition of ZnO:B with a water mass flow rate of 3200 *sccm*. The improvement in haze with increasing the flow rate of water indicates an increase in grain size which coincides with a surface morphology that tends to be more rough compared to the ones at lower water mass flow rates. Considering a DEZ mass flow rate of 2500 *sccm*, we conclude a water mass flow rate of 3200 *sccm* to be suitable for ZnO deposition, since haze has been maximized for a given film thickness and benefits from a smaller distribution of measured values.

5.2.3 Variation of process pressure

A pressure series was prepared to check for variations around the usual process pressure of 0.5 *mbar*. The results are shown in Figure 5.6. The main effect found was a correlation with deposition rate, which is enhanced by raising the process pressure (not shown here). No significant impact was observed on *Rs_q* and haze, for equivalent thickness, see Figure 5.6a. Merely a beneficial effect on haze uniformity was found for lower process pressures, see Figure 5.6c.

For constant mass flow rates and $p < 0.5 \text{ mbar}$, a lower deposition rate is thus caused by lower DEZ utilization. In her thesis [15], Faÿ stated that in the pressure range between 0.5 and 3.5 *mbar*, grain size and preferred crystallographic and surface morphology are not affected by pressure. She showed that the deposition rate can be easily doubled. This would lead to higher DEZ utilization and in turn to lower material costs for ZnO deposition. Furthermore, by doubling the deposition rate two, instead of four, PMs were sufficient for deposition. This in turn would lower the material

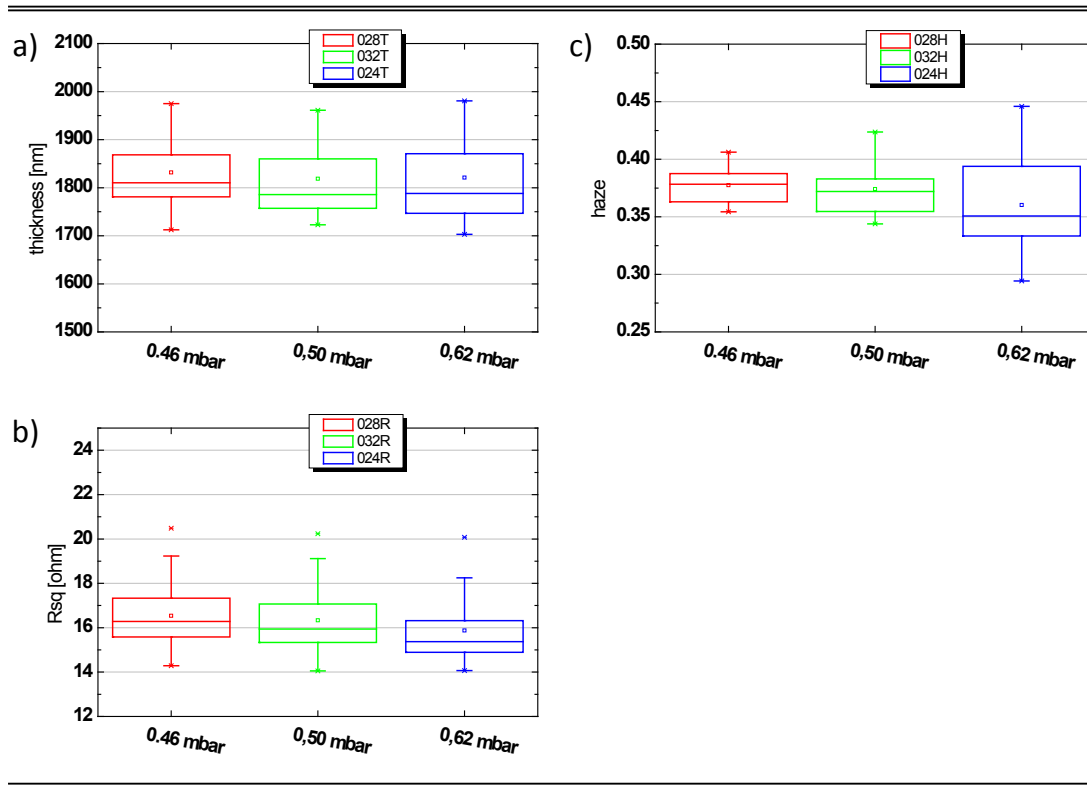


Figure 5.6: Variation of process pressure. Results are shown for the (a) thickness of each sample, (b) sheet resistance and (c) haze parameter.

costs for machine construction. As seen in Figure 5.6c, the uniformity in haze suffers from higher pressures. It is suspected that this might result in uniformity issues with thickness and sheet resistance as well. The TCO1200 deposition system is optimized for a pressure of 0.5 *mbar*. One would presumably have to engineer the gas shower heads and other machine parts in order to optimize the deposition system for a higher pressure regime. For that reason we will stick to the pressure of 0.5 *mbar*.

5.2.4 Variation of seed layers deposition time / thickness

Results of the variation of the seed layer deposition time for a total film thickness of 1800 *nm* are shown in Figure 5.7a. As can be expected from increasing the thickness of the seed layer, which is highly doped (350 *sccm* B_2H_6 additional mass flow rate in PM1 only) compared to bulk doping with 150 *sccm* B_2H_6 , the sheet resistance decreases. Note that we have to consider the bulk doping of 150 *sccm* distributed equally over the four PMs. The mentioned decrease in R_{sq} is shown in Figure 5.7b. Higher average doping leads to a decrease in haze. In Figure 5.7c no such effect is observed. Haze is fixed on average at a level between 0.36 and 0.37.

The impact of the seed layer deposition time / thickness on optical transmission is shown in Figure 5.7d. The transmission at 1200 *nm* decreases from 83 to 81% when the deposition time is increased from 30 to 59 *s*. This is assumed to be correlated to absorption losses in the seed layer due to free charge carriers. The thicker the highly

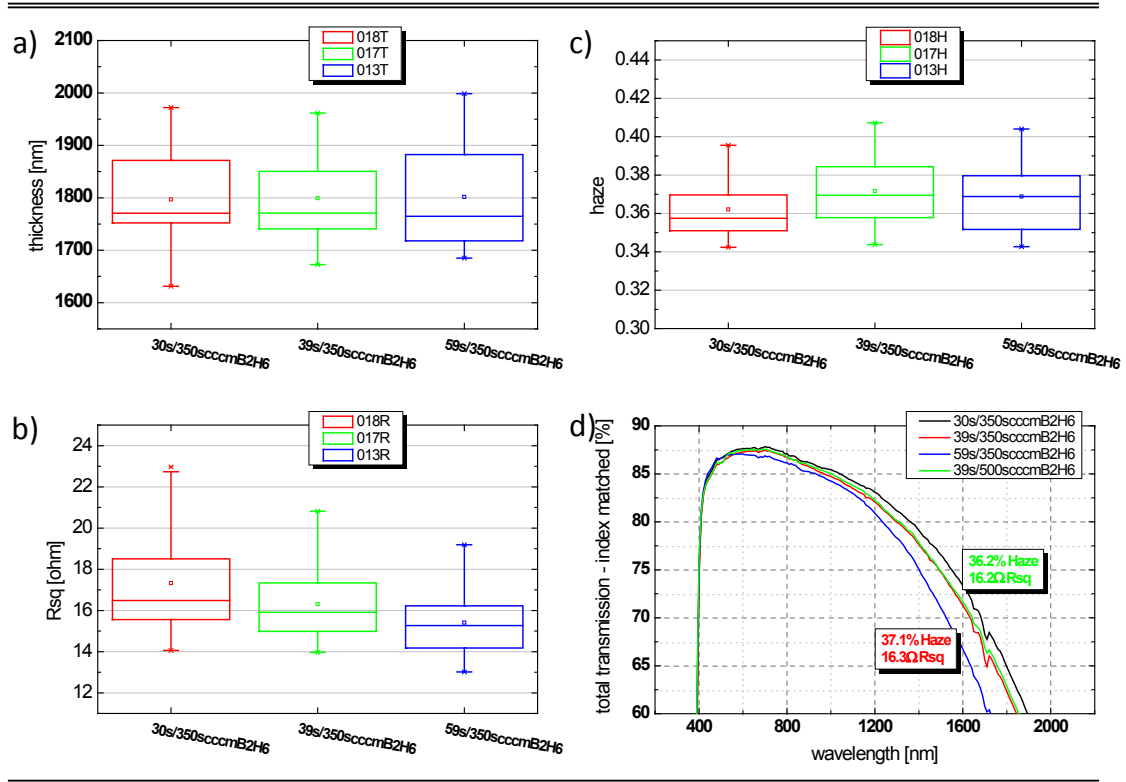


Figure 5.7: Variation of seed layer thickness. Results are shown for the (a) thickness of each sample, (b) sheet resistance and (c) haze parameter. (d) The transmission measured index matched for samples with different seed layer thicknesses (indicated by seconds). For the seed layers an additional mass flow rate of B_2H_6 of 350 and 500 sccm was used.

doped seed layer is, the higher the absorption losses are. For comparison, the influence of seed layer doping on optical and electrical properties for films of 1800 nm thickness deposited with an equivalent seed layer deposition time of 39 s was investigated. The additional mass flow rate of B_2H_6 was 350 and 500 sccm. The results are shown in Figure 5.7d. Whereas the transmission data show no significant difference, haze and sheet resistance evince the expected tendency. For a sample seed layer doped with 350 sccm, R_{sq} and haze are shown to be slightly higher than for the sample doped with 500 sccm. Due to the similarity of both layers the decision was made to fabricate ATCO front electrodes using a seed layer deposited within 39 s with an additional doping of 500 sccm of B_2H_6 .

5.2.5 Variation of bulk layer doping

For ATCO, the bulk doping in comparison to Std-TCO is reduced by about 30%. To investigate the influence of bulk doping on the electrical and optical properties of ATCO, a sample series was prepared. The results are shown in Figure 5.8. Note that a seed layer of 39 s with additional B_2H_6 doping (500 sccm) was deposited just before the bulk ZnO:B layer. The thickness was set to be equivalent, see Figure 5.8a. R_{sq} and haze are reduced raising the bulk doping from 130 to 170 sccm.

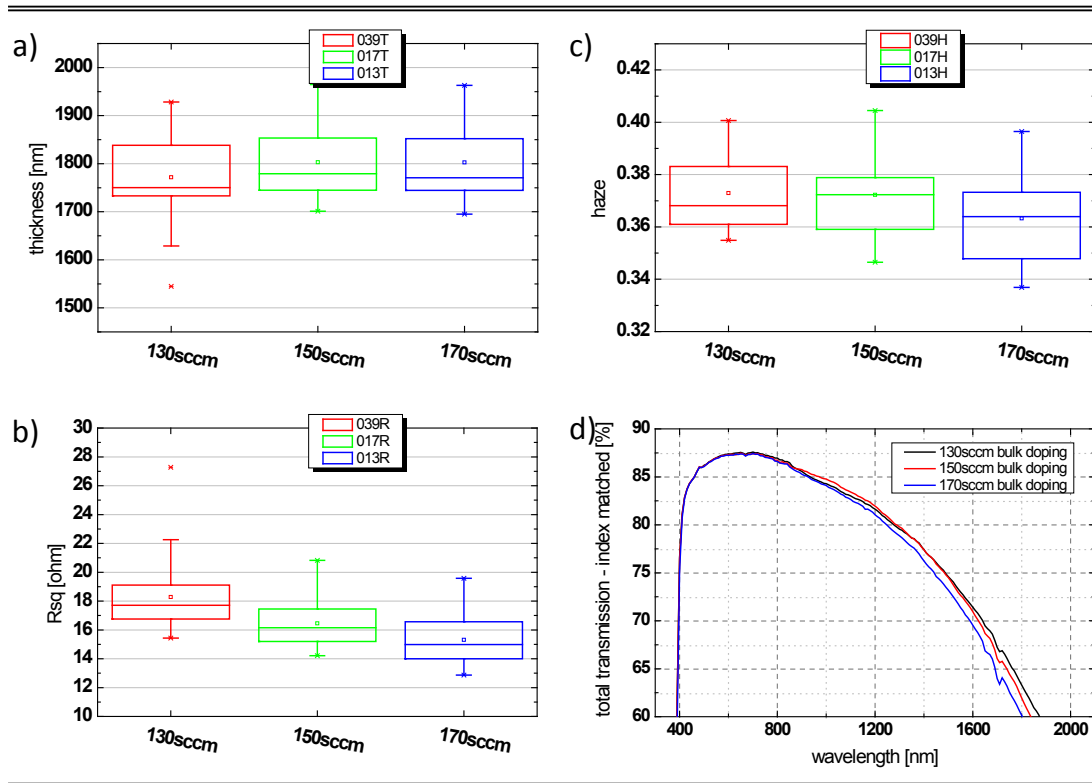


Figure 5.8: Variation in bulk layer doping. Results are shown for the (a) thickness of each sample, (b) sheet resistance and (c) haze parameter. (d) The transmission measured index matched for bulk layer with different doping.

The transmission data are shown in Figure 5.8d. Even though the changes are small, the transmission ($> 800 \text{ nm}$) can be enhanced by lowering the bulk doping. This is caused by lower free charge-carrier absorption as mentioned above. A bulk doping of 150 *sccm* is assumed to be suitable for ATCO. Even a lower doping has to be preferred in terms of lower absorption losses and higher haze. The decision is supported by the following arguments: The transmission and haze are as high as the transmission and haze for the ATCO with a bulk layer doped with 130 *sccm*. Furthermore, the somewhat higher doping (compared to 130 *sccm*) benefits lower resistivity values.

5.2.6 Comparison of ATCO vs. Std-TCO

Finally, the ZnO:B properties of ATCO and Std-TCO for optimized deposition parameters are compared. In Table 5.1, the deposition parameters for ATCO and Std-TCO are summarized. The main difference to be noted is that of bulk doping and the highly doped seed layer for ATCO.

Table 5.1: Optimized deposition parameters for ATCO and Std-TCO.

	ATCO	Std-TCO
water, H_2O [sccm]	3200	3200
DEZ, $(C_2H_5)_2Zn$ [sccm]	2500	2500
diborane, B_2H_6 [sccm]	150	215
hydrogen, H_2 [sccm]	720	720
total deposition time [s]	548	548
additional B_2H_6 in PM1	500 sccm, 39 s	
T_{opt} [°C]	188	188

As already mentioned in Section 5.2.1, the optimal temperature depends on the maintenance condition of the deposition system. Note that T_{opt} can differ by about 10°C within a cycle of maintenance. For comparisons and evaluation of the electrical and optical properties of TCOs we deposited ATCO and Std-TCO of equivalent thickness with the process parameters summarized in Table 5.1. The thickness was 1800 nm. The results are shown in Figure 5.9a, b and e. The values of thickness uniformity were found to be 0.07 and 0.09 for ATCO and Std-TCO, respectively. Average values for sheet resistance were 16.3 for ATCO and 17 Ω for Std-TCO. Significantly different values for R_{sq} uniformity were observed. With 0.19 for ATCO the uniformity is about 30% better compared to that of Std-TCO with 0.28. This can be considered to be beneficial for module fabrication. Comparing Figure 5.9c and d one sees the already mentioned cross talk between PM1 and PM2 leading to a changed distribution of resistance values. However, the main difference between ATCO and Std-TCO can be observed comparing the haze results shown in Figure 5.9g. ATCO with an average haze value of about 37% poses 3 – 5% absolute more haze compared to a Std-TCO of equivalent thickness and sheet resistance.

In Figure 5.10 the optical and electrical properties of a Std-TCO and several ATCOs deposited with slightly different parameters are compared. The ZnO:B film thicknesses were set to 1800 nm. For the comparison not only the thickness should be equivalent, but also the sheet resistance should be of the same order of magnitude, as shown in Figure 5.10. Besides the lower haze level of about 33% for Std-TCO compared to the one of ATCO with a level of 37%, Std-TCO possesses higher transparency for wavelengths > 1200 nm. This is assumed to be correlated to the doping level and its associated absorption of light due to free charge carriers. Since the bulk layer material of ATCO is doped 30% less than that of Std-TCO, it is proposed that the main absorption takes

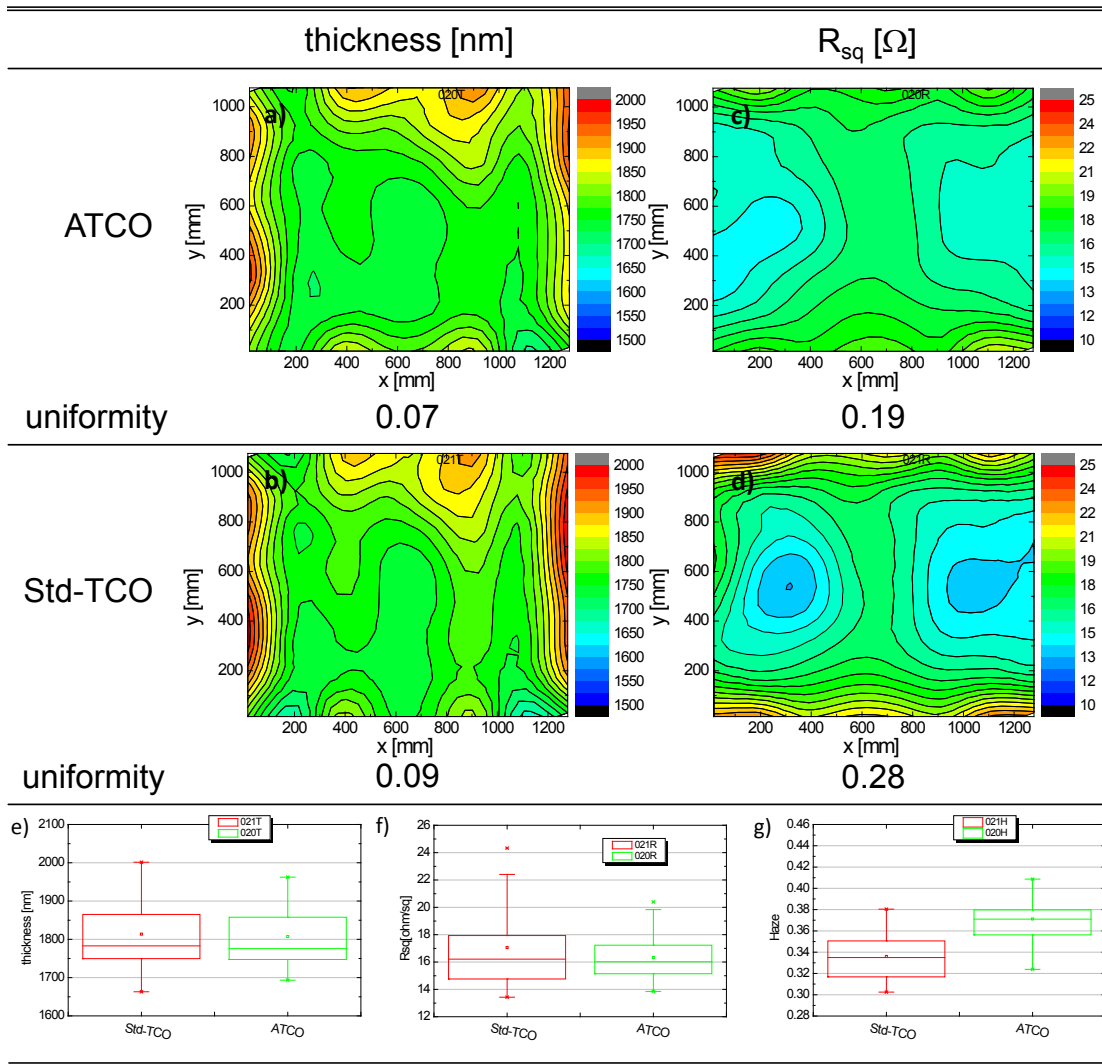


Figure 5.9: Comparison of ATCO and Std-TCO for the optimized deposition parameters. Uniformity values $((\max - \min) / (\max + \min))$ are calculated for the presented contour plots. Box plots compare achieved values for thickness, sheet resistance and haze.

place in the highly doped seed layer of ATCO. This proposition could be confirmed with the sample having the thinner seed layer (deposition time of 30 s) while keeping the level of doping unchanged, see Figure 5.10. Here the transparency above 1200 nm for ATCO was enhanced to be close to that of Std-TCO.

For the a-Si:H and $\mu\text{c-Si:H}$ absorber materials in the top and bottom cells, the relevant spectral range is below 1100 nm where the $\mu\text{c-Si:H}$ bottom cell starts to absorb the incoming light. In Figure 5.10, the transmission for all ATCOs is equal to or even better than that of Std-TCO in the mentioned spectral range. Of course that depends on the doping and film thickness, but for this reason films with similar R_{sq} and thickness were compared. Instead of undesired absorption another reason to explain the better performance for wavelengths < 1100 nm is that higher doping leads to a decrease of the refractive index. Thus, the refractive index matching to the glass for a highly doped seed layers is better than for the low-doped bulk material deposited for ATCO

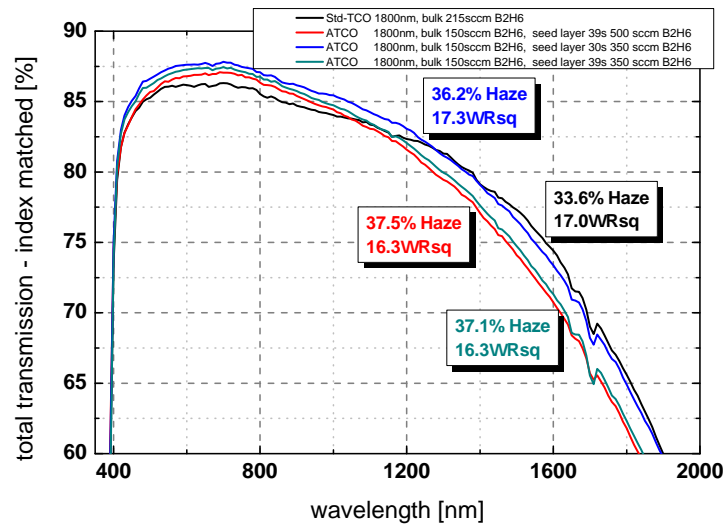


Figure 5.10: Comparison of transmission measured index matched for ATCO and Std-TCO.

and Std-TCO. This leads to fewer losses due to reflection at the glass-TCO interface. Furthermore, the seed layer may also act as a kind of antireflective layer.

5.2.7 Result on module power using ATCO

Using ATCO a maximum initial module power of 153.7 Wp was achieved, see Figure 5.11. The critical point is to adjust the PECVD deposition parameters to adapt for the high haze of ZnO:B. Here, the contact layer between the ZnO and the a-Si:H top cell and the crystallinity of the $\mu\text{c-Si:H}$ bottom cell plays a major roll.

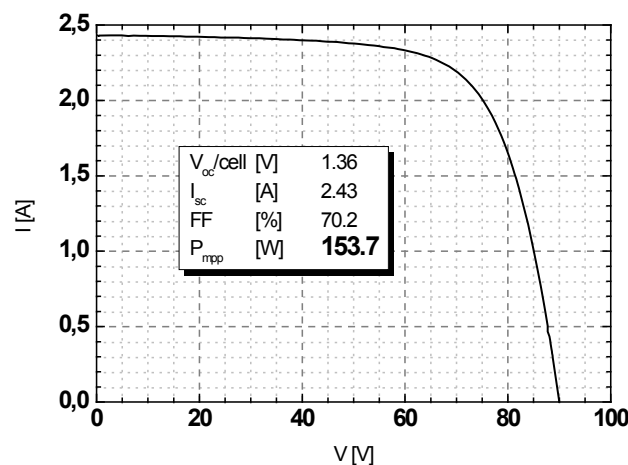


Figure 5.11: Best results achieved on ATCO with non-retrofitted PECVD equipment. The amorphous top and microcrystalline bottom cells have thicknesses of 250 nm and 1300 nm , respectively.

With the current PECVD equipment, as introduced in Section 2.2.1, the cell deposition parameters still can be fine tuned to further raise module power. For module

power above 160 Wp a new, retrofitted PECVD reactor with a lower electrode gap is required, especially for $\mu\text{c-Si:H}$ material deposition. For more details see reports in reference [6].

5.3 Conclusion

The introduction of ATCO into the production line at Bosch Solar Thin Film in Erfurt (Germany) was presented. It was shown that the retrofitted TCO1200 deposition tool is suitable for ATCO deposition. After presenting the results on process optimization, the optical and electrical properties ATCO and Std-TCO were compared. It was found that ATCO possesses better uniformity of thickness and R_{sq} values. Furthermore, ATCO possesses slightly better transmittance in the relevant spectral range of the absorber materials of the top and bottom cells. The major difference was found in the haze parameter. Whereas a 1800-nm -thick ATCO shows a haze of 37% , a Std-TCO of equal thickness and sheet resistance possesses $3 - 5\%$ absolute less haze. Finally, the parameters for PECVD deposition for the top and bottom cells were adjusted to the more rough ATCO. Here the major adjustments have to be done on the contact layer facilitating the interface between the top cell and the TCO, and on the crystallinity of the $\mu\text{c-Si:H}$ absorber of the bottom cell. Using ATCO as the front electrode, an initial module power of 153.7 Wp was achieved.

Chapter 6

Anodic degradation of ZnO:B on soda-lime glass

In the present chapter the anodic degradation of ZnO:B and its influence on thin-film silicon solar cells and modules will be discussed. In Section 6.1 introductory background informations are given. Furthermore, the cathodic degradation (the well known TCO corrosion) is summarized. Experimental details are presented in Section 6.2. General observations made for large size modules will be shown in Section 6.3. Enclosed to these results the focus of the investigation is directed to the microscopic mechanism responsible for the observed degradation phenomenon in Sections 6.4, 6.5, 6.6 and 6.7. Finally, solutions are presented in Section 6.8 which minimize the phenomenon of anodic degradation. Note that the findings presented in the following were generated under harsh conditions (contacting and/or applied voltage) derived in parts from IEC61646 10.13. Since there is a certain scarcity of information about the relation between these accelerated test conditions and the long term performance of modules in the field, the results should just be considered merely as an indicator for the module long term performance.

6.1 Background

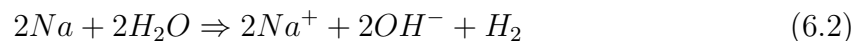
Thin-film modules have to pass many durability tests, including several accelerated lifetime tests, such as damp heat exposure in a climate chamber (IEC61646, 10.13). For this test, modules are exposed to 85°C and 85% relative humidity (r.h.) for 1000 hours. However, this test does not adequately describe the performance of a module wired in a string with other modules. In such a setup the cells in a module may be biased with several hundred volts with respect to ground (module frame or mounting system). This voltage is isolated by highly resistive module components, the front or back glass, for example. Leakage current through these resistive components may cause degradation not only in thin-film modules but also in modules based on inter-

connected crystalline silicon wafer solar cells [107, 108]. This leakage current strongly depends on the temperature of the module and the humidity of its environment. To date, in thin-film photovoltaics, especially in technologies based on the superstrate configuration, the most apparent potential-induced degradation effect is correlated to corrosion of the transparent conductive oxide (TCO), typically used as the front or back electrode [10, 109–112]. Here, the front contact (TCO) is typically deposited on commercially available soda-lime glass, followed by the deposition of the absorber material and the back contact. To protect this sensitive layer stack against environmental impact, it is laminated together with an aluminium-foil-enhanced polymer sheet or glass. According to the standard VDI2578, the main chemical components of soda-lime silicate glass are as follows by mass percentage: 73 % of silicon oxide (SiO_2), 13 % sodium oxide (Na_2O), 9 % calcium oxide (CaO) and other metal oxides which mainly influence optical properties [71]. The sodium concentration and its mobility in such glass are the root cause of the TCO corrosion mentioned above.

Due to the electric field caused by the potential difference between the front TCO and the mounting system, positively charged sodium ions in soda-lime glass migrate towards the glass/TCO interface. The cathode (TCO) reduces the positively charged sodium ions accumulated at this interface to elementary sodium according to chemical reaction 6.1 [111]:



Water is believed to play a major role in the second step of the corrosion mechanism, since moisture accelerates this kind of corrosion. Water oxidizes the elementary sodium to Na^+ and produces OH^- (at the glass/TCO interface), as proposed in reaction Equation 6.2.



The elementary or molecular hydrogen remaining from the reaction between water and sodium is assumed to reduce the TCO at the glass interface, causing an observable delamination. This has been observed for both fluorine doped tin oxide ($SnO_2 : F$) and aluminium doped zinc oxide (ZnO:Al) – common TCO materials – but ZnO:Al seems to be less sensitive than $SnO_2 : F$ to this kind of corrosion [111]. Another explanation for the delamination is the destruction of the sub-interface glass matrix due to the presence of a strong basic solution ($pH > 9$), as might be indicated by the presence of Na^+ and OH^- [113, 114]. Furthermore it was found that before irreversible delamination occurred, the accumulation of sodium could be reduced by applying a reverse bias [111]. In this case the resulting electric field forces the sodium accumulated at the glass/TCO interface to migrate back into the glass. After such a treatment no delamination was observed, even in a humid environment.

During the course of the present work another previously unknown degradation phenomenon was encountered: anodic – and not cathodic – degradation. In the following section experimental details will be presented.

6.2 Experimental

In Figure 6.1 the equipment of our biased damp heat (BDH) experiment is shown. The module under test is placed in a climate chamber fixed by a mounting system, see Figure 6.1b. There is a huge set of mounting systems available on the market. The mounting system used is of great importance, not only for the achievable installation costs, but also for the leakage current between usually grounded mounting system and mounted module, which directly impacts the long term stability of modules installed in the field. To consider a worst case scenario, which is taking into account a mounting system with highest conductivity towards the mounted module, the edges of the modules tested were equipped with conductive copper tape, see Figure 6.1c. In the present experiment the copper tape was always grounded. The connectors of the modules were shorted and set to the same potential. For the results presented in the present work we have chosen 600 V positive bias. This value is derived from the following consideration:

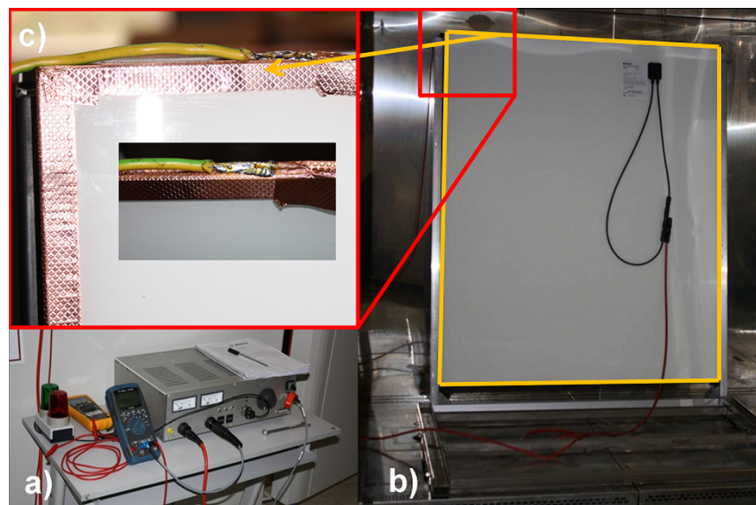


Figure 6.1: Equipment for biased damp heat experiments in the climate chamber. In (a) one can see the power supply (Bürger Electronic HP5000), which is used to apply a positive bias voltage of 600V at shorted module connectors. (b) shows the solar module to be treated in the climate chamber (Vötsch Industrietechnik VCS7340-3). To simulate the worst case scenario, the edges of the module were equipped with high conductive copper tape, which is grounded during biased damp heat experiment, see (c).

Most of today's DC/AC-converters are set up to have floating potentials with a system voltage up to 1000 V. This voltage belongs to the potential difference of the positive and negative system pole. Depending on the actual solar irradiation and on the V_{oc} of the modules string, the real and instantaneous system voltage is build up.

Since the system poles are floating the half amount of the modules wired in the string is biased with up to -500 V while the other half in the string is biased with 500 V . Furthermore, one has to consider the half grid voltage, which has to be added in case of using a transformerless inverter. In case of a grid voltage of 230 V that would mean an additional bias of about 100 V . The environmental conditions in the climate chamber were adjusted to 85°C and 85% relative humidity.

As one will see in the following sections the degradation of the ZnO:B film used in the layer stack of the solar cell (see Figure 2.12) is identified to be the main driver responsible for the reduced module performance after anodic degradation. Inspired from Jansen et al. [111], comparable tests with a hot plate were conducted. They are indented to simplify the experimental setup and to generate experimental data much faster, compared to the data generated within weeks and or months in the climate chamber. Furthermore, they directly allow the access to the degraded layer for further investigations. The experimental setup is shown in Figure 6.2. It consists of an electrically grounded hot plate (comparable to the grounded module frame) set at a constant temperature of 160°C . The voltage was set to be $+1000\text{ V}$. The magnitude of the parameters voltage and temperature were found to have an accelerating effect on the degradation. Unencapsulated mini modules of a total size of $10 \times 10\text{ cm}^2$ as well as glass samples covered with ZnO:B only, were tested on the hotplate regarding their degradation behavior. The mini modules were tested in order to present and discuss the comparability of the results gained on the hot plate and in the climate chamber with large size modules.

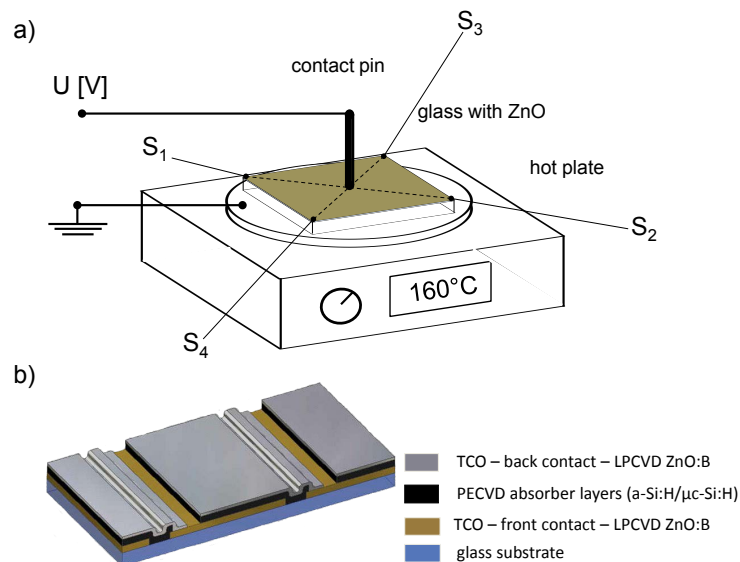


Figure 6.2: (a) Experimental setup for degradation test of TCOs. The hot plate is grounded and the ZnO:B layer on top of the soda-lime glass is set to a fixed potential. (b) Sketch of the monolithic interconnection of the cells in a thin film module.

The glass samples covered with ZnO:B had a square size of $5 \times 5\text{ cm}^2$ and a thickness

of 3.2 mm. The samples were placed on top of the hot plate. The sample side covered with ZnO:B was contacted with a pin; in this configuration, the ZnO:B is the anode and the hot plate is the grounded cathode. Due to the conductivity of ZnO:B, an equipotential surface is formed when a potential is applied to the contact pin. The two electrodes were thus isolated by the glass volume only. To induce anodic degradation, the contact pin was held at a positive potential with respect to the grounded hot plate. After treatment, the ZnO:B sheet resistance was found to be inhomogeneous. Therefore, we evaluated the electrical properties by measuring the resistance across the diagonal of the sample (R_{S1S2} , R_{S2S4}), as indicated in Figure 6.2a by the measure points labeled S1, S2, S3 and S4. The sample was cooled to room temperature before measurement. The measured values for R_{S1S2} and R_{S2S4} were averaged. Furthermore, Hall effect measurements were conducted to determine electron concentration (N_e) and mobility (μ_H). Furthermore, UV-Vis transmittance, IR reflectance as well as Raman effect measurements were conducted.

The mini module tested was based on the micromorph technology, as well as the large size modules tested in the climate chamber. ZnO:B was used as the front and back electrode. This module had 10 cells monolithically interconnected; see Figure 6.2b for visualization. One module cell had a size of $6 \times 66 \text{ mm}^2$. Due to the interconnection, the electrical contact to the front electrode, which was in touch with the glass, was made through the back contact. The degradation treatment was applied to the module for 10 minutes. External quantum efficiency (EQE) and current-voltage (I(V)) measurements were conducted to evaluate the performance of the module before and after the degradation treatment.

6.3 Anodic degradation of a large size module in the climate chamber

Large size modules treated in the way specified above show a drastically changed electric behavior after degradation. In Figure 6.3 the relative module power for a biased und an unbiased module is shown as a function of damp heat duration. The ambience in the climate chamber during the test was set to 85 °C and 85 % relative humidity, according to IEC61646 10.13. The module tested without bias voltage does not show any power degradation until 6000 h, which is six times more than required according to IEC61646 10.13.

In contrast to this, the module tested under the same climate chamber conditions, but biased with 600 V, lost 20 % of its initial power already after about 100 h and roughly 60 % after 200 h test time. Both modules had the same assembling, in terms of front and back glass, transparent conductive oxide (TCO) and micromorph Si absorber. As TCO we used our standard ZnO:B (Std-TCO, uniformly doped during layer growth).

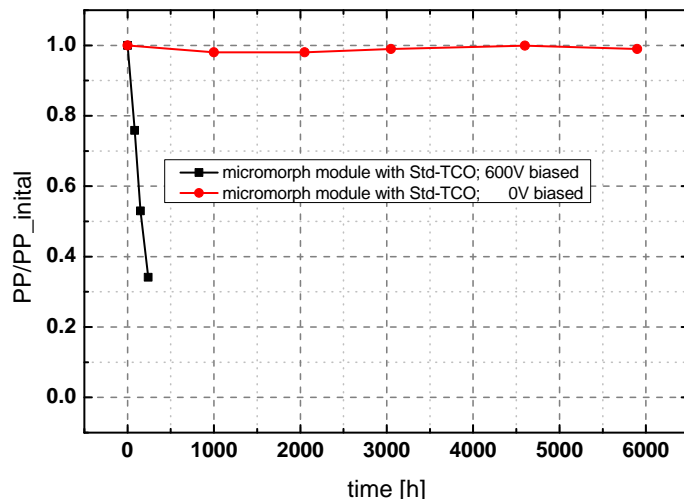


Figure 6.3: At 85°C and 85% r.h. the performances of thin-film silicon solar modules with and without 600 V bias is shown as a function of time.

Further investigations of the module parameters revealed, that the main parameters responsible for the power degradation are FF and R_{oc} (module series resistance, measured under open circuit conditions). The massive power loss of the tested module is correlated to a strong loss in FF which coincides with drastic increase of modules series resistance. The respective behavior is shown in Figure 6.4.

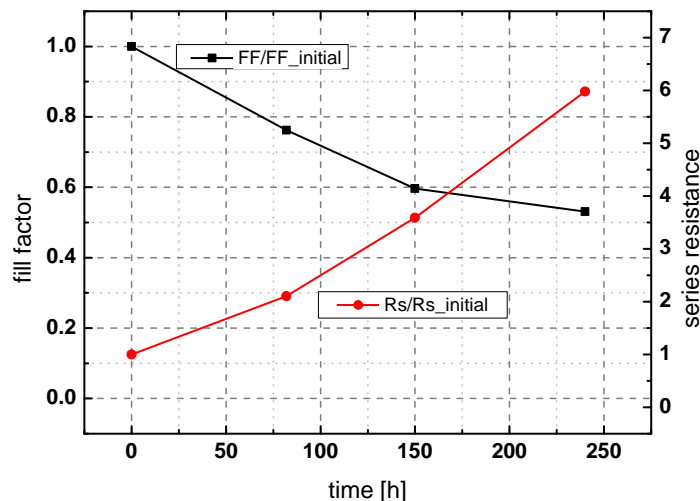


Figure 6.4: Solar Module's fill factor (FF) and series resistance (R_s , resistance measured under open circuit conditions) are shown as a function of time in the climate chamber at 85°C and 85% r.h. and 600 V bias.

As will be identified and discussed later in more detail the increased resistivity of ZnO:B is assumed to be responsible for the observed power degradation. To verify the validity of the hot plate test introduced in Section 6.2, in the following section it will be shown that the effect observed for large size modules in the climate chamber can be observed on an unencapsulated mini module as well, which was subjected to the hot plate treatment.

6.4 Anodic degradation of a unencapsulated mini module on the hot plate

The mini module is treated on the hot plate in accordance to the procedure introduced in Section 6.2. In Figure 6.5a the I(V) characteristics of a small unencapsulated micro-morph module are presented before and after the degradation treatment. Note that the degradation observed is achieved within 10 minutes, compared to the degradation results observed within weeks and month in the climate chamber. The table inset shows the most important I(V) curve parameters and their relative changes. The most significant change occurs for the resistance measured under open-circuit conditions. This resistance is linked to the module's series resistance and may depend on many details. One is the resistivity of the ZnO:B, which is used not only as the front but also as the back electrode (see Figure 6.2b). It is assumed that the resistance increase observed for the single ZnO:B layer, as will be presented in Section 6.5, is responsible for the increase of the series resistance of the module. The series resistance (R_{oc}) of the module grows from about 50 to about 960 Ω .

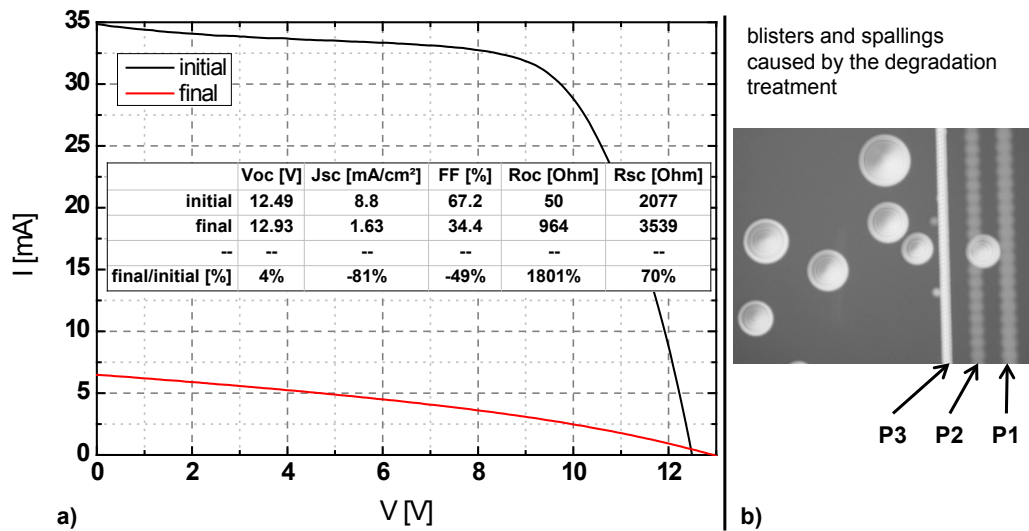


Figure 6.5: (a) I(V) characteristics of a small module based on an a-Si:H and μ c-Si:H silicon tandem solar cell structure before (initial) and after (final) degradation treatment. Here, V_{oc} and R_{oc} are the module voltage and resistance measured under open-circuit conditions, and j_{sc} and R_{sc} are the current and resistance measured under short-circuit conditions. R_{oc} and R_{sc} are correlated with the module's series and parallel resistances, respectively. (b) blisters and spallings near the laser scribing zone (P1, P2 and P3) on a mini module degraded on the hot plate.

As a result a massive drop in the fill factor (FF) is observed as well. This behavior is quite similar to the observations made for the large size modules in the climate chamber. Unexpectedly, the short-circuit current (j_{sc}) strongly decreases from 8.8 to 1.6 mA/cm^2 . Only a slight decrease – if any – was expected due to the shift of the ZnO:B absorption

edge, as shown in Figure 6.9. To further investigate this phenomenon, EQE measurements that yield the module's local spectral response were conducted. The results are presented in Figure 6.6 where the transmittance data presented in Figure 6.9 is also included for comparison.

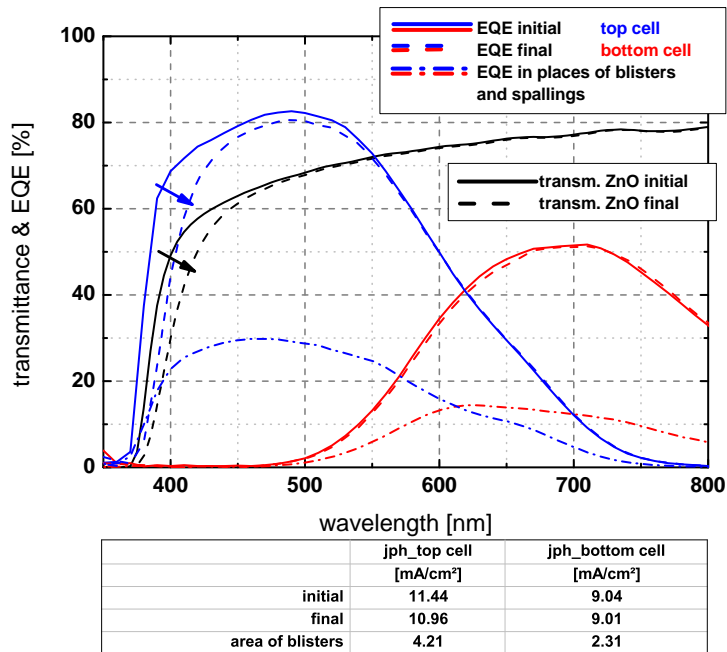


Figure 6.6: External quantum efficiency of a small module measured at different spots on the active module area before and after degradation treatment. The transmittance of ZnO on glass before and after degradation is shown.

As mentioned above, the top-cell EQE in the blue part of the light spectrum decreases after the degradation treatment due to the shift of the absorption edge towards longer wavelengths. Here, a loss of photocurrent of 0.48 mA/cm^2 was measured. This is much less than expected from Figure 6.5a. At this measurement spot the bottom-cell EQE shows no degradation. A closer look at the sample revealed that, due to the non-uniform contact of the sample to the grounded hot plate, the degradation appeared to be inhomogeneously distributed over the active module area. Other EQE spectra were recorded after changing the site of the measurement spot to an area which visually appeared more degraded. Here the photovoltaic layer stack seemed to be detached from the glass surface (bubbles, blisters), see Figure 6.5b. Having a closer look to large size modules treated in the climate chamber, also revealed the appearance of blister. Especially along the edges of the module where the conductive frame (copper tape) is close to the front electrode (ZnO:B). For the mini module, here the EQEs of the top and bottom cells after the degradation treatment decreased to only a third of their initial values. Presumably, the active module area is reduced here due to the presence of spallings and bubbles, and thus the average signal over the beam spot is reduced. Considering the equivalent circuit of an ordinary solar cell (see Figure 2.15), another explanation could be a strong increase of the cell's series resistance caused by the re-

sistivity increase of the ZnO:B front electrode. Due to the locally strongly increased series resistance, the photocurrent is not able to follow the external circuit. The photocurrent is forced to drain off through the local parallel resistance. As a result the low EQE signal shown in Figure 6.6 is measured. As already mentioned in the experimental section that the ZnO:B resistance was found to have a certain inhomogeneity. Together with the explanation given above, the averaging of unaffected module areas with areas of significantly increased series resistance could explain the observed drop of j_{sc} in Figure 6.5a.

6.5 Degradation of samples with ZnO:B on glass only

As one has seen from Section 6.4 the hot plate setup is adequate to achieve similar degradation results for mini modules compared to results gained for large size modules degraded in the climate chamber. In the following it will be further proven that the ZnO:B deposited on the glass and used as front contact is the layer driving the power degradation of the solar module. Electrical and optical properties of glass samples ($5 \times 5 \text{ cm}^2$) covered with ZnO:B only will be discussed before and after degradation treatment on the hot plate.

6.5.1 Electrical changes of glass/ZnO:B samples

The average resistance across the diagonal of the treated samples is shown in Figure 6.7. The ZnO:B was deposited with a constant mass flow rate of DEZ and a varying B_2H_6 rate for different samples. As indicated, the doping ratio (B_2H_6/DEZ) was varied between 0.08 and 0.18. For 10 minutes time a voltage of +1000 V was applied to each sample, as described in Section 6.2. A strong increase of resistance of about 4 orders of magnitude was observed for the sample with a doping ratio of 0.08. The resistance increase is reduced for higher doping ratios. Note that the applied voltage and temperature mainly affects the rate of the degradation process. If no voltage is applied, no reasonable degradation is observed, despite the sample is subjected to the hot plate at 160°C. Details on voltage and temperature variations will not be discussed further in the present work. To the author's knowledge, this phenomenon is previously unrecorded in the literature, even though it is obviously of practical importance for photovoltaic applications.

The resistivity of a polycrystalline semiconductor thin film on top of an isolating substrate is determined by its thickness, density of free charge carriers and their corresponding mobility [69, 115]. In order to discover the reason for the resistance increase, the free charge carrier density and mobility in the ZnO:B film were determined by Hall

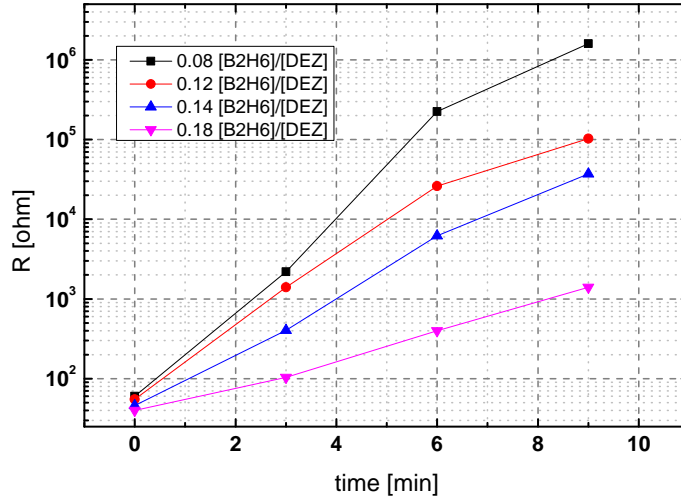


Figure 6.7: Resistance measured across the sample diagonal as a function of treatment time. A voltage of +1000 V was applied. The temperature was set at 160°C. ZnO:B was deposited with a doping ratio (B2H6/DEZ) varying between 0.08 and 0.18. Just for comparison, for the sample with a doping ratio of 0.08, the initial resistance value of 60 ohm (R_{S1S2} , R_{S3S4}) corresponds to a sheet resistance of about 20 ohm/sq (four-point probe setup).

effect measurements. The results for the sample deposited with a doping ratio of 0.08 are summarized in Table 6.1.

Table 6.1: Data derived from Hall effect measurements for the sample with a doping ratio of 0.08 before and after biased hot plate treatment. The film's free charge carrier density (N_e) and mobility (μ_H) are shown. The negative prefix for charge carrier density indicates that the majority carriers are electrons. The ZnO:B layer was treated with an applied voltage of +1000 V for 10 minutes on the hot plate at 160°C.

	N_e [cm^{-3}]	μ_H [cm^2/Vs]
non-degraded ZnO:B sample	$-5.87 \cdot 10^{19}$	29.7
degraded ZnO:B sample (10 min at 1 kV)	$-4.43 \cdot 10^{19}$	1.1

The initial charge carrier density was measured to be $-5.87 \cdot 10^{19} cm^{-3}$ with a mobility of $29.7 cm^2/Vs$. During degradation the free charge carrier density decreased by $1.44 \cdot 10^{19} cm^{-3}$. This induced change is small compared to that measured for the charge carrier mobility. Here, a dramatic drop from 29.7 to 1.1 cm^2/Vs was observed. The drop in mobility seems to be the main driver for the resistance increase.

LPCVD ZnO:B is well studied in the literature [15, 35]. Steinhauser et al. [37] prepared a doping series of ZnO:B films on glass and determined free charge carrier density and mobility. For the free charge carrier density measured for the above sample, they recorded mobilities of between 20 and 30 cm^2/Vs . This is in agreement with the present results of the as-deposited ZnO:B. Although the mobility of free charge carriers is known to depend on their density [35, 69], the relatively small density change observed

in the present work cannot explain the massive drop in mobility (for comparison, see Ref. [37]). Other effects that limit mobility and may be enhanced by the degradation treatment, e.g. phonon or impurity scattering, have to be taken into consideration [31, 116]. As will be discussed later in more detail, for polycrystalline thin films such as our LPCVD ZnO:B, another very important scattering mechanism occurs at grain boundaries. Here, defects may have quite a strong impact on the electrical behaviour. A general review article related to the electrical properties of grain boundaries was published by Greuter et al. [115].

6.5.2 Optical changes of glass/ZnO:B samples

Before discussing the results of optical transmittance, IR reflectance and Raman measurements, some other visual observations will be summarized. Between the grounded hot plate and the ZnO:B, the resulting electric field forces positively charged sodium ions in the glass to move towards the glass surface at the cathode (grounded hot plate). In soda-lime glass, sodium is readily available and its cation is one of the most mobile metallic ions in the glass [117]. Energy dispersive X-ray spectroscopy, conducted in the course of the present work, revealed a remarkable increase in the amount of sodium on the glass surface after degradation (not shown here). During degradation treatment, a possible reaction at the cathode is the reduction of positively charged sodium ions according to Equation 6.1. Furthermore, the sodium on the glass surface is surrounded by humid air during and after the degradation procedure, so that it is likely that the sodium reacts with water according to Equation 6.2. The pH value at the glass surface is an indicator of such a reaction; we observed that the pH value was in the alkaline range between 7 and 10.

In places on the anode (ZnO:B) surface, circular spallings were found after degradation. This coincides with the observation of blisters and spallings for the mini module and for the large size modules along their edges. The spallings can be seen in Figure 6.8. Here, the scanning electron microscopy (SEM) images revealed that the typical diameter of the spallings was about $100\ \mu\text{m}$ or more. As one can see further, the ZnO:B layer peeled off completely from the glass substrate. The distribution of spallings was found to be uniform for the ZnO:B covered glass samples, but might depend on the realized contact between the glass and the grounded hot plate (e.g., an air gap might influence the experiment). Also temperature gradients or the temperature profile might impact the result.

Furthermore, a yellowing of the sample was observed during the degradation treatment. In the literature such coloration is attributed to the presence of oxygen vacancies in ZnO [40]. The oxygen vacancies create a band of defects within the bandgap just above the valence band maximum. This in turn leads to defect-induced light absorption, causing a shift of the ZnO absorption edge towards longer wavelengths which in

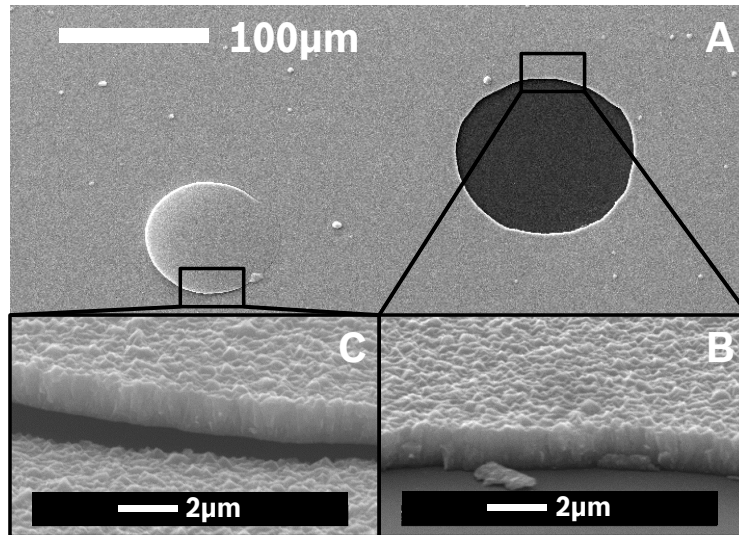


Figure 6.8: Scanning electron microscopy (SEM) images of a ZnO:B surface after an anodic degradation treatment. In places the ZnO:B film possesses circular spallings. B and C are magnifications from area A.

turn causes the yellow appearance. In Figure 6.9 the transmittance is shown for a ZnO:B sample deposited with a doping ratio of 0.08 before and after 10 minutes of degradation treatment. For a better visualization of relevant changes, the x-axis is scaled from 350 to 450 nm and from 500 to 2500 nm. Here, the absorption edge and the influence of free charge carriers in the IR can be evaluated.

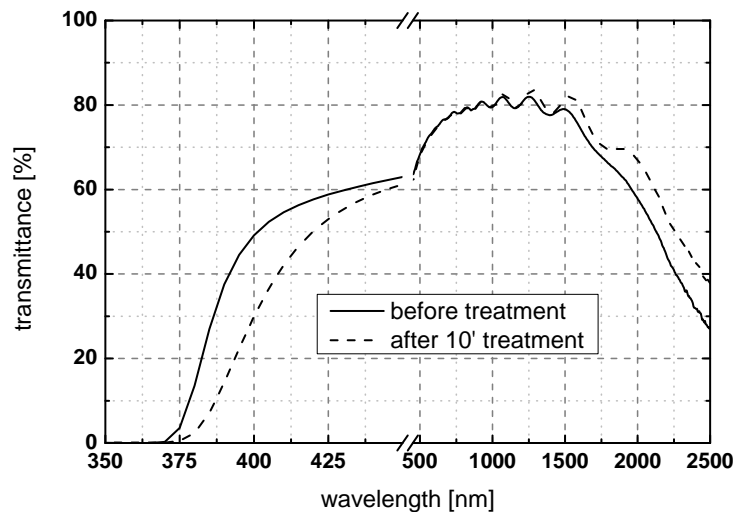


Figure 6.9: Transmittance spectra of a 3.2-mm-thick soda-lime glass substrate covered with ZnO:B before and after 10 minutes of degradation treatment. The ZnO:B was deposited using a doping ratio of 0.08.

In the spectral range between 350 and 450 nm, the absorption edge of ZnO shifted towards longer wavelengths when the degradation treatment was applied. This is in agreement with the yellowing discussed above. For the improved transmission in the spectral range between 1500 and 2500 nm, one explanation could be the optical plasma mode oscillations of free electrons. This behaviour is treated theoretically by Drude's

theory of a free electron gas. It has been applied by many authors to interpret the IR response of TCOs [37, 45, 118–120]. The electron concentration and optical mobility (μ_{opt}) are parameters that can be derived from that theory. Here, due to a decrease of electron concentration, the IR response of free electrons in the conduction band of ZnO:B shifts towards longer wavelengths. This causes less absorption and thus higher transmittance in the spectral range between 1500 and 2500 nm observed in Figure 6.9. Such an argument seems to be valid, since a decrease of electron concentration is indicated by Hall effect measurements, shown in Table 6.1.

Another explanation for the increase of transmittance could be an increase of μ_{opt} . On the one hand an increase of μ_{opt} is in contradiction to the observed massive decrease of Hall mobility (see Table 6.1). But on the other hand this would cause a less pronounced spectral response of free electrons in the spectral range between 1500 and 2500 nm, and thus lead to higher transmittance. Steinhauser et al. [35,37] distinguished between μ_{opt} and μ_H . They stated that under high frequency excitation electrons are scattered by intra-grain mechanisms (e.g., by ionised impurities or phonons), whereas electrons excited by a constant electric field, as during Hall effect measurements, might be strongly influenced by scattering mechanisms located at grain boundaries. With reference to that argument and with regard to the present results, the following is concluded so far: Even if μ_{opt} is assumed to have not changed (instead of increasing), the cause of the dramatic drop of μ_H is presumably correlated with a scattering mechanism located at grain boundaries. To further support or to eliminate this hypothesis IR reflectance measurements were conducted, in order to determine the optical mobility. They will be analyzed with the optical model introduced in Section 2.1.5. The results of this analysis will be discussed in the following.

IR reflectance measurements

In Figure 6.10 the IR reflectance spectra, determined experimentally, in the spectral range between 1.2 and 25 μm of a non-degraded and a degraded ZnO:B film (doping ratio $[B_2H_6]/[DEZ]=0.08$) deposited on soda-lime glass are shown as dotted lines. Furthermore, the respective simulated reflectance data are displayed. For better visualisation the x-axis is scaled from 1.2 to 3 μm and from 3 to 25 μm . In the spectral range between 1.2 and 3 μm the ZnO:B film is transparent. Here, due to multiple reflections at the interfaces glass/ZnO:B and ZnO:B/air, interference fringes can be observed. In the spectral range of 3 to 25 μm the interaction of incoming photons with free electrons and phonons can be observed. The interaction with phonons becomes dominant for wavelengths above 17 μm , whereas the interaction with free electrons, which is characterized by the sudden increase of reflection, is typically observed below 5 μm [46]. This usually depends on the concentration of free electrons.

A very important feature for the following discussion is located at about 17 μm . The

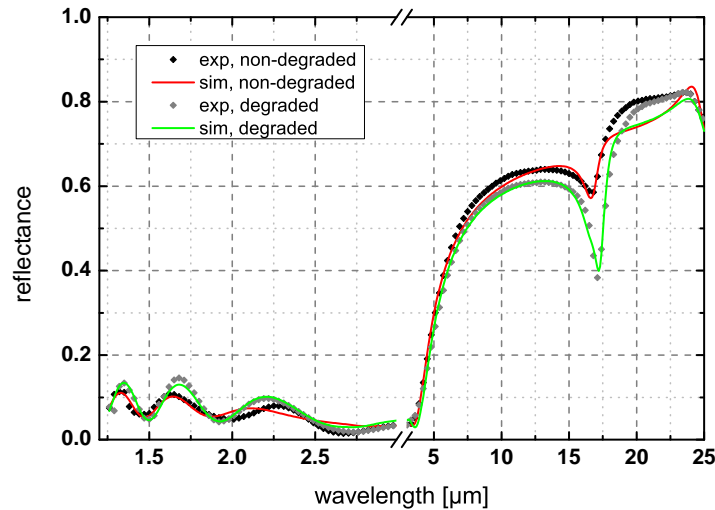


Figure 6.10: IR reflectance measurements generated experimentally (exp) and simulated (sim) of a degraded and a non-degraded sample (ZnO:B on soda-lime glass). The degraded sample was treated for about 10 minutes on the hotplate according to the procedure mentioned in Section 6.2

feature was recently explained by Prunici et al. [46]. Its origin was explained in Section 2.1.5, discussing the dielectric function (DF) of a polycrystalline ZnO:B (poly. ZnO:B) film. The shape and position of the dip in the reflection signal depends mainly on the electron concentration of the grain bulk and boundary material and on the volume fraction f_{bnd} of the grain boundary material. These parameters determine the DF of the polycrystalline ZnO:B film, which can be calculated according to Equation 2.8. They are adjusted during the fitting procedure, matching the simulated and measured reflectance. The most obvious changes observed in Figure 6.10 for the degraded sample are the increase of the dip located at about $17\ \mu\text{m}$ and the increased magnitude of interference fringes in the transparent spectral range between 1.2 and $3\ \mu\text{m}$. As can be seen, both features could be simulated sufficiently.

In Figure 6.11 a sketch of the layer stacks used for the simulation of the reflectance spectra (Figure 6.10) for the non-degraded and the degraded sample are shown. The derived thickness for each fitted optical layer is displayed. Despite the difference in the optical layer model, the total layer thicknesses for the non-degraded and the degraded ZnO:B sample is calculated to be similar with about $1760\ \text{nm}$. Whereas for the non-degraded sample a main polycrystalline ZnO:B layer on a glass substrate in combination with a top surface layer is used, the degraded sample is simulated using an additional layer (poly. ZnO:B*) at the glass/ZnO:B interface. As will be discussed later in more detail, the layer possesses a higher refractive index in the transparent spectral range compared to the $1483\ \text{nm}$ thick polycrystalline ZnO:B layer above. The layer is required to adjust the increased magnitude of the interference fringes for the IR reflectance spectrum of the degraded sample. Its thickness was fitted to be $166\ \text{nm}$. Note that in the case where the additional interface layer is introduced, the thickness

of the main polycrystalline ZnO:B layer is reduced, so that the total layer thickness is maintained.

The top surface layer was treated according to the effective medium theory (EMT) of Bruggeman [49]. For this commonly used approach, a volume fraction of 50 % of the DF of the polycrystalline ZnO:B material below the top surface layer was mixed with a volume fraction of 50 % of the DF of void. The thickness of the surface roughness was fitted to be 117 and 113 nm for the non-degraded and degraded sample, respectively. We conclude that the surface roughness has not changed during anodic degradation.

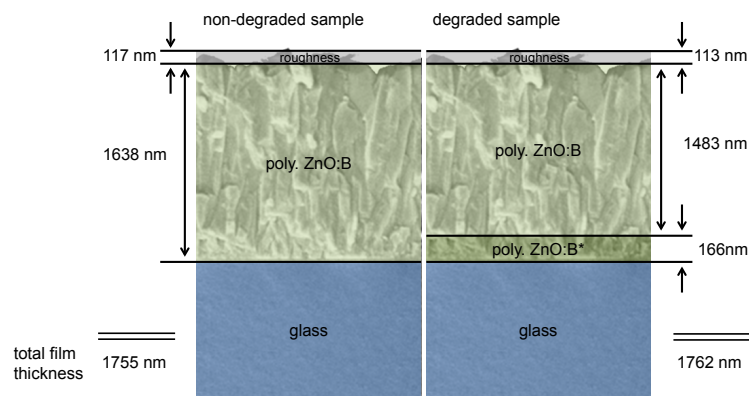


Figure 6.11: Modeled layer stacks used for simulating the IR reflectance spectra of the non-degraded and degraded sample. Beside the used layer stacks, the corresponding fitted thicknesses are shown. "poly. ZnO*" is assigned to a polycrystalline ZnO layer with higher refractive index used in the optical model for the degraded sample.

Table 6.2 summarizes all other parameters used for simulating the IR reflectance spectra, shown in Figure 6.10. As presented, the high frequency constant (ϵ_∞) was set to be 3.8 and the effective mass of the electrons was set to be 0.3 [11] p. 91. For the contribution of phonons only the damping constant (Γ_{ph_blk}) was fitted for both the grain bulk and boundary material. Γ_{ph_bnd} was assumed to be equal to Γ_{ph_blk} . The characteristic frequencies of the transversal and longitudinal optical phonon modes, ω_{LO} and ω_{TO} were set to be 577 and 406 cm^{-1} , respectively [46]. Other optical parameters shown in Table 6.2 were fitted in order to match simulated and measured reflectance spectra.

For the non-degraded sample and its grain bulk ZnO:B material a plasma mode frequency (ω_{N_blk}) of 2501 cm^{-1} was found. This can be recalculated into unit of wavelength. Here, λ_{N_blk} was calculated to be 4 μm , which typically coincides with the spectral position of the onset of high reflection, as shown in Figure 6.10. According to Equation 2.10 and 2.11 and the derived fit parameters, one can calculate electron concentration and optical mobility [46].

As shown in Table 6.2, for the ZnO:B grain bulk material of the non-degraded sample, the electron concentration and mobility determined by IR reflectance measurement and Hall effect measurement are of the same order of magnitude. μ_{opt} was found to be

Table 6.2: Summary and comparison of fit parameters used for simulating the reflectance data presented in Figure 6.10. Further fit parameters used both for non-degraded and degraded samples are $\epsilon_\infty = 3.8$, $\omega_{LO} = 577 [cm^{-1}]$ and $\omega_{TO} = 406 [cm^{-1}]$. Note that $\omega_N = \omega_P/\sqrt{\epsilon_\infty}$ and the effective mass of electrons is assumed to be 0.3. The subscripts *_blk* and *_bnd* refer to grain bulk and boundary material, respectively. For comparison, parameters from Hall-Effect measurements for the samples before and after degradation are included.

non-degraded sample				degraded sample			
grain bulk material				grain bulk material			
$\omega_{N_blk} [cm^{-1}]$	2501	$N_e [cm^{-3}]$	$7.42 \cdot 10^{19}$	$\omega_{N_blk} [cm^{-1}]$	2436	$N_e [cm^{-3}]$	$7.04 \cdot 10^{19}$
$\lambda_{N_blk} [\mu m]$	4.0			$\lambda_{N_blk} [\mu m]$	4.1		
$\Gamma_{pl_blk} [cm^{-1}]$	1016	$\mu_{opt} [cm^2/Vs]$	32.8	$\Gamma_{pl_blk} [cm^{-1}]$	985	$\mu_{opt} [cm^2/Vs]$	33.9
$\Gamma_{ph_blk} [cm^{-1}]$	15.48			$\Gamma_{ph_blk} [cm^{-1}]$	24.45		
grain boundary material				grain boundary material			
$\omega_{N_bnd} [cm^{-1}]$	234	$N_e [cm^{-3}]$	$6.50 \cdot 10^{17}$	$\omega_{N_bnd} [cm^{-1}]$	–	$N_e [cm^{-3}]$	–
$\lambda_{N_bnd} [\mu m]$	42.7			$\Gamma_{pl_bnd} [cm^{-1}]$	–		
$\Gamma_{pl_bnd} [cm^{-1}]$	455			$\Gamma_{ph_bnd} [cm^{-1}]$	24.45		
$\Gamma_{ph_bnd} [cm^{-1}]$	15.48			$f_{bnd} [\%]$	8		
$f_{bnd} [\%]$	3						
Hall effect data measured							
	$N_e [cm^{-3}]$		$5.87 \cdot 10^{19}$		$N_e [cm^{-3}]$		$4.43 \cdot 10^{19}$
	$\mu_H [cm^2/Vs]$		29.7		$\mu_H [cm^2/Vs]$		1.1

slightly higher than μ_H . Although other authors do not distinguish between grain bulk and boundary materials this result is in agreement to results reported for as-deposited ZnO:B samples [37, 45]. This can be explained by the fact that the optical response is typically dominated by the high volume fraction of the grain bulk material in the spectral range between 5 and 15 μm . In the present case, for the non-degraded ZnO:B sample the volume fraction of the grain bulk material (f_{blk}) was determined to be 97%, and 3% for the grain boundary material.

Whereas the difference between the electron concentrations determined optically and from Hall effect measurements can be explained by our choice of ϵ_∞ and m^* , the difference in electron mobility significantly depends on the optical damping constant (Γ_{pl}) and on the conditions at the grain boundaries in the polycrystalline ZnO:B film. The difference in mobility is linked to the different excitation mechanisms on which the measurement methods are based. Whereas during optical excitation electrons are predominantly displaced within individual ZnO grains due to the high-frequency electric field, the constant electric field during Hall effect measurements causes electrons to cross numerous grain boundaries.

A huge discrepancy was found for the degraded sample. Here, the grain bulk material still possesses an optical mobility of 34 cm^2/Vs , whereas the mobility determined from Hall effect measurements dropped from initially 29.7 down to 1.1 cm^2/Vs . This is a strong indication for a high defect concentration at ZnO grain boundaries, causing a high scattering probability for electrons and thus, highly resistive layer properties. These defects are known to trap electrons from the material near the grain boundary and to create a potential barrier at the grain/grain interfaces. Electrons have to

overcome the potential or to tunnel through this interface in order to contribute to a DC current. As a result μ_H is reduced whereas μ_{opt} is maintained, since the majority of electrons optically excited are within grains and not scattered by defect-rich grain boundaries.

Evidence for trapped electrons can be found in the DF fitting parameters of the grain boundary material. Here, the electron concentration was found to be $6.5 \cdot 10^{17} \text{ cm}^{-3}$ for the non-degraded ZnO:B sample, much less than the value of $7.49 \cdot 10^{19} \text{ cm}^{-3}$ found for the grain bulk material. Note that the accuracy of the electron concentration determined for the grain boundary material presumably is limited. The value was derived from the fitted plasma mode frequency $\omega_{N_bnd} = 234 \text{ cm}^{-1}$ (approximately $42 \mu\text{m}$) given in Table 6.2. This is beyond the spectral range investigated but better fit results were obtained, considering a small amount of electrons than neglecting them. Furthermore, because the plasma mode frequency for the grain boundary material is close to the phonon resonances (ω_{LO} , ω_{TO}), the plasma mode oscillation in the grain boundary material might interfere with the phonon resonance. As a result the fitted parameters for the grain boundary material may be inaccurate, and we thus abstained from further interpretation of the damping constant related to the optical mobility.

For the degraded sample, the best fit results were obtained by neglecting free electrons in the grain boundary material. Such an approach may be valid since a higher defect concentration at the grain boundaries for the degraded than for the non-degraded sample is assumed, thus causing a higher number of trapped electrons at the ZnO grain interfaces. This in turn would cause a decrease in electron concentration in the ZnO grain boundary material and a further decrease of ω_{N_bnd} . Furthermore, a decrease in electron concentration in the grain bulk material from $7.42 \cdot 10^{19} \text{ cm}^{-3}$ to $7.04 \cdot 10^{19} \text{ cm}^{-3}$ was determined optically for the degraded ZnO:B film. This decrease was confirmed by Hall effect measurements and further confirms an increased electron trap density at ZnO:B grain boundaries.

In Figure 6.12 the modelled refractive indices and extinction coefficients, which were derived from the EMT approach, are shown for non-degraded and degraded polycrystalline ZnO:B layers. Furthermore, the optical constants for the grain bulk and boundary material used in the EMT approach for the non-degraded sample are presented. The optical constants for the degraded grain bulk and boundary materials are omitted for clarity. They are visually similar to the optical constants of the non-degraded ZnO grain bulk and boundary materials. For the grain bulk and boundary materials, the major difference in n and k is caused by the low electron concentration of the grain boundary material compared to the grain bulk material. Due to the low electron concentration the plasma mode frequency (ω_{N_bnd}) is in far IR spectral range. As a result, the onset of increased k values in the IR spectral range is correlated with the phonon resonance for wavelengths above $15 \mu\text{m}$. For comparison see the extinction coefficients in Figure 6.12 (dashed-dotted and dashed lines).

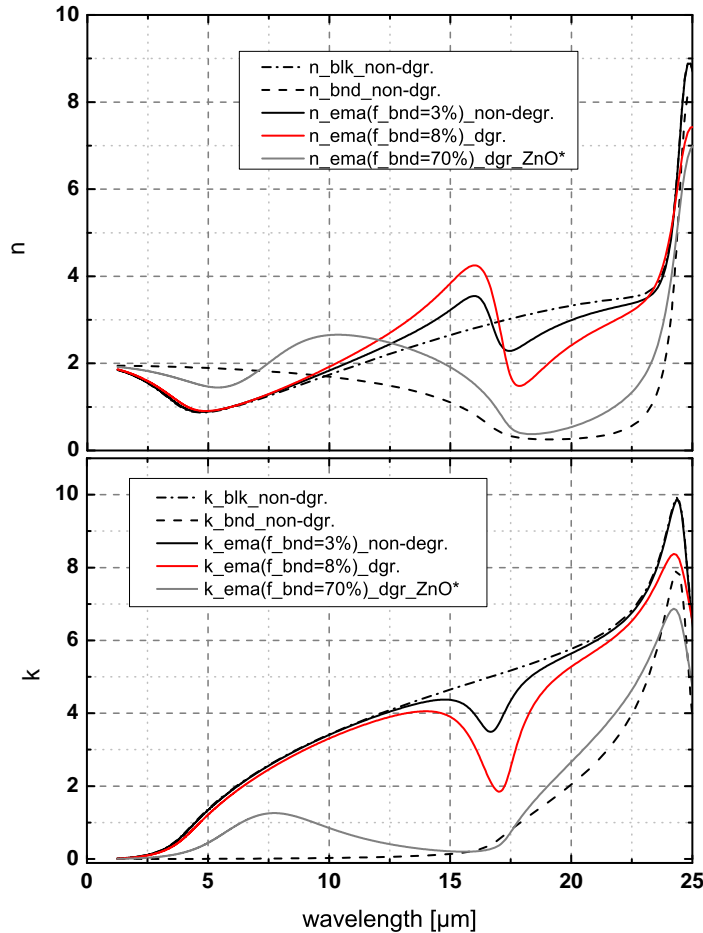


Figure 6.12: Refractive index (n) and extinction coefficient (k) for non-degraded (non-dgr.), degraded (dgr.) ZnO:B layers. Also shown are n & k for the ZnO: interface layer at the glass/ZnO:B for the degraded sample ("dgr_ZnO*"). The DFs were calculated according to the parameters presented in Table 6.2

As already mentioned, only the introduction of the EMT approach yields sufficient simulation results for the polycrystalline ZnO:B layers. As revealed by our fitting, significant changes in the optical constants for the polycrystalline ZnO:B film are induced upon degradation; see Figure 6.12 solid lines. In this model, the volume fraction of the grain boundary material (f_{bnd}) is the major fitting parameter. The higher f_{bnd} , the more pronounced the feature located at around $17 \mu m$. For comparison of the effect of volume fraction, see the reflectance spectra in Figure 6.10 and the corresponding optical constants in Figure 6.12. As presented in Table 6.2, f_{bnd} increases from 3 initially to 8% after degradation. A higher volume fraction can also be interpreted as a wider depletion zone at ZnO:B grain boundaries, consistent with our discussion above.

For the polycrystalline interface layer (poly. ZnO:B*) the optical constants for the degraded ZnO grain bulk and boundary material were used together with the Maxwell-Garnett approach. Instead of 8%, f_{bnd} was fitted to be 70%. The resulting optical constants are shown in Figure 6.12 and are labeled as "dgr_ZnO*". The optical con-

stants show a marked difference compared to those of the non-degraded and degraded ZnO:B material, which is caused by the high volume fraction (f_{bnd}). Note that an individual parameterization of the interface layer is challenging. The reflectance spectrum in Figure 6.10 is sensitive to the interface layer only at short wavelengths, for which the ZnO:B is transparent. From the extinction coefficient presented in Figure 6.12, one can estimate the wavelength-dependent optical penetration depth for the polycrystalline ZnO:B layer above the interface layer. Whereas the penetration depth for wavelengths above $5\ \mu m$ is estimated to be below $500\ nm$, the penetration depth for wavelengths below $5\ \mu m$ exceeds $3\ \mu m$, so that the ZnO:B becomes optically transparent for shorter wavelengths. Thus, the optical constants for the interface layer ($d_{gr_ZnO} : B^*$) are valid only for wavelengths below $5\ \mu m$. For wavelengths above $5\ \mu m$, the glass/ZnO interface is not sensed, due to the reduced penetration depth of the light. However for the optical model of the degraded ZnO:B sample the interface layer with adjusted optical constants is required in order to match the increased magnitude of interference fringes in the transparent spectral range, see Figure 6.10.

For a given electron concentration and a certain electron-trapping defect concentration at ZnO:B grain boundaries, a depletion region of a certain width is created at the grain boundaries. The width is assumed to be independent of the grain size. Thus, f_{bnd} scales with the total grain size: The smaller the grains the higher f_{bnd} . It is well known that LPCVD ZnO:B starts to grow with small grains that then increases in size [16,29]. In Figure 6.13, transmission electron (TEM) and scanning electron (SEM) microscopy records are presented for the non-degraded and the degraded sample. For both samples an interface layer next to the glass substrate, consisting of smaller grains, can be recognized. Note that for optical model of the non-degraded sample this interface layer is neglected, see Figure 6.11. This is justified by the small f_{bnd} (smaller depletion width) for the interface layer in the non-degraded case. As can be seen in Figure 6.12, the refractive index does not vary much for low volume fractions (smaller than 10%). Thus, the interface layer does not differ optically from the polycrystalline ZnO:B layer above it in the transparent spectral range. As a result, both layers can be modeled as a single layer.

Another explanation for an interface layer with higher refractive index in the degraded case could be related to stoichiometry changes or the accumulation of positively charged zinc interstitials at the glass/ZnO:B interface. However, energy dispersive X-ray analysis (EDX) on the samples (presented in Figure 6.13) revealed no changes. Presumably the changes induced are below the detection limits of the measurement. Furthermore, it is not clear yet whether these stoichiometry changes introduce the required changes in n and k .

In Figure 6.13 another interesting detail was revealed. In contrast to the non-degraded sample the degraded ZnO:B film features micro voids at the ZnO:B grain boundaries. These voids were observed for both SEM and TEM images. The origin

is not yet clear, but their presence further supports the hypothesis of the creation of defects at grain boundaries during the degradation treatment.

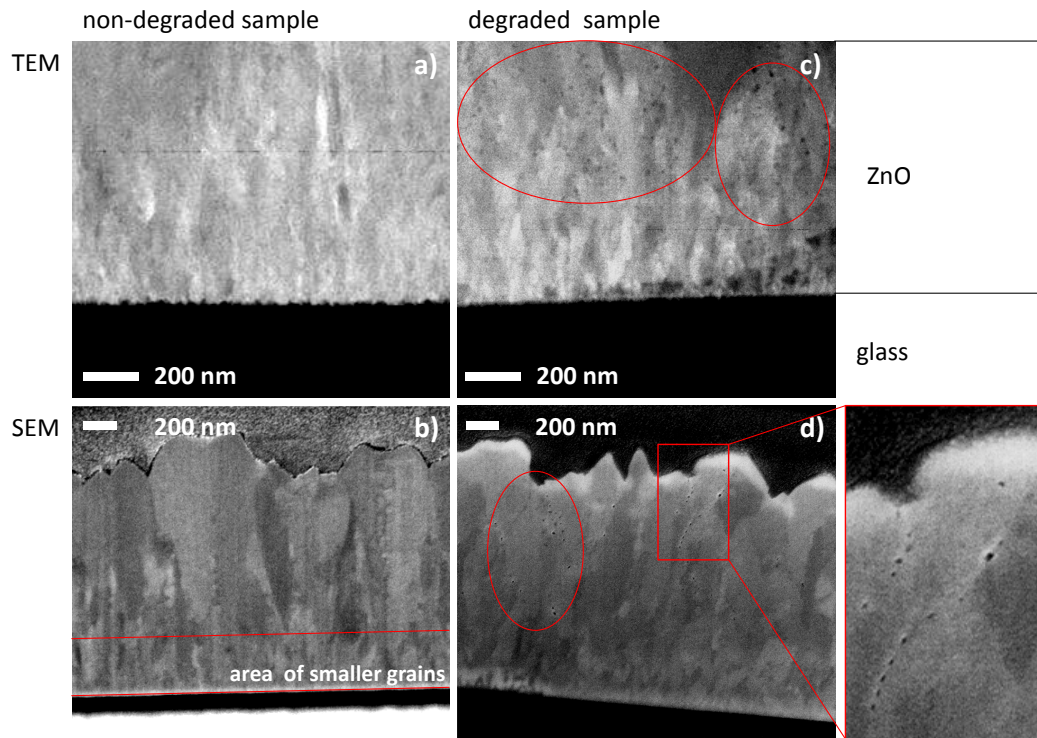


Figure 6.13: Transmission electron (TEM) and scanning electron (SEM) microscopy images of a non-degraded and degraded ZnO film deposited on soda-lime glass. Micro voids at ZnO grain boundaries after degradation are highlighted.

A last detail can be discussed for Figure 6.9. In the spectral range between 500 and 2500 nm we previously discussed both a decreased electron concentration and an assumed higher optical mobility as reasons for the higher transmission, observed after degradation. A decreased electron concentration from initially $7.42 \cdot 10^{19}$ to $7.04 \cdot 10^{19} cm^{-3}$ derived from optical measurements could be confirmed, even though the observed change is much greater for the change derived from Hall effect measurements, see Table 6.2. The optical mobility of the grain bulk material was determined to be constant at a value of about $33 cm^2/Vs$. The optical parameter that changed most was the volume fraction, f_{bnd} . The observed rise from 3 to 8% indicates that more material of the grain boundary material averages with the grain bulk material. As presented the grain boundary material has a much lower electron concentration, which coincides with lower absorption losses in the IR spectral range. As result of both a lower electron concentration and a higher volume fraction, f_{bnd} , the transmission rises.

Raman effect measurements

As mentioned in the beginning of Section 6.5.2, the degraded samples possess a yellow coloration, which is not caused by color centers created somewhere in the ZnO:B film.

Instead, in the literature such coloration is attributed to the presence of oxygen vacancies in the ZnO material [40]. The oxygen vacancies create a band of defects just above the valence band maximum within the band gap. This in turn leads to defect induced light absorption causing a shift of the ZnO absorption edge towards longer wavelengths which in turn causes the yellow appearance. This was discussed for Figure 6.9.

To further strengthen the hypothesis of creation of oxygen vacancies in the ZnO:B film during degradation, we utilized Raman effect measurements. Here, intrinsic defects may affect the material specific Raman response. LPCVD ZnO:B is known to grow with the crystallographic structure of wurtzite, which has hexagonal lattice structure. The lattice of ZnO possesses the symmetry of the C_{6v}^4 space group. The optical phonon modes at the Γ -point of the Brillouin zone are termed A_1 , B_1 , E_1 and E_2 . A_1 and E_1 are polar modes and split into transversal (TO) and longitudinal (LO) phonon modes with different frequencies. Both are Raman and IR active [11, 121, 122]. During the present investigation of the non-degraded and degraded polycrystalline ZnO:B each of them were observed, except for the B_1 mode, which is known to be a silent mode. In order to discuss the change observed for the Raman spectra between the non-degraded and degraded sample, we subtracted the spectra gained before from the one measured after degradation. The results of this calculation and analysis are presented in Figure 6.14.

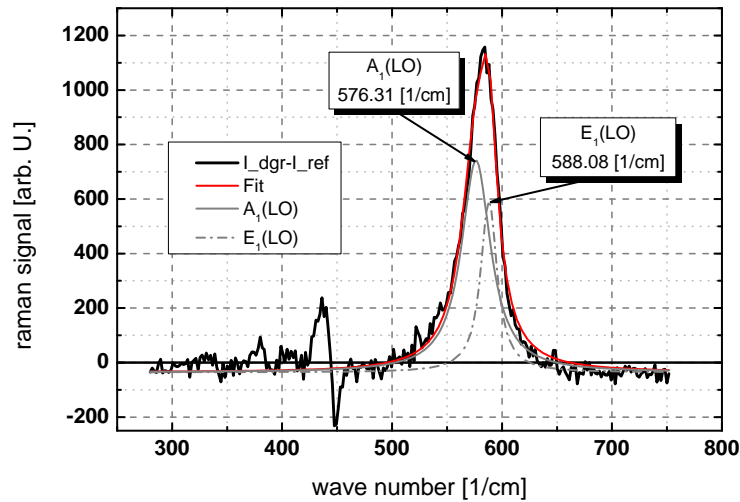


Figure 6.14: The change between the degraded sample and the non-degraded one in the Raman signal is presented. The signal was calculated by subtraction of the non-degraded signal off the degraded one. The signal was fitted using two functions with a Lorentzian profile.

Note that the data presented in Figure 6.14 yielded zero except for the range of wave numbers between 500 and 650 cm^{-1} . This indicates that only here a change for the sample after degradation was observed. The positive amplitude points out that the Raman signal after degradation was increased. In the range between 500 and 650 cm^{-1} for ZnO with wurtzite structure it is known to observe the longitudinal optical

vibration modes of A_1 and E_1 . To determine the position of the respective resonant wave numbers, two Lorentzian peak functions in order to simulate the measured Raman signal in Figure 6.14, were utilized. For $A_1(LO)$ and $E_1(LO)$ values of 576.31 and 588.01 cm^{-1} were found, respectively. This is in good agreement to values reported in the literature and identifies both modes accurately, see Ref. [11] p. 93. In the literature the change of the intensity of these modes is reported to be sensitive to intrinsic defects such as oxygen vacancies or zinc interstitials [123–125]. Šćepanović et al. observed a beige/yellow coloration of the ZnO powder they investigated and attributed this change to the presence of oxygen vacancies as dominant intrinsic defect [125]. Following these interpretations confirms the argumentation of Figure 6.9, where the shift of absorption edge was related to the creation of oxygen vacancies.

6.6 The glass substrate as a source of oxygen during degradation treatment

As will be discussed later in more detail, oxygen is suspected to be responsible for some of our observations. Since it is difficult to measure a small change in oxygen concentration in an oxygen-rich environment (in ZnO:B), the following experiment was conducted. On a standard soda-lime glass substrate we deposited a μc -Si:H layer followed by an a-Si:H cap layer by plasma-enhanced chemical vapour deposition (PECVD). Finally, a ZnO:B layer was deposited to form an electrical contact to the silicon layer stack (and not necessarily to study its degradation). The μc -Si:H was deposited in a regime of high Raman crystallinity, thus yielding porous μc -Si:H material. This layer was intended to act as a gettering material, incorporating the species escaping the glass during degradation. The a-Si:H layer was intended to protect the porous μc -Si:H film from initial oxidation, since the samples were handled in a normal environment before ZnO:B deposition. This sample was treated according to the hot plate degradation treatment, introduced in Section 6.2. Note, that the reference sample was heated on the hot plate, but without applied voltage. The treated sample and reference sample were analysed by secondary ion mass spectroscopy (SIMS) to study the species incorporated from the glass. The results of SIMS analysis are shown in Figure 6.15.

In Figure 6.15, we see a depth profile for the mass number to charge ratio of 60, measured from the ZnO:B side to the glass substrate for the treated and the untreated reference sample. The detector was set to sense negatively charged ions. Cesium was used as primary ion source. Due to the obvious presence of considerable amounts of silicon and oxygen, we observe a certain amount of singly negatively charged silicon dioxide molecules (SiO_2^-) on this channel. We assume that this signal is representative of the amount of oxygen available not only in the glass, but also in the μc -Si:H getter material deposited directly on the glass substrate. Here, a chemical reaction of Si and O

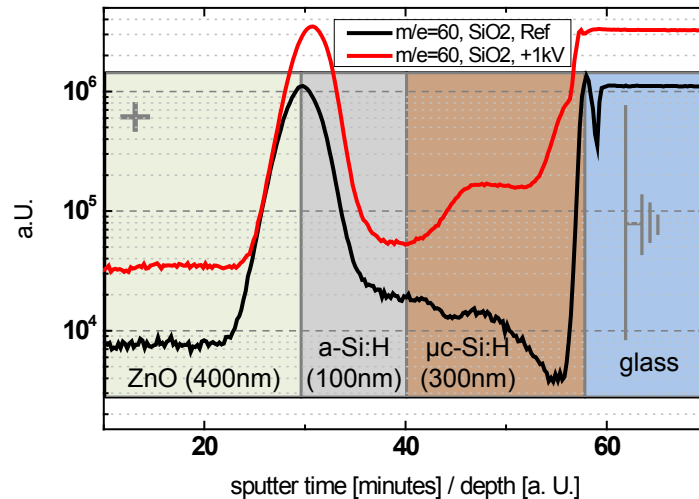


Figure 6.15: SIMS intensity of the ratio $m/e=60$. A layer stack of μc -Si:H (thickness of about 300 nm) and a-Si:H (thickness of about 100 nm) followed by a film of ZnO:B (thickness of about 400 nm) was deposited on a glass substrate. For reference sample (heat treatment on the hot plate, only) and degraded sample (+1000 V applied for 10 min at 160°C) secondary ion mass spectroscopy (SIMS) measurements were performed in order to study the transport of oxygen from the glass into the μc -Si:H getter material.

forming SiO_x is likely. As one sees in Figure 6.15, the a-Si:H cap layer well protects the μc -Si:H from pre-oxidation while handling the sample in a normal environment before ZnO:B deposition. A noticeable difference in line shape at the glass/ μc -Si:H interface was found for the sample treated with +1000 V compared to the reference sample. Here, a difference in signal strength of about 2 orders of magnitude was observed. This indicates a considerable (but not precisely quantified) increase in the amount of oxygen in the μc -Si:H getter material. Furthermore, during anodic degradation, the glass is identified as the source of the oxygen-containing species and, when ZnO:B is deposited directly on glass, these species likely influence the grain boundary properties of the ZnO:B.

6.7 Model of anodic degradation of ZnO:B at the glass/ZnO:B interface

As one has seen from the previous sections, the increase of ZnO:B resistivity, caused by anodic degradation, influences the power output of both mini modules and large size modules. It is suspected that an effect located at ZnO:B grain boundaries is the root cause for the resistance increase of the polycrystalline ZnO:B. Here, when the treatment is applied, the defect density increases. These defects trap electrons from the bulk zinc oxide near grain boundaries, leaving behind an unscreened density of positively charged ions, singly or doubly positively charged interstitial zinc ions, for example. In most

cases such ions are fixed within the zinc oxide and their density within the space charge regions – and thus near the grain boundaries – increases. On the other hand negatively charged defects at the grain boundaries cause a potential barrier. Electrons have to overcome or tunnel through this barrier in order to allow a DC current to pass the defective grain boundary. Besides thermionic emission, where electrons have enough thermal energy to overcome the barrier, the tunneling of electrons through the barrier is one of the most important mechanisms of conduction in polycrystalline zinc oxide films [126–129], especially for devices such as varistors [130–133] and gas sensors [134]. For all applications the grain boundary conditions are thus responsible for the electrical performance of the polycrystalline zinc oxide used. The validity of this working hypothesis can be established by discussing the results of Figure 6.7 in more detail. As already mentioned, a higher doping ratio lowers the resistance increase during degradation. This can be explained by the reduced barrier width and height at grain boundaries, caused by a higher concentration of electrons. For comparison see Equations 2.3 and 2.4. The thinner the barrier, the higher the probability the electrons have to tunnel through the barrier formed at the ZnO:B grain boundaries.

In the literature mentioned in the paragraph above one can find numerous examples in which chemisorbed oxygen at grain boundaries is discussed as the main driver of observed changes in resistivity. However, water incorporated at grain boundaries was also observed to increase the trap density, leading to higher resistivity [38, 135]. For ZnO:B deposited by chemical vapor deposition methods, discussions of water at grain boundaries can be found in [35, 37, 128, 136]. Steinhauser et al. [35, 37, 38] explicitly applied the above-mentioned theory of conduction to LPCVD ZnO:B, the same material discussed in the present work. It is suspected that in the present case oxygen is responsible for an increased trap density at the ZnO:B grain boundaries, as evidence was found for oxygen migration during the degradation process, see Section 6.6. In the following we describe possible mechanisms of ionic and electronic conduction in the glass which we assume to be responsible for the degradation.

Two cases are distinguished. In the first case (I) the degradation current (the current through the sample when a bias voltage is applied) decays rapidly after the degradation process is initialized. The second case (II), which coincides with the present observations for ZnO:B deposited on soda-lime glass, assumes a stable degradation current. In Figure 6.16 a modified SEM image illustrates the conditions under the anode (ZnO:B). Here, in region "A" we assume that when the voltage is applied during the degradation treatment, negatively charged oxygen species, if available in the glass, are forced to move toward, the glass/ZnO:B interface while positively charged sodium ions move away from the glass/ZnO:B interface. Evidence for this phenomena can be found in the literature regarding the physics of anodic bonding or thermal poling [137–144]. A general review of anodic bonding is given by Knowles et al. [145]. In soda-lime glass, sodium is bonded to an oxygen atom, which itself is bonded to a silicon atom, resulting

in a Si-O-Na group. This oxygen, which is bonded only to one silicon atom within the glass matrix, is termed non-bridged oxygen (NBO). The sodium is weakly bonded to the Si-O group, so that sodium can easily be displaced by an electric field, leaving behind negatively charged oxygen that is still bonded to silicon. The sodium, which is forced by the electric field, moves towards the cathode.

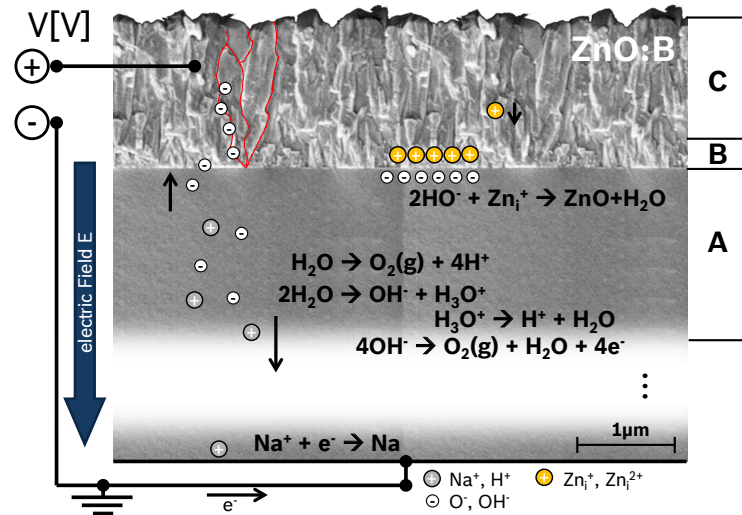


Figure 6.16: A SEM cross section illustrates the conditions under the anode (ZnO:B). Positively charged sodium ions are forced to move towards the cathode, whereas negatively charged oxygen species move towards the anode. Region A marks the ion-depleted glass layer. Region B and C mark the ZnO:B film, where cracks and delamination in the form of bubbles and circular spallings can be observed. Furthermore a lowering of electron concentration and a massive drop in mobility was found. Region B marks the ZnO:B layer next to the glass/ZnO:B interface where presumably an accumulation of zinc takes place. The red lines indicate grain boundaries.

As a result, a sub-anodic sodium-depleted negatively charged glass layer, full of NBOs and with changed physical properties (refractive index, material density), evolves (region "A") [138]. If no charge-transfer compensation mechanism is active (a current of electrons or negatively charged ions in the reverse direction of the positively charged sodium ions), the degradation current would decay and the depletion layer would fully develop, causing the external voltage to drop completely over the established depletion layer. Such a situation corresponds to case I. The thickness of the depletion layer can be assumed to be on the order of one micrometer and depends on treatment parameters such as temperature, duration, applied voltage and the glass composition. For a depletion layer thickness of $1 \mu\text{m}$ and a voltage drop of 1000 V , a 10^7 V/cm electric field is established. Again, while the voltage is applied in case II, anionic conduction is of importance. In the literature it is hypothesized that, due to such high electric field, NBOs are activated and contribute to anionic conduction [139,144]. Other publications dismiss this contribution [117,145]. Krieger et al. [117] state that it is more likely that electronic conduction occurs. In their explanation, none of the negatively charged

NBOs migrate, but electrons jump from NBO to NBO, forced by the high electric field to move towards the anode. However, such an electronic conduction mechanism alone is in contradiction to the observed evolution of oxygen at the anode, since the migration of an oxygen species towards the anode is missing.

Knowles et al. [145] argued that anionic conduction in the sodium-depleted layer under the anode is linked to the presence of a sub-surface glass layer containing water. Here, water is available in the form of protons (H^+), hydroxide ions (OH^-) and molecular H_2O [146–149]. Due to the electric field and electrolysis of water, negatively charged hydroxide ions move towards the anode and might be responsible for the observed oxygen evolution. Possible chemical reactions are indicated in Figure 6.16. This argument is also in agreement with the results and conclusions of Krieger et al. who reject the motion of NBOs [117]. Following their argument it is important to note that proton injection into the glass is important to keep up the current of ions through the sodium-depleted glass layer under the anode [149]. In the case of proton injection, the protons follow the sodium ions jumping from NBO to NBO. The hydroxide ions (OH^-) move towards the anode and presumably become oxidized to release gaseous oxygen.

To validate this argument, the degradation treatment to a LPCVD ZnO:B layer deposited on borosilicate glass was also applied. Here, no considerable increase of the ZnO:B resistance was observed. Furthermore, it was found that, whereas an almost constant current was observed during the degradation treatment using soda-lime glass as the substrate (case II), a rapid decrease of the degradation current was observed using borosilicate glass (case I). The borosilicate glass seems to block ionic as well as electronic conduction. It prevents the migration of oxygen species towards the anode and in turn the degradation of the deposited ZnO:B. The borosilicate glass possesses only a small amount of sodium, and thus fewer NBOs. Furthermore, the boron-oxygen group in borosilicate glass is known to reduce the number of NBOs further, as alkali ions stabilize boron in a tetrahedral configuration without NBOs [114]. This highlights the importance of the presence of NBOs for ionic conduction in silicate glasses, but of course is not proof of NBO motion. Due to the absence of jump-sites (NBOs) for sodium and protons, the degradation current at the beginning of the treatment rapidly decreases. The electrolysis of water, which is mainly driven by the current, stops. This in turn stops the evolution of oxygen at the anode and so does not produce a drastic increase of the ZnO:B resistance.

For soda-lime glass, it is assumed that while the degradation treatment continues the oxygen pressure at the glass/ZnO:B interface increases. Channelling of oxygen along grain boundaries could explain the strong resistance increase observed for the ZnO:B samples, since chemisorption of oxygen is likely (see region "B" and "C" red lines in Figure 6.16). Here, the chemisorbed oxygen results in a higher potential barrier and leads in turn to a drop of electron mobility. The increasing oxygen pressure could also explain the occurrence of bubbles at the beginning of the treatment, which turn

into circular spallings as shown in Figure 6.8. Carlson et al. [137, 138] reported the presence of bubbles for anodic bonding of metal foils.

Due to the external electrode potential, negatively charged species from the glass will accumulate (instead of becoming neutralized) at the glass/ZnO:B interface. As indicated in region "B" of Figure 6.16, this might attract positively charged zinc interstitials. These are forced to move toward the interface and may partially create ZnO together with the available oxygen species. Furthermore, an excess of zinc here could also explain the generation of oxygen vacancies, which would cause the yellow appearance and the red shift of optical absorption edge. Presumably, a zinc-rich ZnO:B layer is created only in the vicinity of the glass/ZnO interface. Investigations by means of energy dispersive x-ray analysis (EDX) on the samples presented in Figure 6.13 have revealed no changes. Presumably the changes induced are below the detection limits of the measurement. Nevertheless, evidence for the presence of an interface layer next to the glass/ZnO:B interface and an increased amount of oxygen vacancies somewhere in the ZnO:B material was found.

6.8 Improvements

In order to reduce the sensitivity of LPCVD-ZnO:B to the effect described above, we have seen that increasing the level of doping is one way to achieve that goal. The disadvantages of increasing the doping level are losses in optical transmission and losses in haze. The haze value is determined by the ratio of diffuse and total transmission. Sufficient haze, which is correlated to the light scattering properties of the ZnO:B front contact, is of great importance and responsible for efficient light trapping within the absorber layers of the micromorph tandem solar cell. Together with Oerlikon Solar great efforts have been made to develop other approaches in order to retain optical and electrical ZnO:B properties.

Furthermore, Bosch Solar Thin Film has independently developed a SiO_x barrier layer made by PECVD (patent pending) to further reinforce the LPCVD-ZnO. The different approaches investigated in the regard of their degradation behavior are presented in Figure 6.17. Beside the standard TCO (Std-TCO), which is homogeneously doped, the ATCO approach, developed in in the framework of the project PEPPER [1], the Lasagne-TCO and the Lasagne-TCO enhanced by an underlying SiO_x barrier layer is shown. The Lasagne-TCO is derived from the ATCO, which combines a highly doped seed layer with a lower doped bulk layer in a multilayer approach. Typical electrical and optical parameters are compared in Figure 6.18.

One can see for the differently doped Std-TCOs in Figure 6.18 the reduction of optical parameters by increasing the doping only. The haze parameter, for example, is reduced from 30 % down to 10 %. Only 10 % in haze is not enough to provide sufficient light trapping. While ATCO provides good electrical and optical properties compared

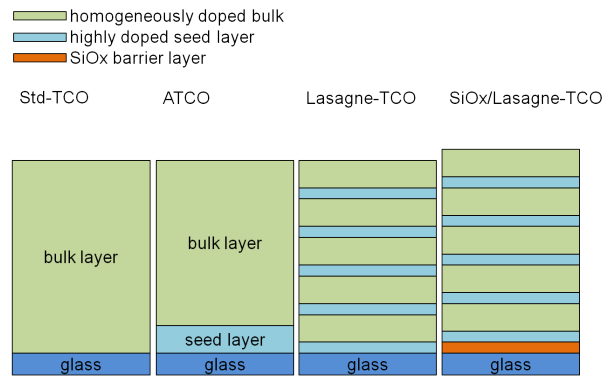


Figure 6.17: Different approaches of LPCVD ZnO:B in order to reduce the sensitivity to the hot plate and climate chamber treatment.

to the Std-TCO, Lasagne-TCO lacks in transmission due to the highly doped seed layers within the layer stack. However, the Lasagne-TCO benefits, because its haze is retained, compared to Std-TCO2 (250 sccm of B_2H_6) and the sheet resistivity is lower.

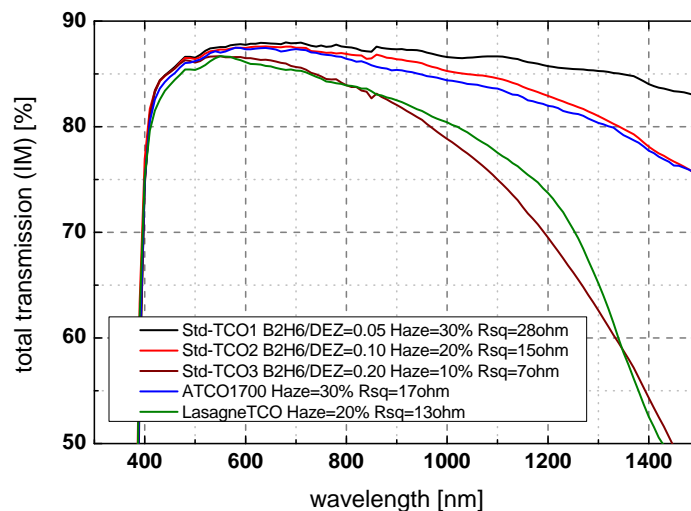


Figure 6.18: Optical and electrical properties of different homogeneously doped Std-TCOs, Lasagne-TCO and ATCO. The total transmission was measured index matched (IM) in order to avoid miss interpretation of transmission for spectral range $< 800\text{ nm}$, due to different light scattering properties of the ZnO:B layer. The layers shown have a total thickness of about 1700 nm .

In Figure 6.19 the relative change of resistance of the layers described above during the hot plate treatment is shown as a function of time. R_{ini} denotes the initial resistance measured before hot plate treatment. The samples were placed on the hot plate and biased with 1000 V , as introduced in Section 6.2. This time the temperature was lowered to 150°C resulting in a reduced rate of degradation. For comparison see Figure 6.7. Here, the degradation results were obtained for a hot plate temperature of 160°C . While the ATCO already performs much better in comparison to the Std-TCO, another significant improvement was achieved with Lasagne-TCO which performs outstandingly with only a slight increase of resistivity.

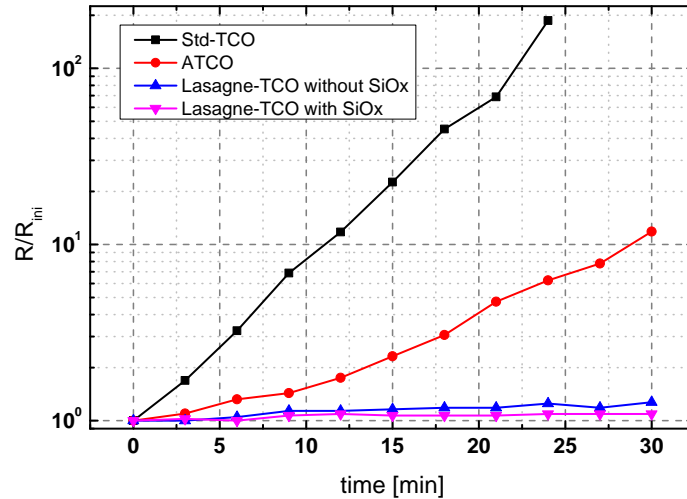


Figure 6.19: Comparison of different types of LPCVD ZnO:B treated on the hot plate at 150°C and 1 kV.

Those results can still be improved further by introducing a silicon oxide (SiO_x) barrier layer deposited by PECVD. This indicates that both the glass ZnO:B interface and especially the glass itself deserve more in-depth analysis. As mentioned, results on boron silicate glass have shown, that the degradation phenomenon discussed above can be avoided or at least significantly reduced. The stability performance of a Std-TCO, doped with 250 *sccm* of B_2H_6 , on boron silicate glass is comparable to Lasagne-TCO with SiO_x barrier layer on standard low iron soda lime glass. The working principle of the SiO_x barrier layer is not clear yet in detail. It is assumed that due to its purity (exclusion of other metal oxide inclusions, transforming the glass network) and as a result the atomic structure of the SiO_x layer plays the major role for ionic conduction.

With these promising results we went back to the climate chamber in order to validate the findings on large size modules under conditions of 85°C, 85% r.h. and 600 V positive bias. A representative number of modules presented in Figure 6.20 shows the current status of the improvements made in terms of biased damp heat behavior in the climate chamber under the aforementioned conditions.

In Figure 6.20 one can see the results gained with the initial module configuration (glass/Std-TCO/Si/Std-TCO), which was already presented in Figure 6.3, degrading most rapidly. In addition to that, four modules with different stabilized front contacts, such as SiO_x combined with Std-TCO, Lasagne-TCO, SiO_x combined with Lasagne-TCO and Std-TCO(500 *sccm* B_2H_6) are shown. From the hot plate test we expected the combination SiO_x /Lasagne-TCO to yield the best results, which is obviously not the case. The reason for that is not clear yet, but the number of modules tested in this configuration was limited by climate chamber capacity. The combination of SiO_x and Lasagne-TCO used as front contact together with Lasagne-TCO used as back contact, on the other hand, shows very promising results. It is evident from Figure 6.20, that one can increase the stability behaviour by a factor of about 6, by introducing Lasagne-

TCO as back contact, as well. Such an increase was unexpected, since the degradation phenomena were thought to be limited to the front contact only.

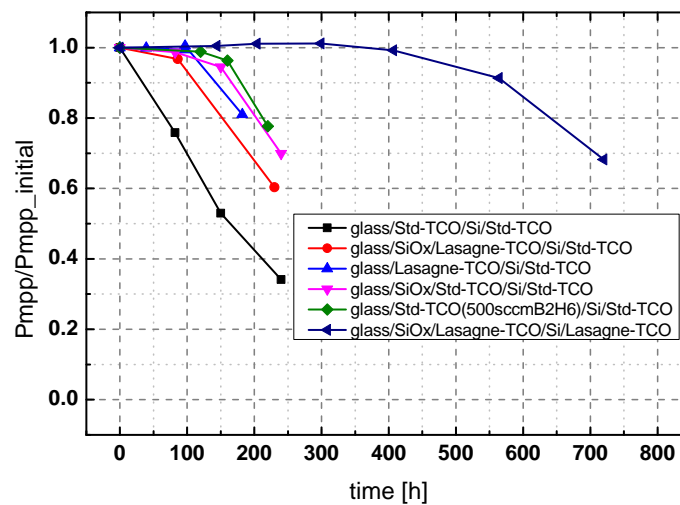


Figure 6.20: Modules under test in the climate chamber (85°C and 85% r.h.) with a voltage bias of 600 V. Different configurations have been studied to stabilize the power loss.

Further efforts have to be made in order to understand and to separate the degradation phenomena of the Std-TCO front and back contact.

6.9 Conclusion

The investigations presented in this report have shown the limitations of the current IEC standard and the importance of damp heat testing under voltage bias. The results were generated under harsh conditions and should be considered preliminary. Nevertheless, they contribute to a better understanding of possible degradation mechanisms. All findings discussed above stress the importance of layer properties in order to improve the stability. But also the glass, which seems to play a major role for TCO (ZnO:B) degradation, and the module mounting system, which has a huge impact on the leakage current, responsible for degradation, have to be subjected to critical scrutiny. Furthermore, we have seen that ATCO, developed in the framework of the PEPPER project tends to be more stable than Std-TCO.

In the present work a new degradation mechanism of ZnO:B deposited on commercial soda-lime glass was shown. It was found that anodic field-induced degradation leads to a drastic increase of the ZnO:B resistance. From Hall effect measurements it was concluded that the strong resistance increase is caused by a significant loss in electron mobility. Furthermore, the limiting scattering mechanism was found to be located at the grain boundaries of the polycrystalline ZnO:B film. It was shown that such an increase impacts the power output of a small unencapsulated module as well as of large size modules. Here, the series resistance of the modules was strongly increased.

The degraded ZnO layer possesses a yellow coloration which coincides with a shift in the optical absorption edge towards longer wavelengths. Observed circular spallings and bubbles on top of the ZnO layer indicate the evolution of gas at the glass/ZnO:B (anode) interface. It is highly likely that oxygen is the evolving gas. Two oxygen sources were proposed. The first source is water, which is incorporated into the sub-anodic glass layer due to impurities at the glass/ZnO:B interface. Due to the high voltage and the electrolysis of water at the anode (ZnO:B) a certain amount of oxygen evolves. A second source of oxygen is correlated with the presence of negatively charged non-bridged oxygen (NBO) in the glass matrix caused by the motion of sodium towards the cathode. The motion of sodium leads to the creation of a sub-anodic depletion layer full of NBOs. Due to the presence of the high electric field these NBOs might be forced to move towards the anode. The gaseous oxygen is partially channelled through grain boundaries. This increases the defect density, which coincides with a drop in electron mobility. The yellow appearance of the sample after degradation could be explained by the accumulation of interstitial zinc (Zn^+ , Zn^{2+}) at the ZnO:B/glass interface. The excess of zinc leads to the creation of oxygen vacancies. These defects are known to be defect states within the bandgap and are responsible for the red shift of the absorption edge. Evidence for the creation of oxygen vacancies and the presents of an interface layer next to the glass/ZnO:B interface were found.

To avoid such degradation and to assure a long module lifetime, a proper, highly insulating mounting system is useful [150]. Also a barrier layer between the glass and ZnO is able to interrupt the degradation process. Another option is the prevention of positive high voltage between a module's photovoltaic active layers and the grounded mounting system. This can be achieved by grounding the positive pole of the module string. For Bosch Thin-Film Modules mounted in non-Bosch mounting systems, it is recommended to ground the negative pole of the module string. In this configuration, well-known cathodic degradation is avoided, whereas the presented anodic degradation is sufficiently suppressed by an applied barrier layer.

Chapter 7

Summary

The present work discussed advanced LPCVD ZnO and its challenges in application for thin-film solar cells and modules. Here, advanced LPCVD ZnO refers to ZnO layers that try to overcome to current limitations of standard boron-doped LPCVD ZnO:B, typically used as front and back electrodes. These limitations are related to optical and electrical properties and to the surface morphology influencing the quality and therefore the efficiency of the subsequently deposited solar cell structure.

In Chapter 4 the suitability of adding ethanol as an additional precursor during ZnO:B deposition to create a surface morphology that is more favorable for $\mu\text{c-Si:H}$ growth was evaluated. It was found that ethanol has a strong impact on the electrical and optical properties of 2- μm -thick ZnO layers. The growth model proposed is based on the assumption of a surface reaction and that oxygen, delivered by the ethanol, is incorporated at the ZnO surface at oxygen vacancy sites. Although ethanol-enriched ZnO single layers might be suitable for good $\mu\text{c-Si:H}$ growth, their high resistivity of up to 200 Ωcm rules out their usage as electrodes for photovoltaic applications. In a two-step deposition process, a 200- nm -thick ethanol-enriched ZnO cap layer on top of a 1900- nm -thick as-grown rough ZnO film was deposited. A change in surface morphology was observed for these bilayers as well. The sheet resistance of bilayer films was maintained at reasonable values, independent of the thickness of the ethanol-enriched cap layer. It was found that the used four point probe measurement was not sensitive to the resistive cap layer. To solve resistivity issues, which might become a problem for the potential application of bilayers, additional doping of the underlying and cap layers still has to be studied. Future work will have to be done to investigate the effects of deposition parameters like pressure and temperature on morphology. Also, other types of precursors should be considered to induce morphological changes. Finally, a complete solar cell, incorporating an optimized bilayer as the front electrode, will have to be tested. Meanwhile work has been carried out by Ding et al. (to be published) incorporating the above-presented approach into a micromorph solar cell. Cell efficiencies above 12.2% were achieved. Despite these results, the introduction of

ethanol-enriched bilayers into mass production of thin-film silicon solar modules still is far away from realization. The process still has to be upscaled to substrate sizes of $1.1 \times 1.3 \text{ m}^2$, and a production tool that enables the deposition of ethanol-enriched bilayers has to be developed.

Another approach to an advanced LPCVD ZnO:B was followed by Ding et al. [1,2]. For an advanced TCO (ATCO), they combined a highly doped ZnO:B seed layer with a low-doped ZnO:B bulk layer. Compared to a standard ZnO:B (Std-TCO), which is homogeneously doped across the total layer thickness, their ATCO possesses enhanced optical and electrical properties. For the first time, in Chapter 5 the introduction of this ATCO into the production line at Bosch Solar Thin Film in Erfurt, Germany, on substrate sizes of $1.1 \times 1.3 \text{ m}^2$ was discussed. Therefore, the deposition tool TCO1200 needed to be retrofitted. Comparing the ATCO with the Std-TCO, equal in layer thickness (1800 nm) and sheet resistance (16 to 17Ω), ATCO possesses slightly better in transmittance. Furthermore, ATCO showed 37% haze, which is 3 to 5% absolute more haze compared to the Std-TCO. After ATCO optimization, a complete micromorph solar module was fabricated, incorporating this new advanced LPCVD ZnO:B layer as the front electrode. An initial module power of 153.7 Wp was achieved.

After the introduction of new processes and materials, module manufactures are usually committed to detailed tests, confirming product quality. One of these tests is an accelerated damp heat lifetime test according to IEC61646, in which the modules have to be exposed to 85°C and 85% relative humidity for 1000 h. In Chapter 6 the limitation of the current IEC standard was discussed. Furthermore, the importance of test conditions with regard to considering a voltage bias, which is not yet included in the current IEC standard, was shown. Note that the results in the present work were generated under harsh conditions and should be considered preliminary. Nevertheless, they contribute a better understanding of possible degradation mechanisms. In the present work, for the first time, a novel degradation mechanism of ZnO:B on soda-lime glass was introduced. A degradation model was proposed and solutions for minimizing the degradation effect were presented. It was found that the resistance of the ZnO:B front electrode strongly increases, when the ZnO:B electrode is biased with a positive potential against a grounded module frame or mounting system. As a result the module power was found to decrease. The investigations have shown that ZnO:B grain boundaries are strongly affected by adsorbed or chemisorbed oxygen species coming from glass. At the ZnO:B grain boundaries the increased number of oxygen species leads to an increased defect concentration. These defects are known to build a potential barrier, which electrons have to overcome by thermionic emission or quantum mechanical tunneling. The increased defect concentration leads to an observable drop in electron mobility and as a result to a major rise of ZnO:B resistivity.

To avoid such degradation and to assure a long module lifetime, a proper, highly insulating mounting system is useful [150]. The introduction of a SiO_x barrier layer

between the glass and the ZnO:B layer (patent pending) prevents front electrode degradation and enhances module lifetime. Another option is the prevention of positive high voltage between a module's photovoltaic active layers and the grounded mounting system. This can be achieved by grounding the positive pole of the module string. A further prevention can be achieved by a higher doping level of the ZnO:B layer. Due to the higher doping level, the increase of the barrier height and width during degradation at ZnO:B grain boundaries is reduced.

References

- [1] Ding, L., M. Boccard, G. Bugnon, M. Benkhaira, M. Despeisse, F. Sculati-Meillaud, S. Nicolay, P.A. Losio, O. Kluth, P. Carroy, *et al.*: *New generation transparent LPCVD ZnO electrodes for enhanced photocurrent in micromorph solar cells and modules*. IEEE Journal of Photovoltaics, 2(2):88–93, 2012.
- [2] Ding, L., M. Boccard, G. Bugnon, M. Benkhaira, S. Nicolay, M. Despeisse, F. Meillaud, and C. Ballif: *Highly transparent ZnO bilayers by LP-MOCVD as front electrodes for thin-film micromorph silicon solar cells*. Solar Energy Materials and Solar Cells, 98:331–336, 2012.
- [3] British Petroleum (BP): *60 years BP statistical review of world energy*, 2011. <http://www.bp.com/en/global/corporate/about-bp/statistical-review-of-world-energy-2013/statistical-review-1951-2011.html>, visited on 2013-08-29.
- [4] British Petroleum (BP): *BP statistical review of world energy june 2013*, 2013. <http://www.bp.com/en/global/corporate/about-bp/statistical-review-of-world-energy-2013/statistical-review-downloads.html>, visited on 2013-08-29.
- [5] Roedel, W.: *Physik unserer Umwelt: Die Atmosphäre*. Springer, 2000.
- [6] TEL Solar AG (formerly Oerlikon Solar AG), Ecole Polytechnique Federale de Lausanne, University of Northumbria at Newcastle, Bosch Solar Thin Film GmbH, Linde AG, Heliosphera, and University of Patras: *Demonstration of high performance processes and equipments for thin film silicon photovoltaic modules produced with lower environmental impact and reduced cost and material use*. http://cordis.europa.eu/projects/rcn/100464_en.html, visited on 2013-08-29.
- [7] Messerschmidt, D., S. Nicolay, L. Ding, G. Bugnon, F. Meillaud, J. Eberhardt, and C. Ballif: *Ethanol-enriched low-pressure chemical vapor deposition ZnO bilayers: Properties and growth - a potential electrode for thin film solar cells*. Journal of Applied Physics, 113(2):024908–024908, 2013.
- [8] Messerschmidt, D., A. Hochmuth, E. Rädlein, H. Romanus, W.M. Gnehr, J. Eberhardt, and C. Ballif: *Anodic degradation of zno on soda-lime glass*. Solar Energy Materials and Solar Cells, 117:569–576, 2013.
- [9] Messerschmidt, D., K. Bratz, W.M. Gnehr, H. Romanus, J. Eberhardt, S. Nicolay, and C. Ballif: *Optical properties of anodically degraded zno*. Journal of Applied Physics, 115(9):094902, 2014.
- [10] Shah, A.V., H. Schade, M. Vanecek, J. Meier, E. Vallat-Sauvain, N. Wyrsh, U. Kroll, C. Droz, and J. Bailat: *Thin-film silicon solar cell technology*. Progress in Photovoltaics: Research and Applications, 12(2-3):113–142, 2004.
- [11] Ellmer, K., A. Klein, and B. Rech: *Transparent conductive zinc oxide*, volume 104. Springer, 2008.

- [12] Herold, R.J., S.L. Aggarwal, and V. Neff: *Mechanisms of the reactions of diethylzinc with isopropanol and water*. Canadian Journal of Chemistry, 41(5):1368–1380, 1963.
- [13] Smith, S.M. and H.B. Schlegel: *Molecular orbital studies of zinc oxide chemical vapor deposition: gas-phase hydrolysis of diethyl zinc, elimination reactions, and formation of dimers and tetramers*. Chemistry of Materials, 15(1):162–166, 2003.
- [14] Kim, Y.S., Y.S. Won, H. Hagelin-Weaver, N. Omenetto, and T. Anderson: *Homogeneous decomposition mechanisms of diethylzinc by raman spectroscopy and quantum chemical calculations*. The Journal of Physical Chemistry A, 112(18):4246–4253, 2008.
- [15] Faÿ, S.: *L'oxyde de zinc par dépôt chimique en phase vapeur comme contact électrique transparent et diffuseur de lumière pour les cellules solaires*. Phd. thesis, University of Neuchâtel, 2003.
- [16] Nicolay, S., S. Faÿ, and C. Ballif: *Growth model of MOCVD polycrystalline ZnO*. Crystal Growth & Design, 9(11):4957–4962, 2009.
- [17] Kashiwaba, Y., F. Katahira, K. Haga, T. Sekiguchi, and H. Watanabe: *Heteroepitaxial growth of ZnO thin films by atmospheric pressure CVD method*. Journal of Crystal Growth, 221(1):431–434, 2000.
- [18] Oda, S., H. Tokunaga, N. Kitajima, J. Hanna, I. Shimizu, and H. Kokado: *Highly oriented ZnO films prepared by MOCVD from diethylzinc and alcohols*. Japanese Journal of Applied Physics, 24(12):1607–1610, 1985.
- [19] Hu, J. and R.G. Gordon: *Textured fluorine-doped ZnO films by atmospheric pressure chemical vapor deposition and their use in amorphous silicon solar cells*. Solar Cells, 30(1):437–450, 1991.
- [20] Gruber, Th., C. Kirchner, and A. Waag: *MOCVD growth of ZnO on different substrate materials*. physica status solidi (b), 229(2):841–844, 2002.
- [21] Oleynik, N., A. Dadgar, J. Christen, J. Bläsing and M. Adam, T. Riemann, A. Diez, A. Greiling, and M. Seip and A. Krost: *Growth of ZnO layers by metal organic chemical vapor phase epitaxy*. physica status solidi (a), 192(1):189–194, 2002.
- [22] Kaufmann, Th., E. Fuchs, and M. Webert: *Metalorganic chemical vapour deposition of oriented ZnO films*. Crystal Research and Technology, 23(5):635–639, 1988.
- [23] Hahn, B., G. Heindel, E. Pschorr-Schoberer, and W. Gebhardt: *MOCVD layer growth of ZnO using DMZn and tertiary butanol*. Semiconductor Science and Technology, 13(7):788, 1998.
- [24] Sallet, V., J.F. Rommeluere, A. Lusson, A. Riviere, S. Fusil, O. Gorochoy, and R. Triboulet: *MOCVD growth of ZnO on sapphire using tert-butanol*. physica status solidi (b), 229(2):903–906, 2002.
- [25] Ogata, K., T. Kawanishi, K. Maejima, K. Sakurai, Sz. Fujita, and Sg. Fujita: *ZnO growth using homoepitaxial technique on sapphire and Si substrates by metalorganic vapor phase epitaxy*. Journal of Crystal Growth, 237:553–557, 2002.
- [26] Dadgar, A., N. Oleynik, D. Forster, S. Deiter, H. Witek, J. Bläsing, F. Bertram, A. Krtschil, A. Diez, J. Christen, *et al.*: *A two-step metal organic vapor phase epitaxy growth method for high-quality ZnO on GaN/Al₂O₃ (0001)*. Journal of Crystal Growth, 267(1):140–144, 2004.

- [27] Faÿ, S., U. Kroll, C. Bucher, and E. Vallat Sauvain and A. Shah: *Low pressure chemical vapour deposition of ZnO layers for thin-film solar cells: temperature-induced morphological changes*. Solar Energy Materials and Solar Cells, 86(3):385–397, 2005.
- [28] Faÿ, S., L. Feitknecht, R. Schlüchter, U. Kroll, E. Vallat-Sauvain, and A. Shah: *Rough ZnO layers by LP-CVD process and their effect in improving performances of amorphous and microcrystalline silicon solar cells*. Solar Energy Materials and Solar Cells, 90(18):2960–2967, 2006.
- [29] Faÿ, S., J. Steinhauser, N. Oliveira, E. Vallat-Sauvain, and C. Ballif: *Opto-electronic properties of rough LP-CVD ZnO:B for use as TCO in thin-film silicon solar cells*. Thin Solid Films, 515(24):8558–8561, 2007.
- [30] Faÿ, S., J. Steinhauser, S. Nicolay, and C. Ballif: *Polycrystalline ZnO:B grown by LPCVD as TCO for thin film silicon solar cells*. Thin Solid Films, 518(11):2961–2966, 2010.
- [31] Özgür, U., Y.I. Alivov, C. Liu, A. Teke, MA Reshchikov, S. Dogan, V. Avrutin, S.J. Cho, and H. Morkoc: *A comprehensive review of ZnO materials and devices*. Journal of Applied Physics, 98(4):041301, 2005.
- [32] McCluskey, M.D. and S.J. Jokela: *Defects in ZnO*. Journal of Applied Physics, 106(7):071101–071101, 2009.
- [33] Janotti, A. and C.G. Van de Walle: *Hydrogen multicentre bonds*. Nature Materials, 6(1):44–47, 2006.
- [34] Seto, John Y.W: *The electrical properties of polycrystalline silicon films*. Journal of Applied Physics, 46(12):5247–5254, 1975.
- [35] Steinhauser, J.: *Low pressure chemical vapor deposited zinc oxide for silicon thin film solar cells optical and electrical properties*. Phd. thesis, University of Neuchâtel, 2008.
- [36] Steinhauser, J., S. Faÿ, N. Oliveira, E. Vallat-Sauvain, D. Zimin, U. Kroll, and C. Ballif: *Electrical transport in boron-doped polycrystalline zinc oxide thin films*. physica status solidi (a), 205(8):1983–1987, 2008.
- [37] Steinhauser, J., S. Faÿ, N. Oliveira, E. Vallat-Sauvain, and C. Ballif: *Transition between grain boundary and intragrain scattering transport mechanisms in boron-doped zinc oxide thin films*. Applied Physics Letters, 90(14):142107–142107, 2007.
- [38] Steinhauser, J., S. Meyer, M. Schwab, S. Faÿ, C. Ballif, U. Kroll, and D. Borrello: *Humid environment stability of low pressure chemical vapor deposited boron doped zinc oxide used as transparent electrodes in thin film silicon solar cells*. Thin Solid Films, 520(1):558–562, 2011.
- [39] Burstein, E.: *Anomalous optical absorption limit in InSb*. Physical Review, 93(3):632, 1954.
- [40] Wang, J., Z. Wang, B. Huang, Y. Ma, Y. Lui, X. Qin, X. Zhang, and Y. Dai: *Oxygen vacancy induced band-gap narrowing and enhanced visible light photocatalytic activity of ZnO*. Applied Materials and Interfaces, 4:4024–4030, 2012.
- [41] Srikant, V. and D.R. Clarke: *Optical absorption edge of ZnO thin films: The effect of substrate*. Journal of Applied Physics, 81(9):6357–6364, 1997.
- [42] Fox, A.M.: *Optical properties of solids*, volume 3. Oxford university press, 2001.

- [43] Kim, I., K.S. Lee, T.S. Lee, J. Jeong, B. Cheong, Y.J. Baik, and W.M. Kim: *Effect of fluorine addition on transparent and conducting Al doped ZnO films*. Journal of Applied Physics, 100(6):063701–063701, 2006.
- [44] Wolden, C.A., T.M. Barnes, J.B. Baxter, and E.S. Aydil: *Infrared detection of hydrogen-generated free carriers in polycrystalline ZnO thin films*. Journal of Applied Physics, 97(4):043522–043522, 2005.
- [45] Ruske, F., A. Pflug, V. Sittinger, B. Szyszka, D. Greiner, and B. Rech: *Optical modeling of free electron behavior in highly doped ZnO films*. Thin Solid Films, 518(4):1289–1293, 2009.
- [46] Prunici, P., F.U. Hamelmann, W. Beyer, H. Kurz, and H. Stiebig: *Modelling of infrared optical constants for polycrystalline low pressure chemical vapour deposition ZnO:B films*. Journal of Applied Physics, 113(12):123104–123104, 2013.
- [47] Born, M. and E. Wolf: *Principles of optics: electromagnetic theory of propagation, interference and diffraction of light*. CUP Archive, 1999.
- [48] Hecht, E. and A. Zajac: *Optics*. Addison Wesley, New York, 2002.
- [49] Aspnes, D.E.: *Optical properties of thin films*. Thin Solid Films, 89:249–262, 1982.
- [50] Maxwell-Garnett, J.C.: *Colours in metal glasses and in metal films*. Philos. Trans. R. Soc. London, 203:385–420, 1904.
- [51] Donker, M.N.: *Plasma Deposition of Microcrystalline Silicon Solar Cells: Looking Beyond the Glass*. Phd. thesis, Forschungszentrum Jülich, 2006.
- [52] Lejeune, M., W. Beyer, R. Carius, J. Müller, and B. Rech: *Silicontetrachloride based microcrystalline silicon for application in thin film silicon solar cells*. Thin Solid Films, 451-452:280, 2004.
- [53] Platz, R. and S. Wagner: *Intrinsic microcrystalline silicon by plasma-enhanced chemical vapor deposition from dichlorsilanne*. Applied Physics Letters, 73:1236, 1998.
- [54] Cicala, G., P. Capezzuto, and G. Bruno: *From amorphous to microcrystalline silicon deposition in $\text{SiF}_4 - \text{H}_2$ -He plasmas: in situ control by optical emission spectroscopy*. Thin Solid Films, 383:203, 2001.
- [55] Rech, B.: *Solarzellen aus amorphem Silizium mit hohem stabilem Wirkungsgrad*. Phd. thesis, RWTH Aachen, 1997.
- [56] Meier, J., S. Dubail, R. Fluckiger, D. Fischer, H. Keppner, and A. Shah: *Intrinsic microcrystalline silicon ($\mu\text{-Si: H}$)-a promising new thin film solar cell material*. In *Photovoltaic Energy Conversion, 1994., Conference Record of the Twenty Fourth. IEEE*, volume 1, pages 409–412. IEEE, 1994.
- [57] Meier, J., U. Kroll, S. Dubail, S. Golay, S. Faÿ, J. Dubail, and A. Shah: *Efficiency enhancement of amorphous silicon pin solar cells by LP-CVD ZnO*. In *Photovoltaic Specialists Conference, 2000. Conference Record of the Twenty-Eighth IEEE*, pages 746–749. IEEE, 2000.
- [58] Chittick, R., J. Alexande, and H. Sterling: *The preparation and properties of amorphous silicon*. Journal of the Electrochemical Society, 116:77, 1969.
- [59] Spear, W. and P. LeComber: *Electronic properties of substitutionally doped amorphous Si and Ge*. Philosophical Magazine, 33:935, 1976.
- [60] Wagemann, Hans G. and H. Eschrich: *Photovoltaik – Solarstrahlung und Halbleitereigenschaften*. B. G. Teubner, 2007.

- [61] Senoussaoui, N.: *Einfluss der Oberflächenstrukturierung auf die optischen Eigenschaften der Dünnschichtsolarzellen auf Basis von a -Si:H und μ c-Si:H*. Phd. thesis, Heinrich-Heine-Universität Düsseldorf, 2003.
- [62] Vetterl, O.: *On the Physics of Microcrystalline Silicon Thin Film Solar Cells; From the Material to Devices with High Conversion Efficiencies*. Phd. thesis, Forschungszentrum Jülich, 2001.
- [63] Shah, A.V., J. Meier, E. Vallat-Sauvain, N. Wyrsh, U. Kroll, C. Dorz, and U. Graf: *Material and solar cell research in microcrystalline silicon*. Solar Energy Materials and Solar Cells, 78:469, 2003.
- [64] Houben, L.: *Plasmaabscheidung von mikrokristallinem Silizium: Merkmal der Mikrostruktur und deren Deutung im Sinne von Wachstumsvorgängen*. Phd. thesis, Heinrich-Heine-Universität Düsseldorf, 1998.
- [65] Shah, A., C. Ballif, W. Beyer, J.E. Bouree, C. Dorz, F. Finger, M. Python, J. Randall, and H. Schade and N. Wyrsh: *Thin-film silicon solar cells*. EPFL Press, 2010.
- [66] Würfel, P.: *Physik der Solarzellen*. Spektrum, Akad. Verlag, 2000.
- [67] Green, M.A., K. Emery, Y. Hishikawa, W. Warta, and E.D. Dunlop: *Solar cell efficiency tables (version 41)*. Progress in Photovoltaics: Research and Applications, 21(1):1–11, 2013.
- [68] Holovský, J., M. Bonnet-Eymard, M. Boccard, M. Despeisse, and C. Ballif: *Variable light biasing method to measure component I - V characteristics of multi-junction solar cells*. Solar Energy Materials and Solar Cells, 103:128–133, 2012.
- [69] Sze, S.M. and K.K. Ng: *Physics of semiconductor devices*. Wiley, 2006.
- [70] Goetzberger, A., B. Voß, and J. Knobloch: *Sonnenenergie: Photovoltaik: Physik und Technologie der Solarzellebildungen*. Teubner, 1997.
- [71] Bamford, C.R.: *Optical properties of flat glass*. Journal of Non-Crystalline Solids, 47:1–20, 1982.
- [72] Rubin, M.: *Optical properties of soda lime silica glasses*. Solar Energy Materials, 12(4):275–288, 1985.
- [73] Wartewig, S.: *IR and Raman Spectroscopy*. John Wiley & Sons, 2006.
- [74] Bennett, J.M. and E.J. Ashley: *Infrared reflectance and emittance of silver and gold evaporated in ultrahigh vacuum*. Applied Optics, 4:221–224, 1965.
- [75] Long, D.A.: *The Raman effect: A unified treatment of the theory of Raman scattering by molecules*. West Sussex, England: John Wiley & Sons Ltd, 2002.
- [76] Schroder, D.K.: *Semiconductor material and device characterization*. John Wiley & Sons, 2006.
- [77] Magonov, S.N. and M.H. Whangbo: *Surface analysis with STM and AFM: experimental and theoretical aspects of image analysis*. Wiley, 2008.
- [78] Binnig, G., C.F. Quate, and Ch. Gerber: *Atomic force microscope*. Physical Review Letters, 56:930, 1986.
- [79] Spiess, L., G. Teichert, R. Schwarzer, H. Behnken, and C. Genzel: *Moderne röntgenbeugung: röntgendiffraktometrie für materialwissenschaftler, physiker und chemiker*. Springer, 2009.
- [80] Lüth, H.: *Solid surfaces, interfaces and thin films*, volume 3. Springer, 2001.

- [81] Czanderna, A.W.: *Methods of surface analysis*. North Holland, 1984.
- [82] M. Grasserbauer, H. Dudek, M.F. Ebel: *Angewandte Oberflächenanalyse mit SIMS, AES, XPS*. Springer-Verlag, 1986.
- [83] Wacom Electric Co., LTD.: *Super solar simulator (2 lamps type)-specifications*. www.wacom-ele.co.jp/Solar/ENGsolar2.htm, visited on 2013-08-29.
- [84] Kluth, O., A. Löffl, S. Wieder, C. Beneking, W. Appenzeller, L. Houben, B. Rech, H. Wagner, S. Hoffmann and R. Waser, *et al.*: *Texture etched Al-doped ZnO: a new material for enhanced light trapping in thin film solar cells*. In *Photovoltaic Specialists Conference, 1997., Conference Record of the Twenty-Sixth IEEE*, pages 715–718. IEEE, 1997.
- [85] Staebler, D.L. and C.R. Wronski: *Reversible conductivity changes in discharge-produced amorphous Si*. Applied Physics Letters, 31(4):292–294, 1977.
- [86] Python, M., E. Vallat-Sauvain, J. Bailat, D. Dominé, L. Fesquet, A. Shah, and C. Ballif: *Relation between substrate surface morphology and microcrystalline silicon solar cell performance*. Journal of Non-Crystalline Solids, 354(19):2258–2262, 2008.
- [87] Johnson, E.V., M. Nath, P. Roca i Cabarrocas, A. Abramov, and P. Chatterjee: *Why does the open-circuit voltage in a micro-crystalline silicon pin solar cell decrease with increasing crystalline volume fraction?* Journal of Non-Crystalline Solids, 354(19):2455–2459, 2008.
- [88] Python, M.: *Microcrystalline Silicon Solar Cells: Growth and Defects*. Phd. thesis, University of Neuchâtel, 2009.
- [89] Despeisse, M., C. Battaglia, M. Boccard, G. Bugnon, M. Charrière, P. Cuony, S. Hänni, L. Löfgren, F. Meillaud, G. Parascandolo, *et al.*: *Optimization of thin film silicon solar cells on highly textured substrates*. physica status solidi (a), 208(8):1863–1868, 2011.
- [90] Bailat, J., D. Dominé, R. Schluchter, J. Steinhauser, S. Faÿ, F. Freitas, C. Bucher, L. Feitknecht, X. Niquille, T. Tschärner, *et al.*: *High-efficiency pin microcrystalline and micromorph thin film silicon solar cells deposited on LPCVD ZnO coated glass substrates*. In *Photovoltaic Energy Conversion, Conference Record of the 2006 IEEE 4th World Conference on*, volume 2, pages 1533–1536. IEEE, 2006.
- [91] Hüpkens, J., B. Rech, O. Kluth, T. Repmann, B. Zwaygardt, J. Müller, R. Drese, and M. Wuttig: *Surface textured MF-sputtered ZnO films for microcrystalline silicon-based thin-film solar cells*. Solar Energy Materials and Solar Cells, 90(18):3054–3060, 2006.
- [92] Wenas, W.W. and M. Konagai: *Control of the surface morphology of ZnO thin films for solar cells by novel two-step MOCVD process*. In *Photovoltaic Specialists Conference, 2002. Conference Record of the Twenty-Ninth IEEE*, pages 1130–1133. IEEE, 2002.
- [93] Hongsingthong, A., I. Afdi Yunaz, S. Miyajima, and M. Konagai: *Preparation of ZnO thin films using MOCVD technique with D₂O/H₂O gas mixture for use as TCO in silicon-based thin film solar cells*. Solar Energy Materials and Solar Cells, 95(1):171–174, 2011.
- [94] Kim, Y. and Y. Won: *Investigations on reaction pathways for ZnO formation from diethylzinc and water during chemical vapor deposition*. Bulletin of the Korean Chemical Society, 30(7):1573–1578, 2009.

- [95] Matxain, J.M., J.E. Fowler, and J.M. Ugalde: *Small clusters of II-VI materials: Zn_iO_i , $i=1-9$* . Physical Review A, 62(5):053201, 2000.
- [96] Vohs, J.M. and M.A. Barteau: *Dehydration and dehydrogenation of ethanol and 1-propanol on the polar surfaces of zinc oxide*. Surface science, 221(3):590–608, 1989.
- [97] Mokwa, W., D. Kohl, and G. Heiland: *Decomposition of ethanol and acetaldehyde on clean ZnO prism and oxygen faces*. Surface Science, 117(1):659–667, 1982.
- [98] Kwak, G. and K. Yong: *Adsorption and reaction of ethanol on ZnO nanowires*. The Journal of Physical Chemistry C, 112(8):3036–3041, 2008.
- [99] Pagni, O. and A.W.R. Leitch: *Influence of VI:II ratio on the properties of MOCVD-grown ZnO thin films*. physica status solidi (a), 201(10):2213–2218, 2004.
- [100] Zhu-xi, F., G. Chang-xin, L. Bi-xia, and L. Gui-hong: *Cathodoluminescence of ZnO films*. Chinese Physics Letters, 15(6):457–459, 1998.
- [101] Vanheusden, K., C.H. Seager, W.L. Warren, D.R. Tallant, and J.A. Voigt: *Correlation between photoluminescence and oxygen vacancies in ZnO phosphors*. Applied Physics Letters, 68(3):403–405, 1996.
- [102] Lany, S. and A. Zunger: *Anion vacancies as a source of persistent photoconductivity in II-VI and chalcopyrite semiconductors*. Physical Review B, 72(3):035215, 2005.
- [103] Hofmann, D.M., A. Hofstaetter, F. Leiter, H. Zhou, F. Henecker, B.K. Meyer, S.B. Orlinskii, J. Schmidt, and P.G. Baranov: *Hydrogen: a relevant shallow donor in zinc oxide*. Physical Review Letters, 88(4):45504, 2002.
- [104] Marcel, C., N. Naghavi, G. Couturier, and J. Salardenne and J.M. Tarascon: *Scattering mechanisms and electronic behavior in transparent conducting $Zn_xIn_2O_{x+3}$ indium-zinc oxide thin films*. Journal of Applied Physics, 91(7):4291–4297, 2002.
- [105] Ding, L., L. Fanni, D. Messerschmidt, S. Zabihzadeh, M. Masis Morales, S. Nicolay, and C. Ballif: *Tailoring the surface morphology of zinc oxide films for high-performance micromorph solar cells*. Solar Energy Materials and Solar Cells, 128:378–385, 2014.
- [106] Nicolay, S., M. Benkhaira, L. Ding, J. Escarre, G. Bugnon, F. Meillaud, and C. Ballif: *Control of CVD-deposited ZnO films properties through water/DEZ ratio: Decoupling of electrode morphology and electrical characteristics*. Solar Energy Materials and Solar Cells, 105:46–52, 2012.
- [107] Berghold, J., O. Frank, H. Hoehne, S. Pingel, B. Richardson, and M. Winkler: *Potential induced degradation of solar cells and panels*. pages 3753–3759, 2010.
- [108] Weber, T., E. Benfares, S. Krauter, and P. Grunow: *Electroluminescence on the TCO corrosion of thin film modules*. 25th EUPVSEC, Valencia, page 3169, 2010.
- [109] Osterwald, C.R., T.J. McMahon, and J.A. Del Cueto: *Electrochemical corrosion of SnO_2 : F transparent conducting layers in thin-film photovoltaic modules*. Solar Energy Materials and Solar Cells, 79(1):21–33, 2003.
- [110] Osterwald, C.R., T.J. McMahon, J.A. del Cueto, J. Adelstein, and J. Pruet: *Accelerated stress testing of thin-film modules with SnO_2 : F transparent conductors*. In *National Center for Photovoltaics and Solar Program Review Meeting Denver, Colorado March*, pages 24–26, 2003.

- [111] Jansen, K.W. and A.E. Delahoy: *A laboratory technique for the evaluation of electrochemical transparent conductive oxide delamination from glass substrates*. Thin Solid Films, 423(2):153–160, 2003.
- [112] Carlson, D.E., R. Romero, F. Willing, D. Meakin, L. Gonzalez, R. Murphy, H.R. Moutinho, and M. Al-Jassim: *Corrosion effects in thin-film photovoltaic modules*. Progress in Photovoltaics: Research and Applications, 11(6):377–386, 2003.
- [113] Dunken, H.H.: *Physikalische Chemie der Glasoberfläche*. VEB Deutscher Verlag für Grundstoffindustrie, 1981.
- [114] Scholze, H. and M.J. Lakin: *Glass: nature, structure, and properties*. Springer, 1991.
- [115] Greuter, F. and G. Blatter: *Electrical properties of grain boundaries in polycrystalline compound semiconductors*. Semiconductor Science and Technology, 5(2):111–137, 1990.
- [116] Ellmer, K. and R. Mientus: *Carrier transport in polycrystalline transparent conductive oxides: A comparative study of zinc oxide and indium oxide*. Thin Solid Films, 516(14):4620–4627, 2008.
- [117] Krieger, U.K. and W.A. Lanford: *Field assisted transport of Na^+ ions, Ca^{2+} ions and electrons in commercial soda-lime glass I: Experimental*. Journal of Non-Crystalline Solids, 102(1):50–61, 1988.
- [118] Pflug, A., V. Sittinger, F. Ruske, B. Szyszka, and G. Dittmar: *Optical characterization of aluminum-doped zinc oxide films by advanced dispersion theories*. Thin Solid Films, 455:201–206, 2004.
- [119] Solieman, A. and M.A. Aegerter: *Modeling of optical and electrical properties of $\text{In}_2\text{O}_3 : \text{Sn}$ coatings made by various techniques*. Thin Solid Films, 502(1):205–211, 2006.
- [120] Mergel, D. and Z. Qiao: *Dielectric modelling of optical spectra of thin $\text{In}_2\text{O}_3 : \text{Sn}$ films*. Journal of Physics D: Applied Physics, 35(8):794, 2002.
- [121] Calleja, J.M. and M. Cardona: *Resonant raman scattering in ZnO*. Physical Review B, 16(8):3753, 1977.
- [122] Cuscó, R., E. Alarcón-Lladó, J. Ibanez and L. Artus, J. Jimenez, B. Wang, and M.J. Callahan: *Temperature dependence of raman scattering in ZnO*. Physical Review B, 75(16):165202, 2007.
- [123] Du, C.L., Z.B. Gu, M.H. Lu, J. Wang, S.T. Zhang, J. Zhao, G.X. Cheng, H. Heng, and Y.F. Chen: *Raman spectroscopy of (Mn, Co)-codoped ZnO films*. Journal of Applied Physics, 99(12):123515–123515, 2006.
- [124] Exarhos, G.J. and S.K. Sharma: *Influence of processing variables on the structure and properties of ZnO films*. Thin Solid Films, 270(1):27–32, 1995.
- [125] Šćepanović, M., M. Grujić-Brojčin, K. Vojisavljević, S. Bernik, and T. Srećković: *Raman study of structural disorder in ZnO nanopowders*. Journal of Raman Spectroscopy, 41:914–921, 2010.
- [126] Roth, A.P. and D.F. Williams: *Properties of zinc oxide films prepared by the oxidation of diethyl zinc*. Journal of Applied Physics, 52(11):6685–6692, 1981.
- [127] Major, S., A. Banerjee, K.L. Chopra, and K.C. Nagpal: *Thickness-dependent properties of indium-doped ZnO films*. Thin Solid Films, 143(1):19–30, 1986.

- [128] Sato, H., T. Minami, S. Takata, T. Miyata, and M. Ishii: *Low temperature preparation of transparent conducting ZnO:Al thin films by chemical beam deposition*. Thin Solid Films, 236(1):14–19, 1993.
- [129] Minami, T.: *New n-type transparent conducting oxides*. MRS Bulletin, 25(8):38–44, 2000.
- [130] Mahan, G.D., L.M. Levinson, and H.R. Philipp: *Theory of conduction in ZnO varistors*. Journal of Applied Physics, 50(4):2799–2812, 1979.
- [131] Gupta, T.K. and W.G. Carlson: *A grain-boundary defect model for instability/stability of a ZnO varistor*. Journal of Materials Science, 20(10):3487–3500, 1985.
- [132] Stucki, F. and F. Greuter: *Key role of oxygen at zinc oxide varistor grain boundaries*. Applied Physics Letters, 57(5):446–448, 1990.
- [133] Tuller, H.L.: *ZnO grain boundaries: electrical activity and diffusion*. Journal of Electroceramics, 4:33–40, 1999.
- [134] Mitra, P., A.P. Chatterjee, and H.S. Maiti: *ZnO thin film sensor*. Materials Letters, 35(1):33–38, 1998.
- [135] Tohsophon, T., J. Hüpkes, S. Calnan, W. Reetz, B. Rech, W. Beyer, and N. Sirikulrat: *Damp heat stability and annealing behavior of aluminum doped zinc oxide films prepared by magnetron sputtering*. Thin Solid Films, 511:673–677, 2006.
- [136] Sang, B., K. Dairiki, A. Yamada, and M. Konagai: *High-efficiency amorphous silicon solar cells with ZnO as front contact*. Japanese Journal of Applied Physics, 38:4983–4988, 1999.
- [137] Carlson, D.E.: *Ion depletion of glass at a blocking anode: I, theory and experimental results for alkali silicate glasses*. Journal of the American Ceramic Society, 57(7):291–294, 1974.
- [138] Carlson, D.E., K.W. Hang, and G.F. Stockdale: *Ion depletion of glass at a blocking anode: II, properties of ion-depleted glasses*. Journal of the American Ceramic Society, 57(7):295–300, 1974.
- [139] Carlson, D.E., K.W. Hang, and G.F. Stockdale: *Electrode "polarization" in alkali-containing glasses*. Journal of the American Ceramic Society, 55(7):337–341, 1972.
- [140] Qingfeng, X., G. Sasaki, and H. Fukunaga: *Interfacial microstructure of anodic-bonded al/glass*. Journal of Materials Science: Materials in Electronics, 13(2):83–88, 2002.
- [141] Albaugh, K.B. and D.H. Rasmussen: *Rate processes during anodic bonding*. Journal of the American Ceramic Society, 75:2644–2648, 1992.
- [142] Wallis, G.: *Direct-current polarization during field-assisted glass-metal sealing*. Journal of the American Ceramic Society, 53(10):563–567, 1970.
- [143] Borom, M.P.: *Electron-microprobe study of field-assisted bonding of glasses to metals*. Journal of the American Ceramic Society, 56:254–257, 1973.
- [144] Dussauze, M., V. Rodriguez, A. Lipovskii, M. Petrov, C. Smith, K. Richardson, T. Cardinal, E. Fargin, and E.I. Kamitsos: *How does thermal poling affect the structure of soda-lime glass?* The Journal of Physical Chemistry C, 114(29):12754–12759, 2010.

- [145] Knowles, K.M. and A.T.J. Van Helvoort: *Anodic bonding*. International Materials Reviews, 51(5):273–311, 2006.
- [146] Conradt, R.: *Chemical durability of oxide glasses in aqueous solutions: A review*. Journal of the American Ceramic Society, 91(3):728–735, 2008.
- [147] Hench, L.L. and D.E. Clark: *Physical chemistry of glass surfaces*. Journal of Non-Crystalline Solids, 28(1):83–105, 1978.
- [148] Tomozawa, M.: *Water in glass*. Journal of Non-Crystalline Solids, 73(1):197–204, 1985.
- [149] Carlson, D.E.: *Anodic proton injection in glasses*. Journal of the American Ceramic Society, 57(11):461–466, 1974.
- [150] Bosch Solar Energy AG: *Bosch solar rack slide*, 2012. http://www.bosch-solarenergy.de/en/bosch_se_online/produkte/montage/aufstaenderung_2.html, visited on 2013-08-29.
- [151] MacDonald, S.A., C.R. Schardt, D.J. Masiello, and J.H. Simmons: *Dispersion analysis of FTIR reflection measurements in silicate glasses*. Journal of Non-Crystalline Solids, 275(1):72–82, 2000.
- [152] Efimov, A.M. and V.G. Pogareva: *Ir absorption spectra of vitreous silica and silicate glasses: The nature of bands in the 1300 to 5000 cm^{-1} region*. Chemical geology, 229(1):198–217, 2006.
- [153] Lee, Y.K., Y.L. Peng, and M. Tomozawa: *IR reflection spectroscopy of a soda-lime glass surface during ion-exchange*. Journal of Non-Crystalline Solids, 222:125–130, 1997.
- [154] Rinoud, H. and G.J. Su: *Infrared absorption spectra of sodium silicate glasses from 4 to 30 μm* . Journal of the American Ceramic Society, 47(12):597–601, 1964.
- [155] Brawer, S.A. and W.B. White: *Raman spectroscopic investigation of the structure of silicate glasses (II). soda-alkaline earth-alumina ternary and quaternary glasses*. Journal of Non-Crystalline Solids, 23(2):261–278, 1977.
- [156] Brawer, S.A. and W.B. White: *Raman spectroscopic investigation of the structure of silicate glasses. I. the binary alkali silicates*. The Journal of Chemical Physics, 63:2421, 1975.
- [157] Brawer, S.A.: *Theory of the vibrational spectra of some network and molecular glasses*. Physical Review B, 11:3173, 1975.

Appendix A

IR spectral reflectivity response of low-iron soda-lime glass

In Chapter 6, the optical properties of ZnO:B-covered low-iron soda-lime glass samples were investigated. These were derived from reflectance measurements in the spectral range between 1.3 and 25 μm . Note that the introduced optical layer model implied knowledge about the optical properties of the glass, since the reflectance spectra discussed in Chapter 6 contain information about the glass, as well. Here the optical properties of the glass in the spectral range between 1.3 and 25 μm will be discussed. Furthermore, a suitable set of optical constants, required for the simulation of the reflectance measurement presented in Chapter 6, is introduced.

In Figure A.1 the reflectance of a 3.2-mm-thick low-iron soda-lime glass sample is shown in the spectral range of interest. Furthermore, the simulated reflectance spectrum is displayed. The simulated data were derived from spectral dispersion analysis, equal to the method introduced in Ref. [151]. Here, we have to model an appropriate dielectric function (ϵ), considering single phonon contributions of the glass network caused by the atomic arrangement. In crystalline materials these contributions can be taken into account by summing up the dielectric contributions of harmonic oscillators [151]:

$$\epsilon(\omega) = \epsilon_{\infty} + \sum_{j=1}^n \frac{A_j}{(\omega_j^2 - \omega^2) - i\Gamma_j\omega}, \quad (\text{A.1})$$

where A_j is to the amplitude, ω_j is the center position of the contributing oscillator, Γ_j is the broadening parameter and ϵ_{∞} is the high-frequency dielectric constant. Note that A_j is proportional to the density of oscillators probed within the material investigated. Equation A.1 represents a complex dielectric function from which the complex refractive ($\underline{n} = \sqrt{\epsilon} = n + ik$, with $n = \text{Re}\{\underline{n}\}$ the refractive index and $k = \text{Im}\{\underline{n}\}$ the extinction coefficient) can be calculated. In a further step, by employing Fresnel's equation, the reflectance can be calculated. The dispersion analysis has been com-

pleted once the difference between the measured and simulated reflectance has been minimized.

$Im\{\epsilon\}$, as a function representing the imaginary part of ϵ , has a Lorentzian line shape. This line shape, which is defined by its broadening parameter Γ_j , is suitable to describe a homogeneous excitation around the resonance frequency ω_j . Unfortunately, in amorphous materials this broadening parameter is strongly increased due to an inhomogeneous excitation caused by the deviations of atomic bond lengths and angles. Using oscillators with a Lorentzian line shape to describe the dielectric function of an amorphous material leads to poor-quality results.

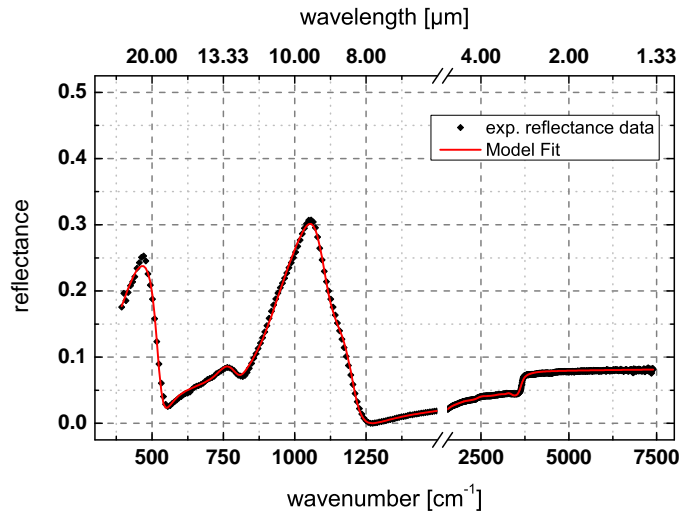


Figure A.1: Experimental and simulated IR reflectance data of a 3.2-mm-thick low-iron soda-lime glass sample.

To circumvent this limitation, $Im\{\epsilon\}$ is described by Gaussian peak functions. Here, the broadening parameter does not significantly affect the dispersion far from the resonance frequency ω_j , and thus leads to much better results. In the present work $Im\{\epsilon\}$ was modeled by a sum of Gaussian peak functions:

$$Im\{\epsilon(\omega)\} = \sum_{j=1}^n A_j \exp - \left(\frac{\omega - \omega_j}{\Gamma_j} \right)^2, \quad (\text{A.2})$$

where 10 individual Gaussian peak functions were parameterized according to the values presented in Table A.1. Note that the parameterization was intended to fit simulated and measured IR reflectance data rather than to identify single phonon contributions. For deeper analysis of possible peak positions and broadening parameters the reader is referred to the literature [151–157].

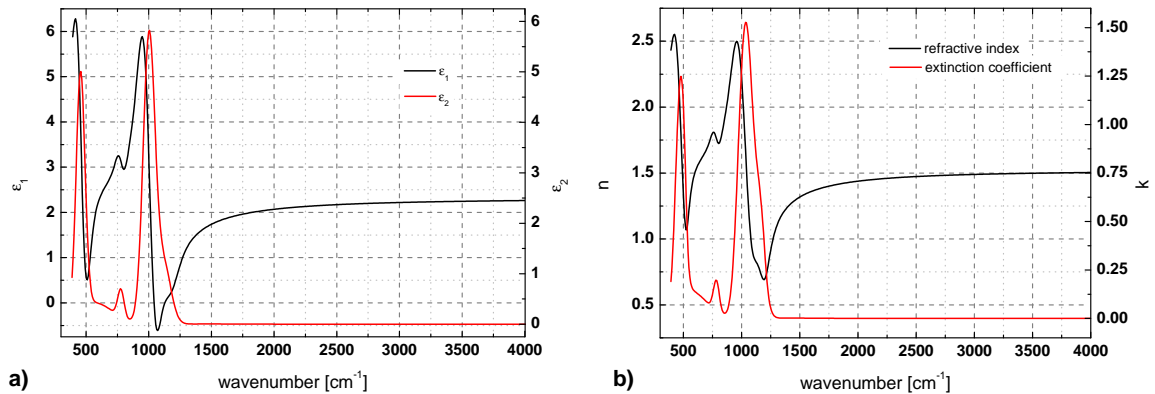
Whereas from Equation A.1 the real and imaginary parts of the dielectric function are known, in Equation A.2 only the imaginary part is given. The real part of the dielectric function ($Re\{\epsilon\}$) can be calculated according to the relation of Kramers-Kronig [151]:

Table A.1: Parameterization of Gaussian peak functions used to model $Im\{\epsilon\}$ of a low-iron soda-lime glass sample.

	A_j	$\omega_j [cm^{-1}]$	$\Gamma_j [cm^{-1}]$
ω_{01}	0.000227	3471.65	230.02
ω_{02}	0.000078	3200.00	246.20
ω_{03}	0.000400	2400.00	1313.07
ω_{04}	0.000356	2200.00	215.01
ω_{05}	0.006635	1487.51	577.26
ω_{06}	1.163153	1123.64	133.06
ω_{07}	5.685519	1006.18	110.10
ω_{08}	0.552204	781.65	58.96
ω_{09}	0.256300	570.00	344.91
ω_{10}	4.688592	461.17	82.54

$$Re\{\epsilon(\omega)\} = \epsilon_\infty + \frac{2}{\pi} \int_0^\infty \frac{\omega' Im\{\epsilon(\omega')\}}{\omega'^2 - \omega^2} d\omega' \quad (A.3)$$

The real and imaginary part of the dielectric function ($\epsilon = \epsilon_1 + i\epsilon_2$) which were parameterized in accordance with the parameters shown in Table A.1 are presented in Figure A.2a. The refractive index (n) and extinction coefficient (k), calculated by the relation $\underline{n} = \sqrt{\epsilon}$, are presented in Figure A.2b. Note, that the refractive index approaches a value of 1.5 above $2500 cm^{-1}$ and stays constant, also for wavenumbers above $4000 cm^{-1}$. This is in agreement with well-known values for glass in the transparent spectral region ($\lambda < 2500 nm$, $\omega \geq 5000 cm^{-1}$).

**Figure A.2:** (a) Real and imaginary part of the dielectric function. (b) The refractive index and extinction coefficient calculated by the relation $\underline{n} = \sqrt{\epsilon}$.

Publications

- D. Messerschmidt, S. Nicolay, L. Ding, G. Bugnon, F. Meillaud, J. Eberhardt and C. Ballif
„Ethanol-enriched low-pressure chemical vapor deposition ZnO bilayers: Properties and growth - A potential electrode for thin film solar cells“
Journal of Applied Physics **2**(113), 024908–024908 (2013).
- D. Messerschmidt, A. Hochmuth, E. Rädlein, H. Romanus, W.-H. Gnehr, J. Eberhardt and C. Ballif
„Anodic degradation of ZnO on soda-lime glass“
Solar Energy Materials and Solar Cells (117), 569–576 (2013).
- D. Messerschmidt, K. Bratz, W.-M. Gnehr, H. Romanus, J. Eberhardt, S. Nicolay and C. Ballif
„Optical properties of anodically degraded ZnO“
Journal of Applied Physics **9**(115), 094902 (2014).
- L. Ding, L. Fanni, D. Messerschmidt, S. Zabihzadeh and M. Masis Morales, S. Nicolay and C. Ballif
„Tailoring the surface morphology of zinc oxide films for high-performance micromorph solar cells“
Solar Energy Materials and Solar Cells (128), 378–385 (2014).

Thank you...

Ich möchte mich an dieser Stelle bei einigen Menschen bedanken. Dankend anerkennen möchte ich die Unterstützung und die Rahmenbedingungen – wenn auch nicht die einfachsten – die es mir ermöglichten die vorliegende Arbeit anzufertigen.

Zunächst möchte ich mich bei den Mitgliedern der Prüfungskommission Herrn Prof. Philipp Aebi, Prof. Christophe Ballif, Prof. Thomas Südmeyer, Prof. Edda Rädlein und Herrn Dr. Jens Eberhardt für das Erstellen der Gutachten und Würdigen meiner Arbeit bedanken.

Ganz besonders und ausdrücklich möchte ich meinen Dank an Herrn Dr. Jens Eberhardt richten. Vielen Dank für die umfassende Betreuung meiner Arbeit. Herr Eberhardt stand mir stets mit fachlichem sowie persönlichem Rat zur Seite. Er hat damit zum wesentlichen Gelingen der Arbeit beigetragen. Jens, hab vielen Dank für alles!

Außerdem gilt mein Dank Herrn Dr. Christian Koitzsch, dem damaligen technischen Geschäftsführer und Herrn Dr. André Hedler, dem damaligen Leiter der Entwicklung der Bosch Solar Thin Film GmbH. Danke, dass ich die vorliegende Arbeit in einem hoch motivierten und herausfordernden Umfeld anfertigen durfte. Ich möchte mich für die Bereitstellung des Themas, technischer Ressourcen und für die persönliche Unterstützung bedanken.

Auch möchte ich mich an dieser Stelle bei allen anderen Mitgliedern der Entwicklung und den Mitarbeitern der ehemaligen Bosch Solar Thin Film GmbH für ihre Unterstützung bedanken. Gerne erinnere ich mich an eine turbulente, aber auch spannende Zeit zurück.

Mein Dank gilt ebenfalls Herrn Prof. Christophe Ballif und seinem hoch motivierten Team von Wissenschaftlern. Herr Ballif ermöglichte es mir einen Teil meiner Ergebnisse bei einem mehrmonatigen Aufenthalt am "Institute of Microengineering (IMT)" in Neuchâtel zu erarbeiten. Christophe, vielen Dank für die Bereitstellung technischer Ressourcen und für deine persönliche Unterstützung.

In diesem Zusammenhang möchte ich mich auch bei Herrn Dr. Sylvain Nicolay, dem wissenschaftlichen Fachgruppenleiter für transparente leitfähige Oxide am IMT, bedanken. Danke für die freundliche Aufnahme und die Betreuung meiner Person in deiner Fachgruppe. Die fachlichen Diskussionen und Anregungen haben zum Gelingen dieser Arbeit beigetragen.

Bedanken möchte ich mich bei Prof. Edda Rädlein, Leiterin des Fachgebietes für anorganisch-nichtmetallische Werkstoffe an der Fakultät für Maschinenbau der technischen Universität Ilmenau. Durch den von ihr vermittelten Einblick in die Chemie von Gläsern und durch zahlreiche Diskussion half sie mir, notwendiges Verständnis für einen Teil meiner Arbeit zusammenzutragen .

Auch Herrn Dr. Henry Romanus, wissenschaftlicher Mitarbeiter am Zentrum für Mikro- und Nanotechnologien der technischen Universität Ilmenau, gilt mein Dank. Bei zahlreichen experimentellen Fragestellungen unterstützte er mich nach Möglichkeit und mit dem ihm zur Verfügung stehenden Analysesquipment. Vielen Dank für zahlreiche Diskussionen und deine Unterstützung.

Ausdrücklich möchte ich mich bei allen nicht namentlich genannten Unterstützern bedanken. Danke, für die großen und vielen kleine Bausteine, aus denen ich diese Arbeit zusammensetzen durfte.

Schliesslich gilt mein Dank auch meiner Familie, meinen Freunden und meiner Freundin, Janine. In all der Zeit wurde ich durch sie unterstützt und wenn es notwendig war auch gestützt. DANKE!

Curriculum Vitae

Personal information

Last name	Messerschmidt
First name	Daniel
Date of birth	7 th February 1983
Location of birth	Meiningen, Germany
Nationality	German
Marital Status	Single

Education

1989–1995	Elementary school: „Rosa Luxemburg“, Walldorf
1995–2002	Secondary school „Henfling Gymnasium“, Meiningen

Military duty

2002–2003	„General Olbricht Kaserne“, Leipzig
-----------	--

Studies

2003–2009	Studies of technical physics at the technical University of Ilmenau
2008–2009	Diploma thesis „Untersuchungen zur Stabilität mikromorpher Siliziumdünnschicht-Solarzellen“
since 2010	Doctorate at the University of Neuchâtel

Professional activity

2009–2013	Development Engineer Bosch Solar Thim Film GmbH, Erfurt
since 2014	Development Engineer Robert Bosch GmbH, Reutlingen

Reutlingen, den August 31, 2014

Daniel Messerschmidt